Analiza strujanja i prijelaza topline u odjeljku motora lakog zrakoplova korištenjem numeričke mehanike fluida

Zrnić, Dino

Master's thesis / Diplomski rad

2018

Degree Grantor / Ustanova koja je dodijelila akademski / stručni stupanj: **University of Zagreb, Faculty of Mechanical Engineering and Naval Architecture / Sveučilište u Zagrebu, Fakultet strojarstva i brodogradnje**

Permanent link / Trajna poveznica: https://urn.nsk.hr/urn:nbn:hr:235:767178

Rights / Prava: In copyright/Zaštićeno autorskim pravom.

Download date / Datum preuzimanja: **2024-04-23**

University of Zagreb

Faculty of Mechanical Engineering and Naval Architecture

MASTER'S THESIS

Dino Zrnić

Zagreb, 2018.

UNIVERSITY OF ZAGREB

FACULTY OF MECHANICAL ENGINEERING AND NAVAL
ARCHITECTURE

MASTER'S THESIS

THERMAL MANAGEMENT ANALYSIS IN THE ENGINE COMPARTMENT OF A LIGHT AIRCRAFT USING COMPUTATIONAL FLUID DYNAMICS

Mentor:

prof. dr. sc. Hrvoje Jasak

Student:

Dino Zrnić

ZAGREB, 2018.

Statement | Izjava

I hereby declare that I have made this thesis on my own using the knowledge acquired during my studies and the cited references.

Izjavljujem da sam ovaj rad radio samostalno koristeći znanja stečena tijekom studija i navedenu literaturu.

Zagreb, January 2018.   Dino Zrnić

DIPLOMSKI ZADATAK

Student: **Dino Zrnić**   Mat. br.: 0035191374

Naslov rada na
hrvatskom jeziku: **Analiza strujanja i prijelaza topline u odjeljku motora lakog zrakoplova korištenjem numeričke mehanike fluida**

Naslov rada na
engleskom jeziku: **Thermal Management Analysis in the Engine Compartment of a Light Aircraft using Computational Fluid Dynamics**

Opis zadatka:

Design of an engine compartment of a light aircraft involves challenges on thermal management, including limited space, minimisation of external drag, limitations on wall temperature and influence of the propeller wake on the internal flow pattern. Detailed modelling of a rotating propeller and conjugate heat transfer conditions in an engine radiator or air-cooled ribs is impractical for design/optimisation simulations. Therefore, a choice of simplified models of sufficient accuracy is crucial.

In this project, Computational Fluid Dynamics (CFD) shall be used to simulate the flow and heat transfer conditions in the engine compartment of a Pipistrel Panthera aircraft.

The candidate shall perform the following tasks:

· Peform detailed simulations of the aircraft propeller in free stream under steady conditions using the Multiple Frames of Reference (MRF) approach. Assemble the propeller performance curves by simulating at least 4 operating points. Examine the importance of compressibility effects in the flow for one operating point;

· Perform a literature survey on single-stream and multi-stream integral heat exchanger models appropriate for engine compartment thermal management simulations;

· Implement the appropriate integral heat exchanger model in OpenFOAM;

· Prepare the computational mesh of the Panthera aircraft engine compartment, including the actuator disk plane for the propeller model and the porous heat exchanger region.

· Perform a steady compressible CFD simulation of the flow and heat transfer in the engine compartment of the Panthera aircraft using the actuator disk propeller model and the integral heat exchanger model. Present the results of simulations in an appropriate form, including integral heat transfer parameters and flow field visualisation;

The Thesis shall list the bibliography and any assistance received during this study.

Zadatak zadan: Rok predaje rada: Predviđeni datumi obrane:

16. studenog 2017.   18. siječnja 2018.   24., 25. i 26. siječnja 2018.

Zadatak zadao: Predsjednik Povjerenstva:

Prof. dr. sc. Hrvoje Jasak   Prof. dr. sc. Ivica Smojver

Contents

List of Figures

List of Tables

List of Symbols

Subscripts

Abbrevatons

Sažetak

U ovom radu predstavljen je prikaz hlađenja i analiza strujanja i prijelaza topline u odjeljku motora lakog zrakoplova korištenjem numeričke mehanike fluida. Kako propeler ima veliki utjecaj na ulaznu struju zraka u odjeljak motora gdje se odvija hlađenje, napravljena je zasebna numerička simulacija rada propelera. Ovom simulacijom proučavani su stlačivi efekti strujanja s ciljem dobivanja točnih sila i momenata za veće područje rada motora. Ti podatci su potrebni kako bi se pomoću teorije diska postavili uvjeti za sljedeću numeričku simulaciju koja obuhvaća prijelaz topline s motora na okolni zrak. U ovoj numeričkoj simulaciji disk je postavljen na mjesto propelera, tj. ispred difuzora, te se računa i prikazuje karakteristika strujanja fluida koji prvo ulazi u difuzor, a potom u odjeljak motora hlađenog zrakom. Također je izračunata toplina koja se prenosi samo konvekcijom na orebrenim površinama. Nadograđena su tri nova modela izmjenjivača topline unutar algoritma za proračun stlačivog strujanja. Ti modeli su testirani i validirani na jednostavnom primjeru cijevi kvadratnog presjeka. Na kraju su prikazani rezultati numeričke simulacije povezanih dijelova propelera i odjeljka motora čiji rezultati su dobiveni zasebnim numeričkim simulacijama.

Ključne riječi: stlačivost, CFD, prijelaz topline, `foam-extend`, zrakoplovni propeler, hlađenje, model izmjenjivača, porozni medij

Summary

In this thesis the cooling system of an engine in a light aircraft influenced by a propeller is simulated. Firstly, investigation is made for aircraft propeller separately, in order to examine air compressibility effects of the flow around the propeller and to determine the performance of the propeller. The second set of simulations deals with heat transfer in the engine compartment of the Pipistrel Panthera aircraft. Computational domains for the propeller and the engine cooling system are made separately for each case.

In order to calculate heat transfer in the engine compartment three new heat exchanger models have been implemented and upgraded with porous media effects inside the compressible flow solver: Total Volumetric Heat model, Single stream model and the Nusselt model. Implemented models are validated on a simple test case and comparison of the results is presented. After successful validation heat transfer simulations are performed for engine cooling. Finally, a steady compressible CFD simulation of the flow with heat transfer is performed for the engine compartment case using the actuator disk model and the integral heat exchanger model. Actuator disk theory which uses calculated force and moment data from the aircraft propeller case has been implemented in order to study influence of propeller wakes and fluid flow on the cooling system of engine compartment.

Keywords: compressible, CFD, `foam-extend`, aircraft propeller, heat transfer, cooling, exchanger model, porous media

Prošireni sažetak

Za pokretanje vozila podzvučnim brzinama koriste se propeleri, koji ovisno o primjeni, mogu biti racličitih tipova. Konstruiranje i optimizacija propelera za određeno područje rada predstavlja zahtjevan zadatak koji iziskuje sintezu znanja iz područja mehanike fluida i područja konstrukcije. Kako je propeler obično postavljen ispred motora, odnosno ispred usisnika za hlađenje motora, veliki je utjecaj vrtložnog stujanja na kvalitetu nadolazeće struje zraka u odjeljak motora u kojem se događa prijelaz topline s motora na okolni zrak. U ovom radu proučavati će se samo aerodinamičke sile i momenti i oni će biti potrebni kao ulazni parametri za numeričku simulaciju hlađenja motora. Pomoću teorije diska, koja podrazumijeva aproksimaciju propelera diskom jednakog radijusa. Na taj način je prikazano hlađenje koje ovisi o strujanju unutar kućišta motora. Budući da se strujanje mijenja zbog rotacijske komponente koja je uzrokovana vrtnjom elise potrebno je prilagoditi geometriju difuzora. Kako bi hlađenje bilo optimalno treba se fokusirati na površinu hlađenja (koja mora biti što veća), te na količinu predane energije (koja ovisi o karakteristikama stujanja u području izmjene topline).

0.1. Matematički model

Zakon očuvanja mase, Navier-Stokesove jednadžbe količine gibanja i zakon očuvanja energije čine tri zakona koji se koje se koriste u numeričkim simulacijama mehanike fluida i drugih područja fizike [1]. Kako Navier-Stokesove jednadžbe samo opisuju ravnotežu momenata u sustavu, da bi smo u potpunosti opisali polje strujanja moramo koristiti dodatne pretpostavke. Te pretpostavke uključuju rubne uvjete, zakon očuvanja mase i energije, jednadžbu stanja, itd.

Zakon očuvanja mase glasi:

$$\frac{\partial \rho}{\partial t} + \nabla \bullet (\rho \mathbf{u}) = 0 \,,$$

gdje je ρ gustoća, $\mathbf{u}$ brzina i t vrijeme, a govori da ako ne postoje izvori i ponori unutar kontrolnog volumena masa će biti očuvana. Zakon očuvanja količine gibanja govori da će suma svih sila i momenata biti jednaka nuli ukoliko ne postoje vanjske sile i momenti koji djeluju na kontrolni volumen.

Zakon u konzervativnoj formi definiran je kao:

$$\frac{\partial}{\partial t}(\rho \mathbf{u}) + \nabla \bullet (\rho \mathbf{u} \otimes \mathbf{u}) = \nabla(\mu \nabla \mathbf{u}) - \nabla p + \mathbf{Q^V} \,,$$

gdje je e specifična energija, $\dot{q}_V$ izvor ili ponor promjene prijelaza topline unutar materijalnog volumena po jedinici volumena i $\dot{q}_S$ je promjena topline kroz površinu materijalnog volumena. Zakon očuvanja energije odgovara prvom zakonu termodinamike, koji govori da se energija ne može stvoriti niti uništiti; ona se može samo pretvarati iz jednog oblika u drugi. U konzervativnoj formi je predstavljen kao:

$$\frac{\partial \rho e}{\partial t} + \nabla \bullet (\rho \mathbf{u} e) = -\nabla \bullet (p \mathbf{u}) + \nabla \bullet (\tau \bullet \mathbf{u}) - \nabla \bullet \dot{q}_s + \mathbf{f_b} + \dot{q}_V \,.$$

Analiziranjem svih zakona možemo dobiti generalnu transportnu jednadžbu u konzervativnoj formi koja je zapisana za opću varijablu ϕ:

$$\frac{\delta \phi}{\delta t} + \nabla \cdot (\mathbf{u} \phi) - \nabla \cdot (\gamma \nabla \phi) = q_v \,.$$

Transportna jednadžba se sastoji od lokalne promjene, konvekcijskog, difuzijskog i izvorskog člana.

Modeliranje turbulencije

Strujanje fluida može biti laminarno, turbulentno ili u prijelaznom području. Energija turbulencije definirana je energijom pri čemu se energija kaskadno prenosi s većih vrtloga na manje [2], [3]. Uvođenjem Reynoldsovog osrednjavanja Navier-Stokesove osrednjene jednadžbe možemo zapisati:

$$\frac{\partial}{\partial t}(\rho\overline{\mathbf{u}}) + \nabla \cdot (\rho\overline{\mathbf{u}} \otimes \overline{\mathbf{u}}) = -\nabla\overline{p} + (\nabla \cdot (\overline{\tau} - \rho\overline{\mathbf{u}'\mathbf{u}'}) + \overline{\mathbf{f}}_b \,,$$

u kojima uvodimo novi član $\tau^{\mathbf{R}}$ poznat kao Reynoldsov tenzor naprezanja, koji sadrži šest novih nepoznanica. Te se modelira Boussinesqovom hipotezom [1]. Postoji više načina modeliranja turbulencije, a to su:

- Algebarski modeli

- Modeli s jednom jednadžbom

- Modeli s dvije jednadžbe

- Modeli jednadžbi višeg reda.

U ovom radu korišten model je turbulencije s dvije jednadžbe poznat kao k-ω SST model [4]. Prva jednadžba za turbulentnu kinetičku energiju k:

$$\frac{\partial}{\partial t}(\rho k) + \nabla \cdot (\rho\overline{\mathbf{u}}k) = \nabla \cdot (\mu_{effk}\nabla k) + Q^k \,.$$

Druga jednadžba je za skalu turbulencije ω:

$$\frac{\partial}{\partial t}(\rho\omega) + \nabla \cdot (\rho\overline{\mathbf{u}}\omega) = \nabla \cdot (\mu_{effk}\nabla\omega) + Q^\omega \,,$$

gdje su ρ gustoća, $\overline{\mathbf{u}}$ osrednjena vrijednost brzine, μ_{eff} efektivna turbulentna viskoznost, te Q^ω i Q^k predstavljaju članove stvaranja turbulentne energije. Cijelokupan opis ovog modela može se vidjeti u poglavlju 2.2..

0.2.   Numeričko modeliranje mehanike fluida

Metoda kontolnih volumena je numerička metoda koja počiva na linearizaciji i diskretizaciji parcijalnih diferencijalnih jednadžbi [1]. Nakon diskretizacije i pribrajanja odgovarajućih članova, dobiva se linearni sustav diskretiziranih jednadžbi koji se mogu zapisati u formi:

$$\mathbf{Ax} = \mathbf{b} \,.$$

Međudjelovanje rotora i statora

Modeliranje međudjelovanja rotora i statora ustaljena je tematika u konstruiranju turbostrojeva. Kako u slučaju numeričke simulacije propelera postoji granica između rotirajuće i stacionarne mreže, mora se omogućiti komunikacija između ta dva područja. Numerički princip s matematičkom podlogom opisan je u [5]. Na slici (3.2) vidljiv je
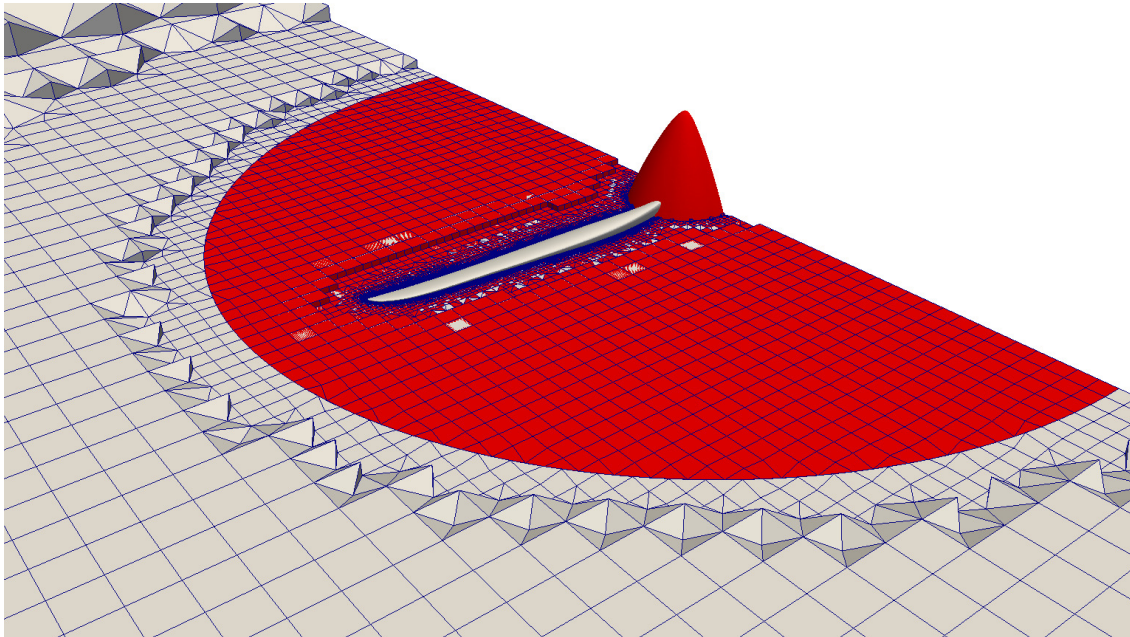
Slika 0.1: Prikaz mreže sa MRF zonom.

cilindričan rub između zona, te je poželjno da je rezolucija mreže što sličnija na obje strane.

Modeliranje porozne zone

Orebrene površine kod hladnjaka su komplicirana geometrija koju je gotovo nemoguće prekriti kvalitetnom proračunskom mrežom. Kako bi se propračun pojednostavnili uvodi se porozna zona oblika hladnjaka cilindara. Kako bi je modelirali i definirali potrebno je odrediti pad tlaka kroz tu zonu kao funkciju brzine. S obzirom na tu funciju mogu se izračunati Darcy-Forheimmerovi koeficijenti s kojima se računa jakost ponora brzine unutar momentne jednadžbe:

$$S_i = -\left(\mu\mathbf{D} + \frac{1}{2}\rho|\mathbf{u}|\mathbf{F}\right)\mathbf{u} \ .$$

Tri modela izvora topline su implementirana i uspoređena u ovom diplomskom radu.

1. `Toplina totalnog volumena`

   Model je najjednostavniji i modelira izvor topline prema:

   $$\dot{Q}_i = \dot{Q}_{tot}\frac{V_i}{\displaystyle\sum_{i=0}^{n} V_i} \ ,$$

2. `Jednostrujni model`

   Uzima u obzir maseni protok jedne struje, te osigurava veći prijenos topline s obzirom na mjesta gdje je protok veći te suprotno. Izvor topline definiran je za svaku ćeliju jednadžbom [6]:

   $$\dot{Q}_i = \dot{Q}_{tot}\frac{V_i u_i(T_{ref} - T_i)}{\displaystyle\sum_{i=0}^{n} V_i u_i(T_{ref} - T_i)} \ .$$

3. `Nusseltov model`

   Uzima u obzir Nusseltov broj, koji kao dodatak na klasičnu jednadžbu prijenosa topline konvekcijom, ima dodatnu varijablu ε koja određuje efektivnost izmjenjivača topline. Efektivnost se računa preko empirijske jednadžbe [7]:

   $$\epsilon = 1 - \exp\left[-\frac{1}{C_r}N_{\mathrm{tu}}^{0.22}(1 - e^{-C_r N_{\mathrm{tu}}^{0.78}})\right] \ ,$$

   dok je izvor topline definiran kao:

   $$\dot{Q}_{\mathrm{tot}} = \epsilon C_{\mathrm{min}}(T_{\mathrm{in}} - T_i)$$
   $$\dot{Q}_{\mathrm{cell}} = \dot{Q}_{\mathrm{tot}}\frac{V_{\mathrm{i}}}{\displaystyle\sum_{i=0}^{n} V_{\mathrm{i}}} \ .$$

0.3.   Proračunska mreža i rezultati

Proračunska mreža geometrije avionskog propellera i sustava hlađenja izrađena je pomoću *snappyHexMesh* aplikacije unutar programa `foam-extend`. Domena za avionski propeler je takvih dimenzija da se postignu preporučena idealna konvergencija [8]. Geometrija propelera prikazana je na slici (0.2), a prikaz polovice domene sa prikazom spoja rotacijske (MRF zone) i stacionarne mreže [9] dan je na slici (0.3). Prilikom izrade mreže, naglasak je bio na profinjenju mreže u području ruba lopatice, te na području interferencije stacionarne i rotacijske mreže, kako bi numerička simulacija bila stabilna.
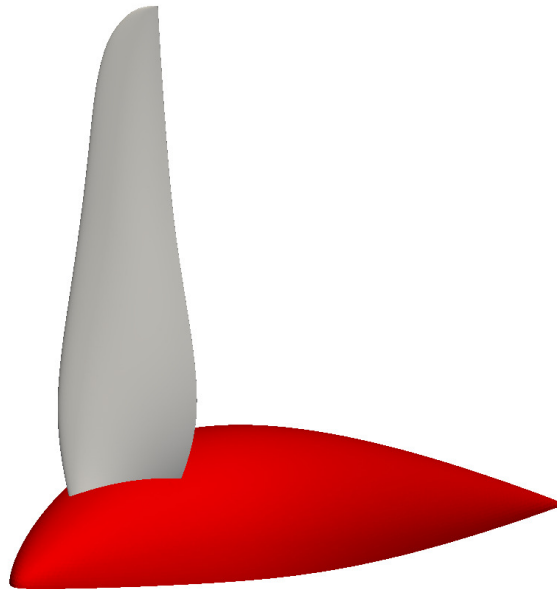
Slika 0.2: Geometrija propelera.
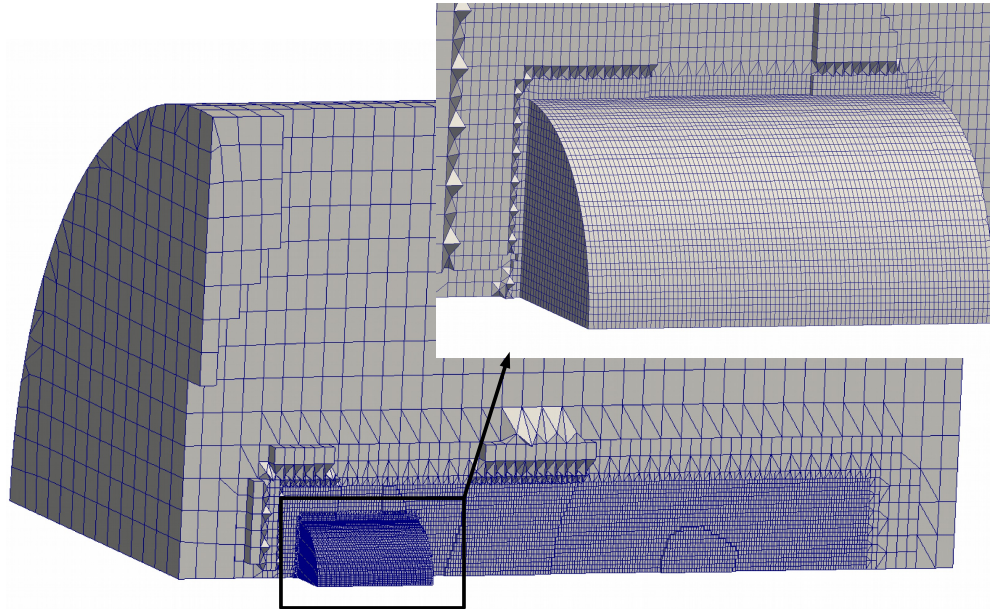
Slika 0.3: Prikaz domene sa spojem rotacijske i stacionarne mreže.

Druga numerička mreža je vezana za hlađenje, odnosno prijenos topline u odjeljku motora lakog zrakoplova. Na slici (0.4) vidimo unutrašnje dijelove sustava hlađenja. Plavo obojana geometrija prikazuje difuzor u koji ulazi struja zraka potrebna za hlađenje, a crveno obojena geometrija prikazuje unutrašnji prostor odjeljka motora te smeđe obojana geometrija prikazuje poroznu zonu. Porozna zona ima oblik geometrije motora te su unutar nje definirani modeli prijenosa topline.
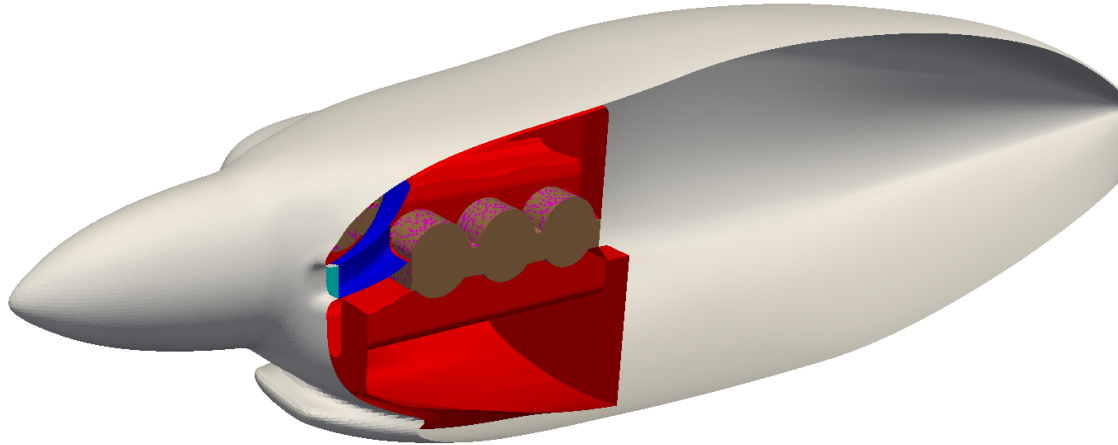
Slika 0.4: Unutrašnji dijelovi sustava hlađenja motora.

Rezultati simulacije vrtnje avionskog propelera

Prikazani su rezultati numeričke simulacije vrtnje avionskog propelera pri kutnoj brzini od 216.66 rad/s, te pri brzini neporemećene struje 42.3 m/s. Termodinamičke karakteristike zraka izračunate su za nadmorsku visinu ≈ 2000 m. Vidi se da na podtlačnoj strani lopatice tlak pada kako se približavamo vrhu lopatice, gdje je točka minimalnog tlaka. Nasuprot, s pretlačne strane tlak je ravnomjerno raspoređen duž radijusa, dok na stražnjem bridu pri vrhu lopatice tlak značajno raste. Kako je razlika tlakova s prednje i stražnje strane najveća pri vrhu propelera, tamo se javlja i najveća pogonska sila.
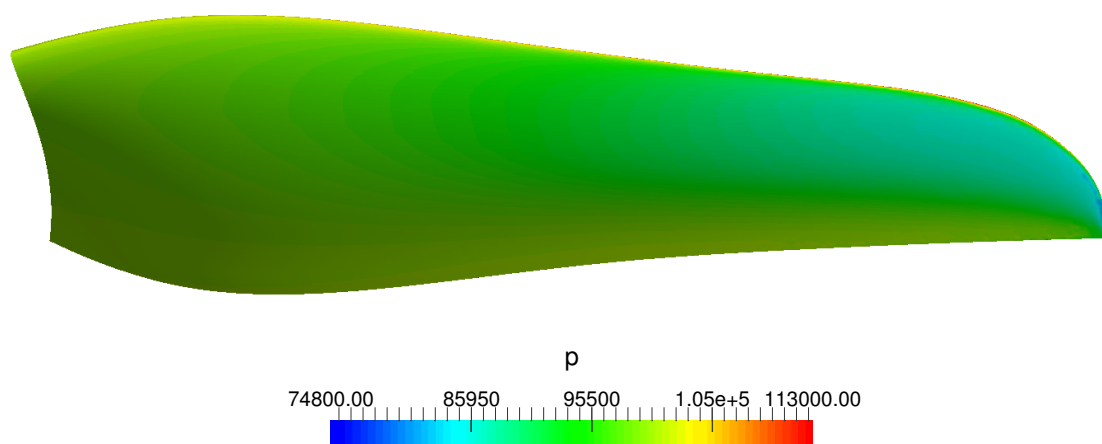
Slika 0.5: Podtlačna strana.
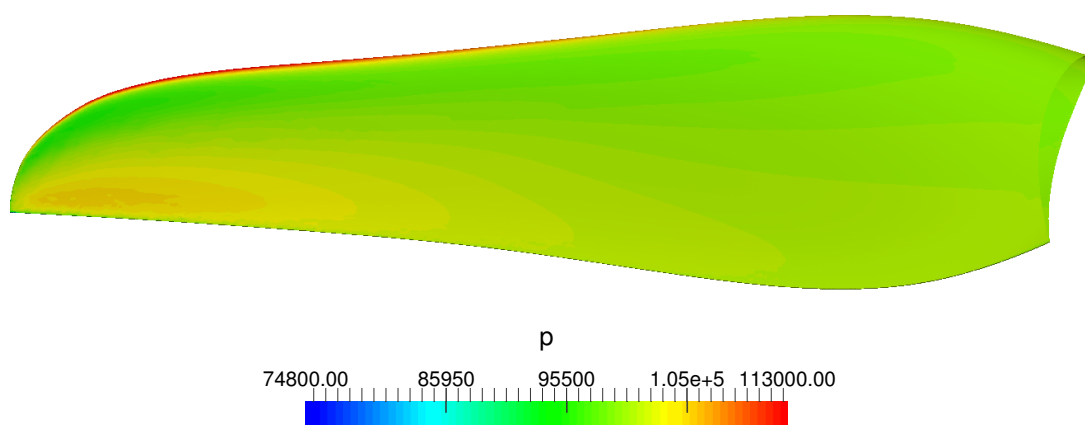
Slika 0.6: Pretlačna strana.

Budući da postoji razlika tlakova zbog promjene smjera gibanja fluida uzrokovane geometrijom i oblikom propelera, posljedica je vrtlog koji se javlja na vrhu. Taj vrtlog postoji i na spoju propelera i kape elise ali je manjeg intenziteta zbog manje razlike tlakova i manjeg intenziteta brzine pri početku lopatice. Opisani vrtlozi mogu se vidjeti na slici (5.7).
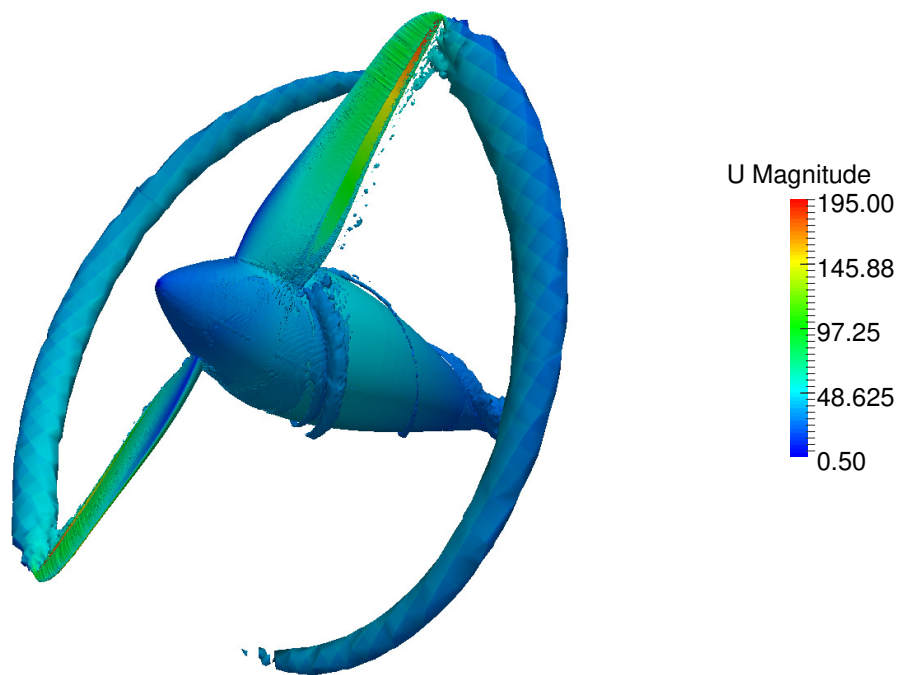
Slika 0.7: Vrtlog na početku i kraju lopatice.

Kako bi se pokazao utjecaj stlačivosti zraka, rezultati simulacije stlačivog strujanja uspoređeni su s rezultatima nestlačivog strujanja, prikazano u tablici (0.1). Razlika rezultata pogonske sile nestlačivog stacionarnog i tranzijentnog rješavača je 1.25% a momenta 1.39%. Što dovodi do zaključka da su u ovom slučaju uvjeti strujanja stacionarni. Rezultati stlačivog stacionarnog rješavača se u sili razlikuju 6.59% i u momentu 27%. Takve razlike govore da je utjecaj stlačivosti zraka na raspodjelu tlaka velik, pa tako i na sile i momente. Budući da je najveći doprinos sili na području vrha lopatice, gdje su i najveće brzine, razlike između stlačivog i nestlačivog strujanja su očekivane.

Tablica 0.1: Usporedba stlačivih i nestlačivih sila i momenata.

Rješivači	Pogonska sila [N]	Moment [Nm]
Stlačivi stacionarni MRF	470.55	117.13
Nestlačivi stacionarni MRF	497.49	84.29
Nestacionarni nestlačivi	503.8[1]	85.48[2]

Na slici (0.8) prikazana je efikasnost propelera u osam radnih točaka. Pri tome je zadržana brzina rotacije od $241\,\mathrm{rad/s}$, a mijenjana je ulazna brzina neporemećene struje. Vidimo da je u točki koraka napredovanja od 1.158 postignuta maksimalna vrijednost efikasnosti $\eta = 0.69$.
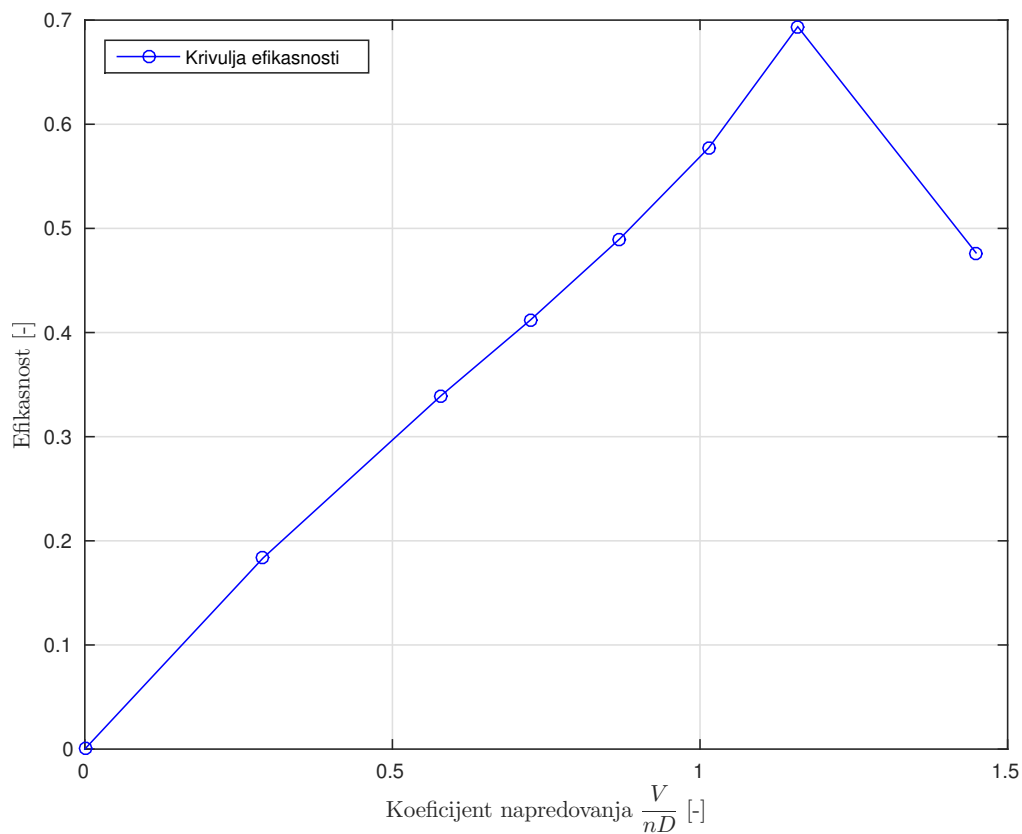
Slika 0.8: Raspodjela efikasnosti propelera u ovisnosti o koeficijentu napredovanja.

---

[1]tokom rotacije, pogonska sila je između 503.05 – 504.85 [N]
[2]tokom rotacije, moment je između 85.08 – 85.88 [Nm]

Usporedba rezultata hlađenja motora

Rezultati su uspoređeni za tri validirana modela prijelaza topline koji su definirani u poglavlju (3.6.). Slučajevi su postavljeni za nadolazeću neporemećenu struju zraka od 100 m/s što je brzina krstarenja zrakoplova. Kako se modeliraju orebrene površine pomoću modela porozne zone potrebo je izračunati Darcy-Forheimmerove koeficijente. Pomoću eksperimentalnih podataka pada tlaka, koeficijenti su:

$$
\begin{aligned}
D &= \frac{\alpha}{\nu} = 13.59530 \cdot 10^6 \\
E &= \frac{2\beta}{\rho} = 727.27 \ .
\end{aligned}
\tag{0.1}
$$

Kako se prikazala temperaturna raspodjela, potrebno je definirati snagu izvora topline, odnosno koliko topline se prenosi u svakom vremenskom koraku sa motora na okolni zrak. Toplina je u svakom vremenskom koraku definirana kao:

$$
Q_{tot} = \alpha S_{ref}(T_s - T_f) = 21650.5 \, W \ ,
\tag{0.2}
$$

gdje je α izračunat prvo lokalno za jednu orebrenu površinu, a potom za cijeli motor. Postupak je prikazan u članku [10].

Rezultati na slikama (0.9) i (0.10) prikazuju temperaturnu raspodjelu unutar odjeljka motora. Model topline totalnog volumena prikazuje vidno drukčiju temperaturnu sliku od modela jedne struje. Kako prvi model definira snaga izvora topline samo preko volumena ćelije, vidljivo je nakupljanje topline nakon oštrih rubova, dok model jedne struje uzima u obzir brzinu i temperaturu susjednih ćelija, čime se uvodi dodatno gibanje i posljedično ima efekt dodatnog hlađenja. Na slici (0.11) prikazani su rezultati temperaturne raspodjele Nusseltovog modela, dok su na slici (0.12) na prikaz dodane strujnice koje prikazuju porast temperature prolaskom kroz poroznu zonu. Također vidljivo je vrtloženje unutar odjeljka motora koje smanjuje efikasnost hlađenja i povećava ukupnu temperaturnu raspodjelu u području motora.
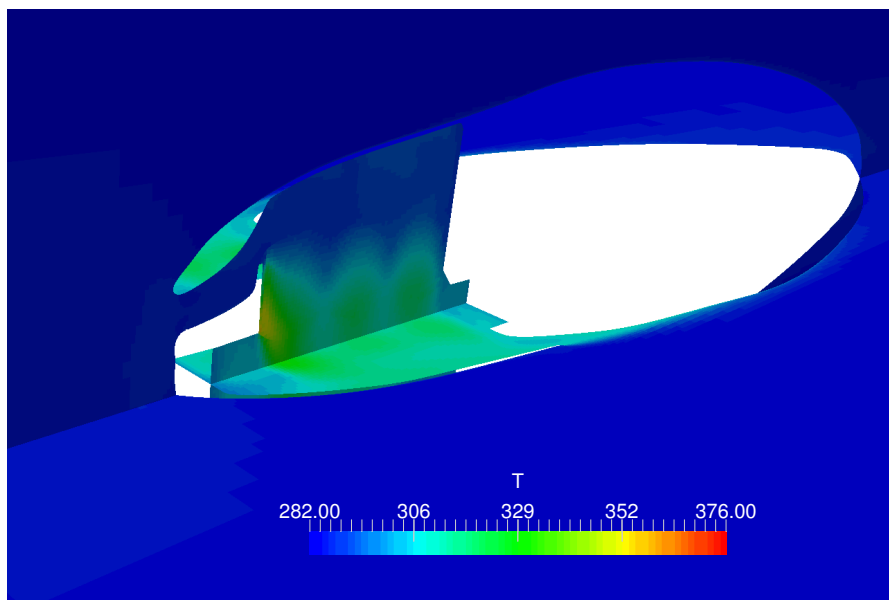
Slika 0.9: Temperaturna raspodjela rezultata modela Topline totalnog volu-
mena.
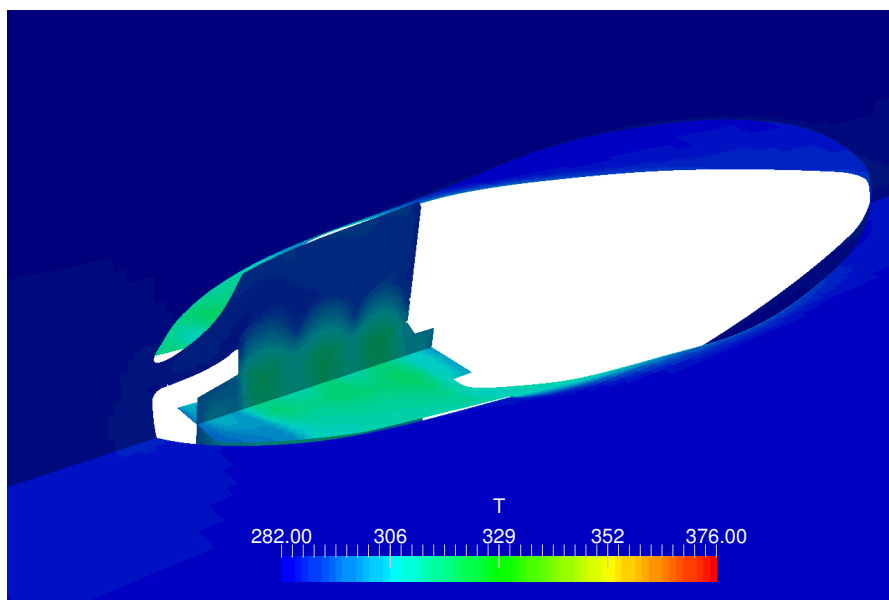
Slika 0.10: Temperaturna raspodjela modela Jedne struje.
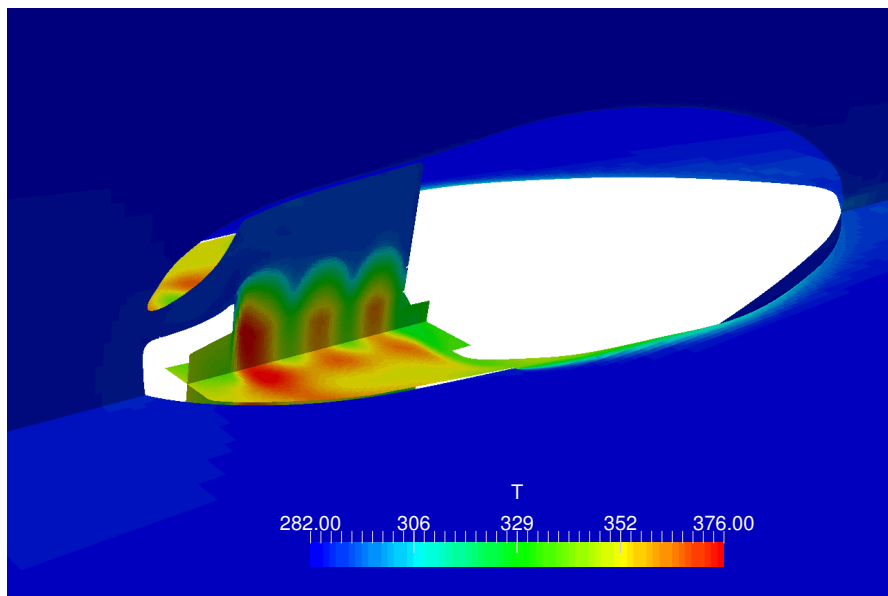
Slika 0.11: Temperaturna raspodjela Nusseltovog modela.
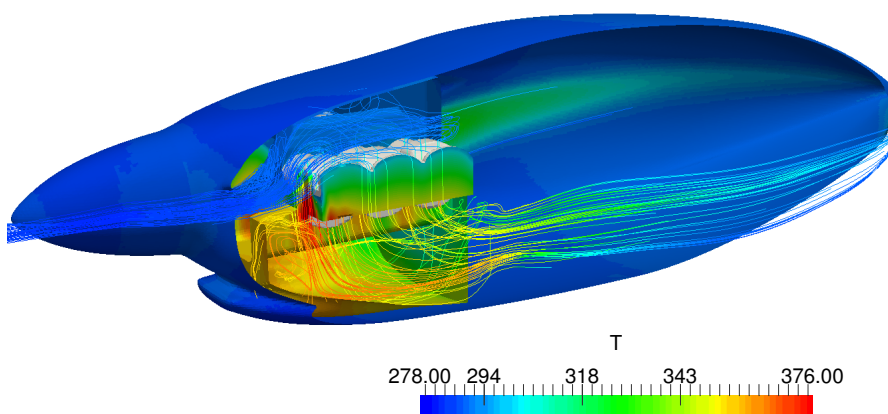
Slika 0.12: Temperaturna raspodijela sa strujnicama Nusseltovog modela.

1 | Introduction

The design and development process of a light aircraft consists of many steps involved in analysis of a system. One of them are thermal management and flow field analysis which are used to improve engine performance and environmental requirements for light aircraft. One of the influence on the engine performance is the cooling system efficiency. Flow field around the engine and flow characteristic of the inlet stream greatly affect efficiency. This characteristic of the flow has additional tangential velocity in presence of a propeller, as it is often mounted in front of a diffuser. In order to make reliable results of the flow field, wind tunnel and in-flight experimental results are used. High costs and long period of design can be reduced by introducing computational fluid dynamics (CFD). It is pointed out that CFD provides a better understanding of the flow phenomena in the engine compartment, compared to for the experiments with improving the performance of the engine cooling system and reducing the component temperature in the engine compartment in the initial stage of development [11]. It can also be used to predict the airflow and temperature distributions in the engine compartments, so it helps to find and improve the problem of heat dissipation within the engine [12]. Modeling of air cooled ribs in CFD is impractical [10], therefore engine with its ribs will be studied as a single part. In order to introduce physical behavior of fluid through the engine and achieve sufficient accuracy, robustness and simplicity, a porous media is modeled. The porous media or the porous material is a material containing pores (voids) and used as a simplification for modeling engine with cooler. The skeletal portion of the material is often called the matrix or frame. The pores are typically filled with a fluid (liquid or gas).

Depending on the design of the inlet diffuser, the cooling efficiency is largely affected by direction and drag of the air flow incoming into the engine compartment. By increasing the diffuser cross-section area, the cooling mass flow rate increases as well, while drag can be reduced by maintaining the flow through the compartment parallel to the freestream direction, while lowest drag is obtained for undisturbed flow [13]. In other words, if the diffuser is optimized for given propeller, efficiency of operating point of cooling will be increased. Motivated by these conclusions, thesis concept consist of the propeller simulations in order to obtain thrust and torque, which are needed for actuator disk theory.

Another importance is to assume correct heat transfer from air-cooled ribs to air around. The study of the cylinder temperature is divided in two process: first, the transfer heat from the combustion engine to cylinder, and second, the transfer of heat from the cylinder through the fins to the cooling air. From a perspective of heat-transfer theory second process will be set up and calculated from semi empirical expressions [10]. They consist of the user defined constants for the certain engine.

Thesis Outline

The work in this thesis can be briefly summarized, as follows: Chapter (2.), contains a detailed overview of the conservation of mass, linear momentum (Navier-Stokes equations), and energy. It is followed by introducing turbulence modeling and explanation of the shear stress transport (k-ω SST) model. Final section in this chapter is multiple reference of frame method, that describes Navier-Stokes equations in the rotating frame. Chapter (3.), deals with numerically discretized scalar transport equation using the finite volume method. As using steady and transient simulations in this thesis, PISO and SIMPLE algorithm are described. Final, it ends with porous media implementation where three heat exchanger models are presented. First is **Total Volumetric Heat** model, second is **Single stream** model and third **Nusselt** model.

Chapter (4.) is presenting geometry and mesh domain for propeller case and engine cooling system with all settings needed in the simulations. A method of inserting needed characteristic of porous media and heat transfer in order to obtain results is also described. In Chapter (5.) results are presented. Compressible effects of the propeller are studied and compare with incompressible steady results and transient results. Finally,

comparison and performance map for eight operating points is assembled. The last part of Chapter (5.) consists of validation of test cases and flow field visualization of engine cooling system. With calculated thrust and moment data, existing cooling case is upgraded with actuator disk theory. Comparison of heat effects and influence of propeller on the flow field at cooling system case is presented.

2 | Mathematical Modeling

In this chapter the mathematical model applied is presented. In order to describe a numerical procedure, the introduction into governing equations is needed. The turbulent flow field is calculated from the Navier-Stokes equation, and the temperature field is calculated from the energy equation in order to obtain the desired flow field distribution.

2.1. Navier-Stokes Equations

The Navier–Stokes equations are strictly a statement of the balance of momentum. To fully describe the fluid flow, more information is needed, depending on how many assumptions are made. This additional information may include boundary data, conservation of mass, balance of energy, and/or an equation of state. These equations can be used to model a wide range of fluid flow configurations: e.g. flow over 2D airfoil, or a complicated geometry such as fluid flow through rotor and stator blades in turbomachinery. Equations can be written in Eulerian or Lagrangian approach of fluid flow [1]. In the Lagrangian specification of flow field observer follows individual particle as it moves through space and time. Plotting the position of the individual parcel through time gives the path line of the parcel. The Eulerian specification of the field is a way of fluid motion that focuses on the specific locations in the space through which fluid flows as the time passes. In this thesis, Eulerian approach is used. First, conservation of mass is presented in the form of the continuity equation (2.1.1.), followed by the conservation of linear momentum (2.1.2.), and energy conservation equation (2.1.3.).

2.1.1. Conservation of Mass

Also known as continuity equation, mass conservation equation is defined such that, in absence of mass sources and sinks, the control volume will conserve mass:

$$\frac{\partial \rho}{\partial t} + \nabla \cdot (\rho \mathbf{u}) = 0 \,, \tag{2.1}$$

where ρ is the density, and $\mathbf{u}$ is velocity. For incompressible flow we assume that pressure change does not effect the density, the equation reduces to:

$$\nabla \cdot \mathbf{u} = 0 \,, \tag{2.2}$$

which defines continuity equation for incompressible flow.

2.1.2. Conservation of Linear Momentum

The conservation of linear momentum defines that in absence of any external force acting on body, the body retains its total momentum. First, the equation can be written in non-conserved form with material derivative:

$$\frac{D}{Dt}(\rho \mathbf{u}) + (\rho \mathbf{u} \cdot \nabla \mathbf{u}) + f = 0 \,, \tag{2.3}$$

and expanding the material derivative of momentum term and regrouping:

$$\rho \frac{D\mathbf{u}}{Dt} + \mathbf{u} \left(\frac{D\rho}{Dt} + \rho \nabla \cdot \mathbf{u} \right) = \mathbf{f} \,. \tag{2.4}$$

It can be seen that the rate of density change in the continuity equation (2.1) depends on the divergence of momentum ($\rho \mathbf{u}$) in the momentum equation above:

$$\frac{\partial \rho \mathbf{u}}{\partial t} + \nabla \cdot (\rho \mathbf{u} \otimes \mathbf{u}) = \mathbf{f} \,, \tag{2.5}$$

where $\mathbf{f}$ is a force which can be divided into surface ($\mathbf{f_s}$), and body forces ($\mathbf{f_b}$). Surface forces are caused by pressure and viscous stress, so we can write

$$\Sigma = - \begin{bmatrix} p & 0 & 0 \\ 0 & p & 0 \\ 0 & 0 & p \end{bmatrix} + \begin{bmatrix} \tau_{xx} & \tau_{xy} & \tau_{xz} \\ \tau_{yx} & \tau_{yy} & \tau_{yz} \\ \tau_{zx} & \tau_{zy} & \tau_{zz} \end{bmatrix} = -p\mathbf{I} + \tau \,, \tag{2.6}$$

where $\mathbf{I}$ is the identity tensor and τ is deviatoric or viscous stress tensor. Conservative form of the surface force after applying the divergence theorem can be written as

$$\mathbf{f_s} = -\nabla p + \nabla \cdot \tau \,. \tag{2.7}$$

Body forces typically occur in force fields, such as: gravitational field, rotating and magnetic field. In the case of rotating field, we can write:

$$\mathbf{f_b} = -2\rho[\omega \otimes \mathbf{u}] - \rho[\omega \otimes (\omega \otimes \mathbf{r})] \,, \tag{2.8}$$

where the first term represents the Coriolis force, and the second term represents centrifugal forces, the rotating frame effects and equations will be described in section (2.3.). To define the stress tensor, Newtonian fluids will be presented where the relation between the stress tensor and strain rate is a linear function. It is defined as:

$$\tau = \mu(\nabla \mathbf{u} + (\nabla \mathbf{u})^T) + \lambda(\nabla \cdot \mathbf{u})\mathbf{I} \,, \tag{2.9}$$

where μ is dynamic viscosity coefficient, and λ the bulk viscosity coefficient. Divergence of the stress tensor is:

$$\nabla \cdot \tau = \nabla \cdot \left[\mu(\nabla \mathbf{u} + (\nabla \mathbf{u})^T) \right] + \nabla(\lambda \nabla \cdot \mathbf{u}) \,. \tag{2.10}$$

Inserting equations (2.7), (2.8) and (2.10) into (2.5), the final conservative form of the linear momentum equation of Newtonian fluids becomes:

$$\frac{\partial}{\partial t}(\rho \mathbf{u}) + \nabla \cdot (\rho \mathbf{u} \otimes \mathbf{u}) = \nabla(\mu \nabla \mathbf{u}) - \nabla p + \mathbf{Q^V} \,, \tag{2.11}$$

where $\mathbf{Q^v}$ consists of body forces, forces caused, by internal shear stresses, and forces caused by bulking into the control volume:

$$\mathbf{Q^v} = \left(\nabla \cdot (\mu \nabla \mathbf{u})^T \right) + \nabla(\lambda \nabla \cdot \mathbf{u}) + \mathbf{f_b} \,. \tag{2.12}$$

For incompressible flow, the divergence of velocity is zero (2.2), and the momentum equation reduces to:

$$\frac{\partial}{\partial t}(\rho \mathbf{u}) + \nabla \cdot (\rho \mathbf{u} \otimes \mathbf{u}) = \nabla p + \mu \nabla^2 \mathbf{u} + \mathbf{f_b} \,, \tag{2.13}$$

where μ is constant.

2.1.3.   Conservation of Energy

Energy conservation equation is essentially the law of thermodynamics. It states that energy cannot be created or destroyed, it can just be transformed (mechanical, kinetic, nuclear, chemical,.. etc.). In other words, sum of all forms of energy remains constant in an isolated system:

$$\left(\frac{dE}{dt}\right)_{MV} = \dot{Q} - \dot{W} \,, \tag{2.14}$$

where the sign convention is that added heat and work done by the control volume are positive values. E is the total energy of material volume, $\dot{Q}$ is the rate of heat exchange and $\dot{W}$ the rate of work done inside material volume. In addition, equation (2.14) states that the rate of change of energy of the material volume is equal to added heat and work extracted through its boundaries. $\dot{Q}$ and $\dot{W}$ can be divided and written as:

$$\left(\frac{dE}{dt}\right)_{MV} = \dot{Q}_v + \dot{Q}_s - \dot{W}_v - \dot{W}_s \,, \tag{2.15}$$

where index v represents volume and s surface. In the Eulerian form, by applying the Reynolds transport theorem, conservation of energy can be written as:

$$\frac{\partial \rho e}{\partial t} + \nabla \cdot (\rho \mathbf{u} e) = -\nabla \cdot (p\mathbf{u}) + \nabla \cdot (\tau \cdot \mathbf{u}) - \nabla \cdot \dot{q}_s + \mathbf{f_b} + \dot{q}_V \,, \tag{2.16}$$

where e is the specific energy, $\dot{q}_V$ represents the rate of heat sources or sinks within the material volume per unit volume, and $\dot{q}_s$ is the rate of heat transfer across the surface area of the material element. The energy equation can be written in terms of specific internal energy, static enthalpy, total enthalpy, etc., depending on the problem.

2.2.   Turbulence Modeling

Fluid flow can be classified as laminar or turbulent. Laminar flows are stable while turbulent are chaotic, causing rapid mixing and vorticity fluctuations. Energy of a field particle can be described in terms of eddies which range from large to small eddies on time and length scale. This energy cascade is developed by Kolmogorov [2], [3], whose theory of turbulence is mostly accepted. Another measure of turbulence is the Reynolds number and it is the ratio of inertial and viscosity forces. As inertial forces become larger than the flow transits from laminar to turbulent. Kolmogorov theory introduces

different size eddies that have a certain amount of energy, depending on size. Large eddies break up into smaller and the energy is transformed through the cascade. The smallest Kolmogorov length and time scales are

$$\begin{aligned} \eta &= \frac{\nu^3}{\varepsilon} \\ t_\eta &= \frac{\nu}{\varepsilon} \,, \end{aligned} \tag{2.17}$$

where ν is the molecular kinematic viscosity and ϵ the average dissipation of turbulent kinetic energy. In addition, DNS and LES approach are described. Direct Numerical Simulation (DNS) is characterized by the use of a very small time step limited by the Courant number which has to be < 1 and fine mesh where $\Delta x < \eta$, causing a large number of cells in order to resolve the entire spectrum of temporal and spatial turbulent scales involved. As it is time consuming, and computationally more intensive another approach is Large Eddy Simulation (LES) approach: large eddies are directly simulated whereas small turbulent scales are modeled using sub-grid scale models. Introducing Reynolds averaging method to decompose values into mean and fluctuating parts:

$$\begin{aligned} \mathbf{u} &= \overline{\mathbf{u}} + \mathbf{u}' \\ p &= \overline{p} + p' \\ T &= \overline{T} + T' \end{aligned} \tag{2.18}$$

substituting $\mathbf{u}$, p, T with time-average counter parts the incompressible Reynolds-averaged Navier-Stokes equation based on time averaged variables (2.18) are obtained:

$$\frac{\partial}{\partial t}(\rho \overline{\mathbf{u}}) + \nabla \boldsymbol{\cdot} (\rho \overline{\mathbf{u}} \otimes \overline{\mathbf{u}}) = -\nabla \overline{p} + (\nabla \boldsymbol{\cdot} (\overline{\tau} - \rho \overline{\mathbf{u}'} \otimes \overline{\mathbf{u}'})) + \overline{\mathbf{f}_b} \tag{2.19}$$

The term $-\rho \overline{\mathbf{u}'} \otimes \overline{\mathbf{u}'}$ is known as the Reynolds stress tensor $\tau^{\mathbf{R}}$ which has six new unknown components in the momentum equation. The problem of the new added unknowns is solved by introducing the turbulent model equations in the stress components are expressed only in terms of mean components. Modeling of Reynolds stress tensor is based on Boussinesq Hypothesis [2] where it is expressed as a linear function of the mean velocity gradient:

$$\tau^{\mathbf{R}} = -\rho \overline{\mathbf{u}'\mathbf{u}'} = \mu_t \left(\nabla \mathbf{u} + (\nabla \mathbf{u})^T \right) - \frac{2}{3}(\rho k + \mu_t(\nabla \boldsymbol{\cdot} \mathbf{u}))\mathbf{I} \,, \tag{2.20}$$

where μ_t is the turbulent eddy viscosity and for incompressible flow, it is further reduced to:

$$\tau^{\mathbf{R}} = -\rho\overline{\mathbf{u'}\mathbf{u'}} = \mu_t\left(\nabla\mathbf{u} + (\nabla\mathbf{u})^T\right) - \frac{2}{3}\rho k\mathbf{I}\,. \tag{2.21}$$

Turbulent kinetic energy is defined as:

$$k = \frac{1}{2}\overline{\mathbf{u'}\cdot\mathbf{u'}}\,. \tag{2.22}$$

Turbulent thermal fluxes are calculated in a way similar to Fourier law:

$$\dot{\mathbf{q}}^{\mathbf{T}} = -\rho c_p\overline{T'\mathbf{u'}} = k_t\nabla T\,, \tag{2.23}$$

where k_t is the turbulent thermal diffusivity. There are many ways of modeling equations (2.20) and (2.23). The models are grouped in four categories:

- Algebraic (Zero-Equation) Models

- One-Equation Models

- Two-Equation Models

- Second-Order Closure Models.

All cases in this thesis have been run with k-ω SST turbulence model, which belongs to two-equation models and will be explained next.

The Shear Stress Transport k-ω SST Model

The k - ω SST model is a two-equation turbulence model consisting of the specific energy dissipation equation and the equation for turbulent kinetic energy [4]. Equation for the turbulent kinetic energy is:

$$\frac{\partial}{\partial t}(\rho k) + \nabla\cdot(\rho\overline{\mathbf{u}}k) = \nabla\cdot(\mu_{effk}\nabla k) + Q^k\,, \tag{2.24}$$

where Q^k is defined as:

$$Q^k = \tilde{P}_k - \beta^*\rho k\omega\,. \tag{2.25}$$

The modified production of turbulence kinetic energy P_k is calculated as:

$$\tilde{P}_k = \min(P_k, c_1\epsilon)\,, \tag{2.26}$$

and the original production of the turbulence kinetic energy is calculated as:

$$P_k = \tau^{\mathbf{R}} \otimes \nabla \mathbf{u} \,. \tag{2.27}$$

Turbulence dissipation is defined as:

$$\omega = \frac{\epsilon}{C_\mu k} \,. \tag{2.28}$$

A second transport equation is solved for the scale of turbulence:

$$\frac{\partial}{\partial t}(\rho\omega) + \nabla \cdot (\rho\bar{\mathbf{u}}\omega) = \nabla \cdot (\mu_{effk}\nabla\omega) + Q^\omega \,. \tag{2.29}$$

Finally, ϕ, a blending function is given as:

$$\phi = \phi_1 F_1 + \phi_2(1 - F_1) \,. \tag{2.30}$$

For the given function, complementary relations are given next. Firstly, the modified turbulent viscosity μ_t:

$$\mu_t = \frac{\rho a_1 k}{\max(a_1\omega, \sqrt{2}S_t F_2)} \,, \tag{2.31}$$

where a_1 is 0.31, S_t is the magnitude of the strain stress calculated as $\frac{1}{2}(\nabla\mathbf{v} + \mathbf{v}^T)$, and F_2 is given by:

$$F_2 = \tanh\left(\max\left(2\frac{\sqrt{k}}{\beta^2\omega(d_\perp)}, \frac{500\nu^2}{d_\perp}\omega\right)^2\right) \,. \tag{2.32}$$

and F_1 is calculated as:

$$F_1 = \tanh((\gamma_1)^4)$$
$$\gamma_1 = \min\left(\max\left(\frac{\sqrt{k}}{\beta^*\omega(d_\perp)}, \frac{500\nu}{(d_\perp^2\omega)}\right), \frac{4\rho\sigma_{\omega 2}k}{CD_{\omega k}d_\perp^2}\right) \tag{2.33}$$
$$CD_{\omega k} = \max\left(2\rho\sigma_{\omega 2}\frac{1}{\omega}\nabla k \cdot \nabla\omega, 10^{-10}\right) \,.$$

Following constants in Table (2.1) are used. As complementary equations are used, additional relations for thermal conductivity and effective turbulent viscosities for k and ω are computed as:

$$k_t = \frac{\mu_t}{Pr_t}$$
$$\mu_{eff,k} = \mu + \frac{\mu_t}{\tilde{\sigma}_k} \tag{2.34}$$
$$\mu_{eff,\omega} = \mu + \frac{\mu_t}{\tilde{\sigma}_\omega}$$

Table 2.1: k - ω SST turbulence model coefficients.

$C_{\alpha 1}$	$C_{\alpha 2}$	$C_{\beta 1}$	$C_{\beta 2}$	β^*	σ_{k1}	σ_{k2}	$\sigma_{\omega 1}$	$\sigma_{\omega 2}$	c1	Pr_t
0.5532	0.4403	0.075	0.0828	0.09	2	1.0	2	2.186	10	0.9

2.3.   Multiple Reference Frame Model

The MRF model is a steady-state approximation technique in computational fluid dynamics which is manly used to simulate rotating machinery. It is robust and relatively simple to use. It assumes that every assigned volume cell on each radius has constant rotational velocity, and the non-wall boundaries are surfaces of revolution. The computational can be divided into several zones which are moving at different rotational and translational speeds. Also, if there is no angular velocity acting on the selected zone, stationary equations are used. It is also called the "frozen rotor approach" [9] because the whole computational mesh (domain) remains fixed, meaning that fluid flow of the moving part is simulated for one specified position. An alternative to MRF is the moving/sliding mesh technique which can deal with strong interactions at the boundaries between moving and stationary zones, but since it is a transient approach it is typically very time consuming [14]. On the other hand MRF approach cannot take into account the transient effects, but it can be used to calculate the initial conditions for a transient flow simulation.

Naiver-Stokes Equations in the Rotating Frame

Navier-Stokes equation for cells which are part of the rotating zone have to be modified. A general equation where $\mathbf{A}$ is a vector and a ω is the constant angular velocity, is defined:

$$\left[\frac{dA}{dt}\right]_I = \left[\frac{dA}{dt}\right]_R + \omega \times \mathbf{A} \, . \tag{2.35}$$

To specify the position of the acting angular velocity of a cell, vector $\mathbf{r}$ is introduced in equation (2.35):

$$\left[\frac{d\mathbf{r}}{dt}\right]_I = \left[\frac{d\mathbf{r}}{dt}\right]_R + \omega \times \mathbf{r} \, , \tag{2.36}$$

and it can be written as:

$$\mathbf{u_I} = \mathbf{u_R} + \omega \times \mathbf{r} \, . \tag{2.37}$$

The angular acceleration is defined as the time derivative of equation (2.37) in inertial frame of reference:

$$\left[\frac{d\mathbf{u_I}}{dt}\right]_I = \left[\frac{\mathbf{u_I}}{dt}\right]_R + \frac{d\omega}{dt} \times \mathbf{r} + 2\omega\mathbf{u_R} + \omega \times \omega \times \mathbf{r} \,, \tag{2.38}$$

where every therm has a physical meaning:

- $\frac{d\omega}{dt} \otimes \mathbf{r}$ tangential acceleration

- $2\omega\mathbf{u_R}$ Coriolis acceleration

- $\omega \times \omega \times \mathbf{r}$ centrifugal acceleration.

After defining these additional terms, they can be added to the conservation equations for compressible flow (2.1), (2.12) and (2.16), in absolute velocity formulation:

$$\frac{\partial \rho}{\partial t} + \nabla \boldsymbol{\cdot} (\rho\mathbf{u_R}) = 0$$

$$\frac{\partial}{\partial t}(\rho\mathbf{u_I}) + \nabla \boldsymbol{\cdot} (\rho\mathbf{u_R}\mathbf{u_I}) + \rho(\omega \times \mathbf{u_I}) = -\nabla p + \mu\nabla^2\mathbf{u_I} + \mathbf{f} \tag{2.39}$$

$$\frac{\partial}{\partial t}(\rho E) + \nabla \boldsymbol{\cdot} (\rho\mathbf{u_R}H + p\mathbf{u_R}) = \nabla \boldsymbol{\cdot} (k\nabla T + (\mu\nabla^2\mathbf{u_I}) \boldsymbol{\cdot} \mathbf{u_I}) + \mathbf{S} \,.$$

In this formulation the Coriolis and centrifugal acceleration can be combined into a single term $(\omega \times \mathbf{u})$ as:

$$\omega \times \mathbf{u_I} = \omega \times (\omega \times \mathbf{r}) + 2\omega \times \mathbf{u_I} \tag{2.40}$$

3 | Computational Fluid Dynamics Modeling

3.1. Finite Volume Method

Finite volume method is a numerical method based on transforming partial differential equations into a set of linear algebraic equations. It is a well-known method [1], widely used for a range of engineering problems. The domain is discretized into a finite number of non-overlapping control volumes, with computational points in cell centroids, where all the unknown variables are calculated. Cells are divided by cell faces, which establish the communication about the transported variable. Cell faces also have face points which are positioned at the center of the face area. For every cell point, a linear algebraic equation is obtained, and it is calculated in every time step.

Discretization of all terms in a scalar transport equation will be presented in the next section. Also, there will be a brief description of the linear system equations and the coupling of pressure and velocity will be shown.

3.2. Discretization of Scalar Transport Equation

Presented in the integral form over a material volume, the scalar transport equation is defined as:

$$\frac{\partial(\rho\phi)}{\partial t} + \nabla \cdot (\rho\mathbf{u}\phi) = \nabla \cdot (\rho\Gamma_\phi\nabla\phi) + S_\phi(\phi) \qquad (3.1)$$

ϕ is the unknown variable, defined in the central point of a cell. ρ is density, Γ_ϕ is diffusion coefficient and $\mathbf{u}$ is velocity which can also depend on variable ϕ.

Temporal Derivative

The first term is the temporal derivative. Its discretization follows the expression:

$$\int_{V_m} \frac{\partial(\rho\phi)}{\partial t} dV_m = V_m \frac{\partial(\rho\phi)^M}{\partial t} = V_m \frac{(\rho\phi)^{M_n} - (\rho\phi)^{M_o}}{\Delta t} , \qquad (3.2)$$

and begins with the linear integration [15] over a material volume which is represented by the cell volume. Inside the cell volume, the product of density and variable ϕ is needed in the current time instance C_n and old time instance C_o, with equal time step Δt. This is also called the Euler discretization and by development in Taylor's order it can be shown that it is second order accurate, but after marching in time for N steps, error order is increasing from $\sigma(\delta t^2)$ to $N\sigma(\delta t^2) \approx \sigma(\delta t)$ and it becomes first order accurate. The transport equation is a second order partial differential equation because of diffusion term, so the backward difference scheme is used:

$$V_m \frac{\partial(\rho\phi)^M}{\partial t} = V_m \frac{\frac{3}{2}(\rho\phi)^{M_n} - 2(\rho\phi)^{M_o} + \frac{1}{2}(\rho\phi)^C_{oo}}{\Delta t} , \qquad (3.3)$$

which is also second order accurate. It has the additional "old old" term and which has to be memorized for every time step. Also $(\rho\phi)t^{C_{oo}}$ is then calculated as:

$$(\phi)t^{C_{oo}} = \phi(t^{C_n} - 2\Delta t) \qquad (3.4)$$

Convection term

Since the convection term contains the gradient operator, a Gauss theorem [16] will be used which transforms the volume integral into a surface integral as follows:

$$\int_{V_m} \nabla \cdot (\rho\mathbf{u}\phi) dV_m = \sum_f \mathbf{S}.(\rho\mathbf{u}\phi)^f = \sum_f \mathbf{S}.(\rho\mathbf{u})^f \phi^f = \sum_f \mathbf{F}\phi^f . \qquad (3.5)$$

Vector $\mathbf{F}$ is, mass flux, defined as product of velocity and density defined in face center. The equation demands definition of variable ϕ in faces of the control volume, so convection interpolation scheme is made between cells who share this face. There are a lot different interpolation schemes, most popular are Central Differencing (CD), Upwind Differencing (UD), and other such as TVD (Total Variation Diminishing) and NVD (Normalized Variable Diagram) schemes. CD scheme is second order accurate and it is not bounded, which is the main reason why it is not widely used. UD scheme is first

order accurate and is unconditionally bounded, but it is the cause of numerical diffusion. In order to have both stable and accurate results, TVD and NVD schemes are used. For additional information the reader is referred to [16].

Diffusion Term

Discretization process of the diffusion term in transport scalar equation:

$$\int_{V_m} \nabla \cdot (\rho \Gamma_\phi \nabla \phi) dV_m = \sum_f \mathbf{S}.(\rho \Gamma_\phi \nabla \phi)^f = \sum_f (\rho \Gamma_\phi)^f \mathbf{S}.(\nabla \phi)^f . \tag{3.6}$$

If the mesh is orthogonal,it is possible to use the following expression:

$$\mathbf{S}.^f (\nabla \phi)^f = |\mathbf{S}| \frac{\phi^S - \phi^M}{|\mathbf{d}|} . \tag{3.7}$$

The pair of adjacent cells with cell centers in points S and M sharing the same face $\mathbf{S}^f$. As a difference between adjacent cell center values of ϕ. $\mathbf{d}$ is the distance between these adjacent cell center points. Finally, it can be written as:

$$(\rho \Gamma_\phi)^f \mathbf{S}.(\nabla \phi)^f = \sum_f (\rho \Gamma_\phi)^f \frac{\phi^S - \phi^M}{\mathbf{d}} . \tag{3.8}$$

Mesh orthogonality is not always possible to satisfy. In that case the product $\mathbf{S}.^f (\nabla \phi)^f$ is split to two parts:

$$\mathbf{S}.^f (\nabla \phi)^f = \mathbf{\Delta}.(\nabla \phi)^f + \mathbf{k}.(\nabla \phi)^f , \tag{3.9}$$

where first term is orthogonal contribution, and second non-orthogonal convection. Two vectors $\mathbf{\Delta}$ and $\mathbf{k}$, in equation (3.9) have got to satisfy the condition:

$$\mathbf{S} = \mathbf{\Delta} + \mathbf{k} , \tag{3.10}$$

where vector $\mathbf{\Delta}$ is chosen to be parallel with vector $\mathbf{d}$ and allows us to use the orthogonal contribution in equation (3.7), limiting the less accurate method only to the non-orthogonal part which can not be treated in any other way. For many existing decompositions the reader is referred to [17]. The orthogonal part of equation (3.9), where $\mathbf{d}$ and Δ are parallel, follows:

$$\mathbf{\Delta}.(\nabla \phi)^f = |\mathbf{\Delta}| \frac{\phi^S - \phi^M}{|\mathbf{d}|} . \tag{3.11}$$

The final form of discretized diffusion term using equation (3.9) is:

$$\mathbf{S}.(\nabla\phi)^f = |\mathbf{\Delta}|\frac{\phi^S - \phi^M}{|\mathbf{d}|} + \mathbf{k}(\nabla\phi)^f . \tag{3.12}$$

The face interpolate of $\nabla\phi$ is calculated:

$$\nabla\phi = f_x(\nabla\phi)^S + (1 - f_x)(\nabla\phi)^M . \tag{3.13}$$

Source/Sink Term

Sinks or source terms can easily be discretized as:

$$\int_{V_m} S_\phi(\phi)dV_m = S_\phi(\phi)V_m , \tag{3.14}$$

where S_ϕ is a function which can be linear or non linear, depending on the case. At last we discrete all terms in scalar transport equation. In the next section, linear system of algebraic equations obtained by discretization will be explained.

Linear System of Discretized Equations

Discretized form of the scalar transport equation is:

$$V_m\frac{(\rho\phi)^{M_n} - (\rho\phi)^{M_o}}{\Delta t} + \sum_f \mathbf{F}\phi^f - \sum_f (\rho\Gamma_\phi)^f\mathbf{S}.^f(\nabla\phi)^f = S_\phi(\phi)V_m , \tag{3.15}$$

containing temporal and source/sink terms defined via variables at the cell centers and convection and diffusion terms defined for face centers, where interpolation schemes are used. Linear system is represented as:

$$a^M\phi^{M_n} + \sum_f a^S\phi^{S_n} = b , \tag{3.16}$$

where variable ϕ^{S_n} belongs to neighboring cell, which shares the face f. For the entire domain, the system of equations can be written as:

$$\mathbf{A}\mathbf{x} = \mathbf{b} . \tag{3.17}$$

Matrix $\mathbf{A}$ is a N $\times$ N square matrix, where N is the number of cells in the domain. $\mathbf{x}$ is the vector of variables and $\mathbf{b}$ is the right-had-side, containing boundary conditions and other known coefficients.

3.3.   Coupling Velocity and Pressure

Solving the pressure-velocity coupling is the main challenge for majority of problems in CFD. Large number of algorithms where proposed for solving the pressure-velocity coupling, and in this thesis PISO and PIMPLE algorithm will be used [1]. In Navier-Stokes equations is a strong coupling between pressure and velocity contributed by appearance of velocity divergence in the momentum equation (2.3), and pressure divergence in the pressure equation. First, the pressure equation derivation will be presented, and in the next section SIMPLE and PISO algorithms will be briefly explained.

3.3.1.   Pressure Equation

To define the coupling of velocity and pressure, the pressure equation has to be derived. The main idea is that pressure field needs to satisfy the continuity equation. Beginning from the discretized Naiver-Stokes equations:

$$a^M \mathbf{u}^{Mn} = -\sum_S a^S \mathbf{u}^{S_n} + S^0 - V_M \nabla P^M \ , \tag{3.18}$$

introduce $H(\mathbf{u})$ operator [17] to obtain the reduced form:

$$a^M \mathbf{u}^{Mn} = H(\mathbf{u}) - V_M \nabla P^M \ . \tag{3.19}$$

When equation (3.18) is solved in a certain time step it is written:

$$\mathbf{u}^{Mn} = \frac{1}{a^M} H(\mathbf{u}) - V_M \frac{1}{a^M} \nabla P^M \ , \tag{3.20}$$

and after interpolation from cell center to face center, it can be written as:

$$\mathbf{u}^{fn} = \frac{1}{a^f} H(\mathbf{u}) - V_M \frac{1}{a^f} \nabla P^f \ , \tag{3.21}$$

and the continuity equation is already discretized as:

$$\sum_f \mathbf{s}^f \mathbf{u}^f = 0 \ . \tag{3.22}$$

When equation (3.21) is inserted into equation (3.22), it can be said that field of velocity is solenoidal:

$$\sum_f \mathbf{s}^f V_M \frac{1}{a^f} \nabla P^f = \sum_f \mathbf{s}^f \frac{1}{a^f} H^f(\mathbf{u}) \ . \tag{3.23}$$

3.3.2.   SIMPLE Algorithm

SIMPLE abbreviation is for "Semi Implicit Method for Pressure Linked Equations"
and it is an iterative method for solution of steady state problems developed by prof.
Brian Spalding in the 1970s. The main steps in solution procedure [1] are:

- First, to calculate the velocity, implicitly relaxed momentum equation is solved

$$\frac{a^M}{\alpha_u}\mathbf{u}^{M_n} = H(\mathbf{u}) - \sum_f \mathbf{s}^f p^f + \frac{1-\alpha_u}{\alpha_u}\mathbf{u}^{M_o} \tag{3.24}$$

  with the previous or boundary values of the pressure field

- Using the calculated velocity, operator $H(\mathbf{u})$ can be used for solving the pressure
  field from (3.23).

- The conservative flux is then calculated

$$F = \rho^f \mathbf{S}^f \mathbf{u}^f = \rho^f \mathbf{s}^f \left(\frac{1}{a_f} H^f(\mathbf{u}) - V_M \frac{1}{a^f}\nabla P^f \right), \tag{3.25}$$

  but it carries a residual error, so it has to be explicitly relaxed

$$p^n = p^o + \alpha_p(p^n - p^o), \tag{3.26}$$

  where p^n is result for the pressure field. This equation is ensuring that convergence
  will be achieved, but just part of old result is taken for new. Suggested values for
  relaxation are

$$\begin{aligned} \alpha_u &= 0.8 \\ \alpha_p &= 0.2 \, . \end{aligned} \tag{3.27}$$

3.3.3.   PISO Algorithm

PISO is an abbreviation for "Pressure Implicit with Splitting of Operator". It is
originally developed for solving non iterative unsteady compressible flow by Issa 1986.
The procedure is [1]:

- To calculate velocity, the discretized momentum equation is solved (3.18). As the
  pressure field is unknown, if the value is used from value of the previous iteration,
  or from the boundary field. For linearization of the equation, velocity is also taken
  from the previous step. Solution of the system in not solenoidal. This step is
  called momentum predictor.

- Operator $H(\mathbf{u})$ can be calculated from the pressure gradient and by the solving the equation (3.23), the new pressure field is obtained. This step is called the pressure solution.

- Equation (3.25) gives new fluxes which are conservative and consistent with the pressure field. New velocity field has to be calculated using the following expression:

$$\mathbf{u}^{f_n} = \frac{1}{a^f} H^f(\mathbf{u}) - V_M \frac{1}{a_f} \nabla P^f \ . \tag{3.28}$$

First term is proportional to the correction of velocity from adjacent cells $H(\mathbf{u})$ and the second term is the correction of velocity from the pressure gradient. First term is negliable. To obtain good results, it is necessary to:

  - correct the operator $H(\mathbf{u})$ with explicit by corrected values of velocity

  - formulate the new equation for pressure and solve it

  - repeat the procedure until convergence is achieved.

3.4.   Rotor-Stator Interface Modeling

In this thesis a rotor-stator interference is used for the purpose of multi reference frame (MRF) simulations. Usually these interfaces are used in turbo-machinery in cases of complex geometries, where the grid on either side of two connected surfaces does not match. In this thesis, the cases are represented in two ways: first where mesh is moving and second where mesh is not physically moving (frozen rotor approach) [9]. In both cases boundaries have to be able to communicate between stationary and rotational part of the mesh. The boundaries which connect rotational and stationary zones require axisymetric interface patches. Other boundaries that are implemented are periodic boundaries which reduce computational time by reducing the number of cells in domain. In addition, numerical grid is often made in a way that the finer mesh is in the area close to the geometry and coarser mesh is in the far field. So the boundaries of adjacent meshes are non-conforming. This problem cannot be solved by adjusting mesh topology, but rather by using general grid interfaces.   In Figure (3.1) MRF zone can be seen colored in red. It is a rotational part of the mesh and the mesh is not moving, so `ggi` patches are required. On the other hand, for transient simulations where mesh
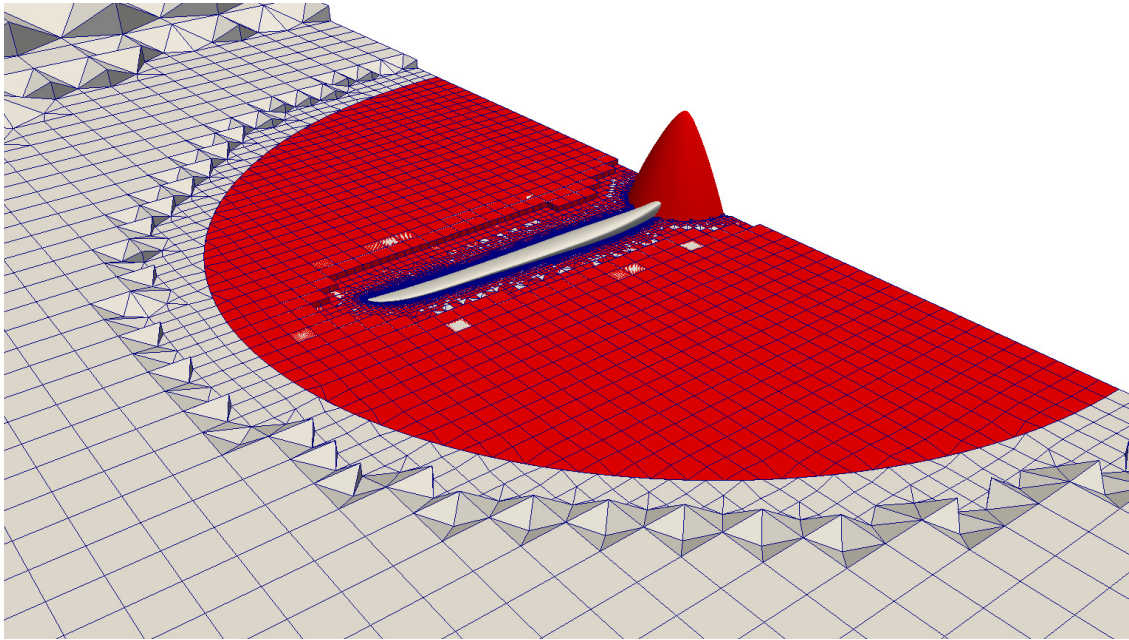
Figure 3.1: Ggi interface of MRF zone

is moving, `overlapGgi` patches between rotational and stationary part of the mesh are required. In addition, to reduce the number of cells in order to reduce the computational time, the case can be set up to calculate only a part of the domain. This can be done by setting up `cyclicGgi` or `cyclic` patches in `foam-extend` [14] at sliced surfaces showed in figure (3.2). Surfaces colored in blue and green reperesent a single pair of cyclicGgi patches, and red and white surface another pair of cyclicGgi.
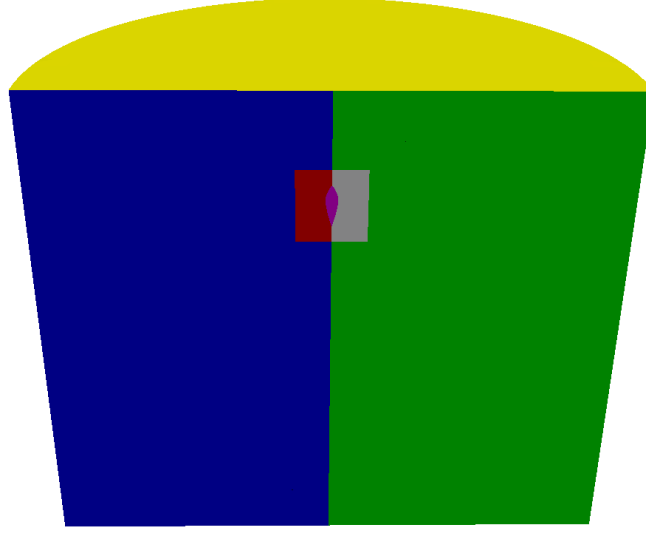
Figure 3.2: Interfaces for half domain case

General Grid Interfaces

General grid interface refers to a class of grid connections which permits non matching node locations, element type, surface shapes and different types of flow across a connection. It is a coupling interface in `foam-extend` [5] using weighted interpolation to evaluate and transmit flow values across pair of conformal or non-conformal boundaries. Flow values for master to slave patch are:

$$\phi_{S_i} = \sum_n W_{M_n to S_i} S_{M_n} \; , \tag{3.29}$$

where ϕ_M is the master patch value, $W_{M_n to S_i}$ the weight factor for master facet to shadow facet and flow values from slave to master patch are:

$$\phi_{M_j} = \sum_m W_{S_m to M_j} S_{S_m} \; , \tag{3.30}$$

where ϕ_S is the slave patch value, $W_{S_m to M_j}$ the weight factor for shadow facet to master facet. In order to achieve conservation for interface discretization, three constraints need

to be set

$$\sum_n W_{M_n to S_i} = 1$$

$$\sum_n W_{S_m to M_j} = 1 \tag{3.31}$$

$$W_{M_n to S_i}|S_{M_n}| = W_{S_m to M_j}S_{S_m} = |S_{\cup M to S}| \,,$$

where $|S_{\cup M to S}|$ is the intersection of the surface area between master and shadow patch, and S_{M_n}, S_{S_n} are surfaces of master and shadow patches respectively. Evaluation of weighting factor requires robust and precise determination because interpolation which does not strictly satisfy equation (3.31) will lead to unacceptable discretization error. Evaluation of weighting factors is from master to shadow patch faces first:

$$W_{M_n to S_i} = \frac{|S_{\cap M to S_i}|}{S_{M_n}} \,, \tag{3.32}$$

and then from shadow to master

$$W_{S_n to M_j} = \frac{|S_{\cap S to M_j}|}{S_{S_m}} \,, \tag{3.33}$$

where $|S_{\cap M to S_i}|$ and $|S_{\cap S to M_j}|$ are surface of intersections between a master and a shadow patch faces. Values of equations (3.32) and (3.33) are the percentage of surface intersection between two overlapping faces which needs to be greater then zero. In case of zero percentage (no intersection), the neighborhood determination algorithm has failed.

3.5.   Porous Media Implementation

Porous media is the interest of many CFD simulations and it is often used in thermal analysis. There are many cases where simulation of flow in complicated geometry and narrow passages is hard to calculate. In order to simulate heat transfer trough engine ribs in one of the cases in this master thesis, porous media is used. To simulate fluid flow over porous media, velocity sink is added to the momentum equation, and to introduce heat transfer over a porous zone, source of heat is added in to the energy equation. Also, a coordinate system for the porous zone has to be provided, in order to properly describe the geometry. Usually, to take the geometry into account, additional terms are provided in the momentum equations:

$$\mathbf{s} = -\left(\mu\mathbf{D} + \frac{1}{2}\rho|\mathbf{u}|\mathbf{F}\right)\mathbf{u} \,, \tag{3.34}$$

where the two terms represent viscous and inertial loss respectively. Matrices $\mathbf{D}$ and $\mathbf{F}$ are represented as scalars, and the equation is well known as Darcy-Forchheimer equation. These scalars are calculated experimentally. Momentum equation is then written as:

$$\frac{\partial}{\partial t}(\mu\rho\mathbf{u}) + \nabla\bullet(\rho\mathbf{u}\otimes\mathbf{u}) = -\nabla p\mathbf{I} + \nabla\bullet\tau + \mathbf{s}\,. \tag{3.35}$$

Value of μ can be between 0 and 1, and it represents porosity in time derivative term. The source term can be also modeled by the a power law of the velocity magnitude as

$$\mathbf{s} = -\rho C_0 |\mathbf{u}|^{\frac{C_1-1}{2}}\,, \tag{3.36}$$

where coefficients C_0 and C_1 are user defined empirical coefficients.

3.6.   Heat Exchanger Models

Sources of heat can be modeled in many ways. Some of them will be explained, and used below. The main idea is to obtain the exchange of energy in equation (2.16), where term $\dot{q_V}$ is modeled. There are two ways of transferring heat. One of them is the process of conduction connected with heat exchange inside some material, and the other is convection which is a process of transferring energy between a solid and a liquid or gas phase. In order to determine the dominance of conductive or convective heat transfer, dimensionless Nusselt number is used. It is defined as:

$$Nu = \frac{\text{Convective Heat Transfer Coefficient}}{\text{Conductive Heat Transfer Coefficient}} = \frac{\alpha_f l_0}{\lambda}\,, \tag{3.37}$$

where α_f is the convective heat transfer coefficient, l_0 characteristic length and λ is the thermal conductivity. Nusselt number is a function of Reynolds and Prandtl numbers which are defined by (3.46) and (3.49). Term $\dot{q_V}$ in equation (2.16) is calculated as

$$\dot{q_V} = \alpha_f S(T_s - T_f)\,, \tag{3.38}$$

where S is the surface of the solid, T_s is temperature of the surface and T_f is temperature of the fluid.

3.7.   Total Volumetric Heat Approach

The first model is the simplest and it has abbreviation THV. The idea is that the rate of heat is user defined, and discretized through porous zone, where every cell, depending

on its volume, has a fraction of the total rate of heat in the cell center. Following the
finite volume method, it can be written as:

$$\dot{Q}_i = \dot{Q}_{tot} \frac{V_i}{\displaystyle\sum_{i=0}^{n} V_i} \,, \tag{3.39}$$

where $\displaystyle\sum_{i=0}^{n} V_i$ is the total volume of porous zone, where rate of heat is taken into account.
This model is called the total volumetric heat model.

3.8.   Single Stream Approach

The second model is taking into account mass flow rate for a single stream [6].
This approach has abbreviation SS and can ensure that more heat can be exchanged
where mass flow is high and avoid problems that may arise in regions where mass flow
is close to zero, as in the cases of total heat model. It also takes into account the
minimum temperature difference to exclude non physical temperature field, and to limit
its temperature to the limits which are given on the boundaries. The local heat transfer
is using source defined for every cell as:

$$\dot{Q}_i = \dot{Q}_{tot} \frac{V_i u_i (T_{ref} - T_i)}{\displaystyle\sum_{i=0}^{n} V_i u_i (T_{ref} - T_i)} \,, \tag{3.40}$$

where $\dot{Q}_{tot}$ is the total heat source which has to be user defined. Variables V_i, u_i, T_i are
volume, velocity and temperature of the cell, respectively.

3.9.   Nusselt Model Approach

This model uses both single stream and total volumetric properties, by taking into
account Nusselt number which is user defined [7]. First, model heat-exchanger effective-
ness has to be defined. It can be written as the ratio of actual rate of heat capacity and
the number of transfer units using relation:

$$\epsilon = 1 - \exp\left[-\frac{1}{C_r} N_{tu}^{0.22} (1 - e^{-C_r N_{tu}^{0.78}}) \right] \,, \tag{3.41}$$

where C_r is ratio of C_{min} and C_{max}, which are defined as

$$C_{\mathrm{max}} = \max[(\dot{m}c_p)_{\mathrm{hot}}, (\dot{m}c_p)_{\mathrm{cold}}]$$
$$C_{\mathrm{min}} = \min[(\dot{m}c_p)_{\mathrm{hot}}, (\dot{m}c_p)_{\mathrm{cold}}] \, . \tag{3.42}$$

It can also be used for a single stream (cold stream) where the hot stream can be estimated as a constant in all of its variables, so only $\min[(\dot{m}c_p)_{\mathrm{hot}}]$ can be taken in equation (3.42). For this model, the heat transfer can be calculated from

$$\dot{Q}_{\mathrm{tot}} = \epsilon C_{\mathrm{min}}(T_{\mathrm{in}} - T_i) \tag{3.43}$$

where ϵ is effectiveness. T_{in} macro auxiliary fluid inlet temperature and T_i cell temperature of porous zone. If the temperature of the auxiliary fluid is constant, it can be redefined in a single stream approach. Finally heat transfer is computed for each cell as

$$\dot{Q}_{\mathrm{cell}} = \dot{Q}_{\mathrm{tot}} \frac{V_{\mathrm{i}}}{\displaystyle\sum_{i=0}^{n} V_{\mathrm{i}}} \, . \tag{3.44}$$

If there are multiple heat exchanger cores, they can be simply added as

$$q_{\mathrm{total}} \quad = \sum_{\mathrm{all\ cores}} q_{\mathrm{core}} \, . \tag{3.45}$$

To be able to set up the Nusselt model, Nusselt number has to be calculated. There are many approaches which can be used, but they are experimental and valid for only one typical case (flat plate, tube, or set of tubes). Calculation begins with the calculation of Reynolds number:

$$Re = \frac{w_\infty l_0}{\nu} \, , \tag{3.46}$$

where w_∞ is the velocity of undisturbed field, l_0 is the characteristic length and ν is viscosity the fluid. For any type of laminar flow equations are given for a flat plate case:

$$N_{tu} = 0,664 Re^{\frac{1}{2}} Pr^{\frac{1}{3}} \, , \tag{3.47}$$

and for turbulent:

$$N_{tu} = 0,023 Re^{\frac{4}{5}} Pr^{\frac{1}{3}} \, , \tag{3.48}$$

which was obtained experimentally considering that it is calculated for an averaged Nusselt number and for the forced convection. Prandtl number is defined as:

$$Pr = \frac{c_p \rho \nu}{\lambda} \, , \tag{3.49}$$

where c_p is the specific heat capacity of fluid.

4 | Geometry and Mesh Domain

In this chapter geometry and setup of used cases are presented. Two cases are simulated, depending on area of interest. First test case is a propeller-only configuration, in order to obtain torque and thrust values to be used later on the cooling case, within actuator disc method. The second test case is used for determining the heat transfer through engine and analyze cooling at cruising operating point.

4.1. Setup of Propeller Case

First step in setting up a case is to achieve accurate representation of the geometry. Industrial name of the propeller is $prop\text{-}11cyc\text{-}SA3d\text{-}0it$ and it is used with engines of light aircrafts. In order to include the propeller head into simulation, the head has been modeled as spinner in aerodynamic shape Figure (4.1). Only half of the propeller and the spinner is showed and numerically simulated. Domain is created in a shape of a half cylinder. This propeller has two blades which have no ability of changing attack angle during flight. The other half of the domain will be included using special boundary conditions which will be described below.
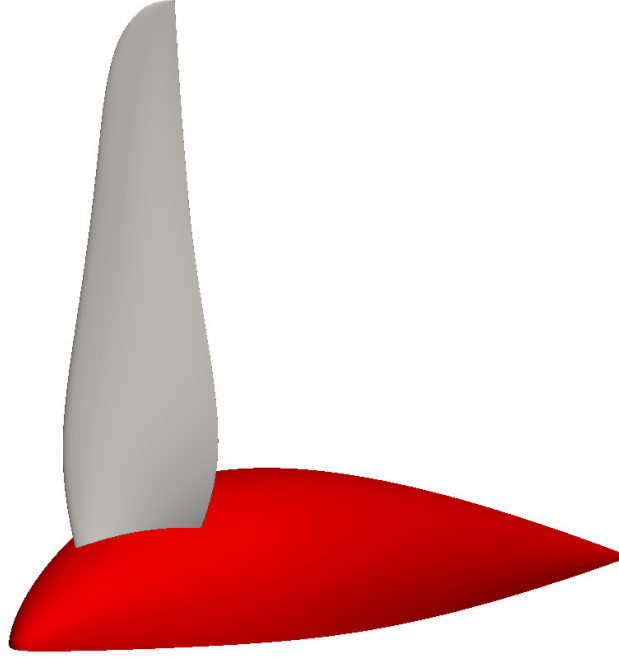
Figure 4.1: Propeller geometry

Domain of the propeller case is cylindrical with two inner cylinders for local refinement Figure (4.3). Local refinement along z axis can is needed in order to capture the propeller wake. The outer cylinder domain generally has diameters of 3D to 7D, where D is the propeller diameter. The distance between the rotating frame and inlet varies from 3D to 6D while the distance from center to outlet is between 4D and 10D. Table (4.1) shows distances chosen for mesh domain. Another zone of mesh refinement was

Table 4.1: Domain dimensions

Outer cylinder radius	10D
Inlet to MRF zone distance	3D
Center of propeller to outlet	10D
Local refinement radius (MRF Zone)	1.2D
Local refinement radius (Wake catch)	2D

generated to capture the wake behind the propeller. The process of domain discretization (meshing) was performed using automatic mesh generator called `snapyHexMesh`.

A very important part of the mesh is the boundary between rotational and stationary part, as described in Chapter 3. (4.3). First, the refined MRF zone with cylindrical shape was created. The boundary between stationary and rotational zone can be seen in Figures (4.3) and (4.4). The propeller is positioned in the center of the zone defining the rotating part of mesh. After the first step, the second mesh was created in order to make a big enough domain with fewer cells, and to make a local refinement along the wake trail. When these two meshes are created, they can be merged into one big mesh with boundaries presented in Table (4.2). The propeller domain is shown on the

Table 4.2: Boundary names and types for the propeller case.

Number	Name	Type of boundary
1.	cyclic_rightM	cyclicGgi
2.	cyclic_leftM	cyclicGgi
3.	propeller	wall
4.	spinner	wall
5.	small_cylindar_inletUS	ggi
6.	small_cylindar_linerUS	ggi
7.	small_cylindar_outletUS	ggi
8.	big_cylindar_inlet	patch
9.	big_cylindar_liner	patch
10.	big_cylindar_outlet	patch
11.	cyclic_rightV	cyclicGgi
12.	cyclic_leftV	cyclicGgi
13.	small_cylinder_inletIS	ggi
14.	small_cylinder_linerIS	ggi
15.	small_cylinder_outletIS	ggi

Figure (4.2) where local levels of refinement can be seen.
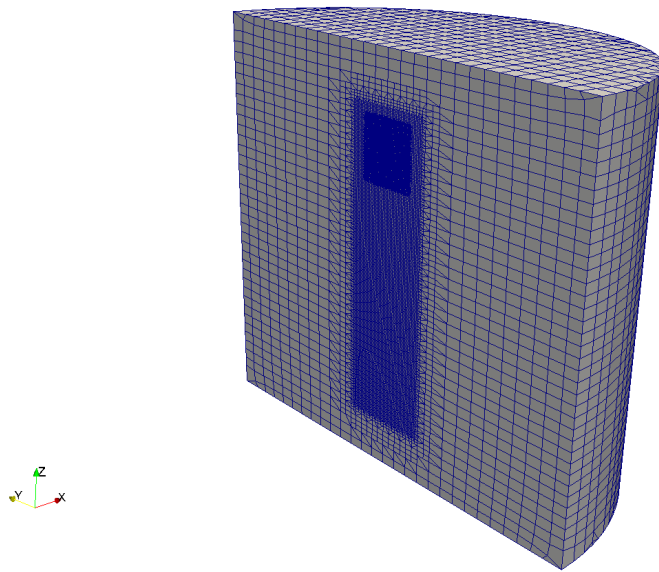
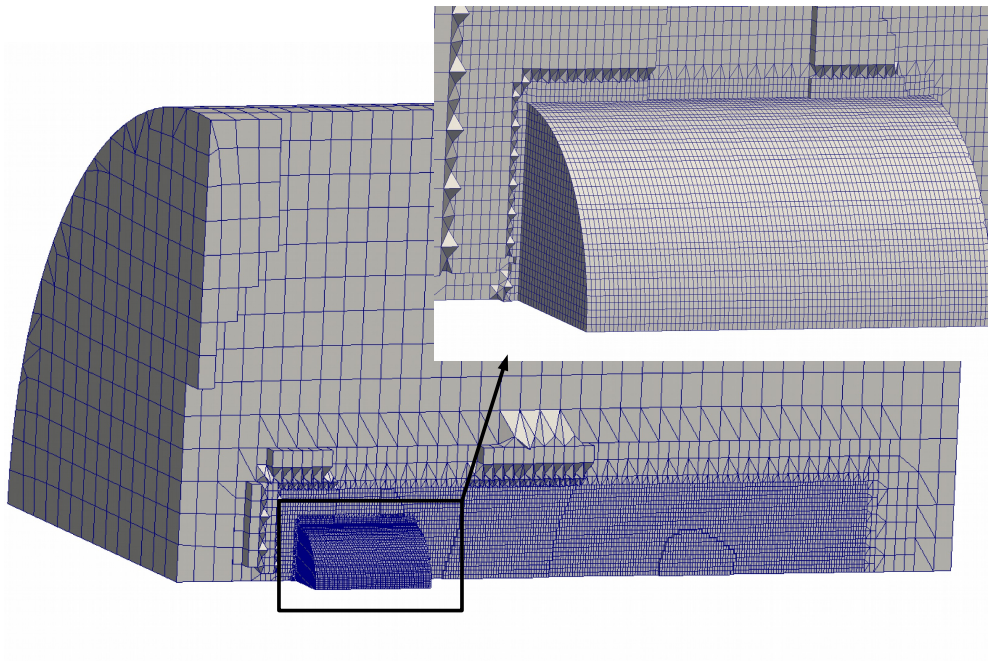Figure 4.2: Propeller domain.

Figure 4.3: Connection of MRF zone.

Meshing of the propeller tip is a sensitive problem. The shape of the tip is changing due to large curvature, and it finishes in two points at the trailing edge. Velocity and gradients of variables reach the extreme values at the tip of the propeller and it effects the results of the total moment. The smallest cells are created at the propeller tip. The limit for their size will be a ability to describe the fields of variable gradients and velocities. Another problem is the local refinement along the trailing edge, which also has an effect on final results. The boundary layer is defined by $y+$. Value of the smallest cell height is limited by local friction velocity and viscosity. The assumed maximum local friction velocity will be at the tip of propeller, where $y+$ is the highest. The smallest $y+$ is at the top of the spinner and the root of the propeller, so in addition, the height of boundary layer has to be increased. To obtain reasonable results minimum average value of y+ has to be 20.
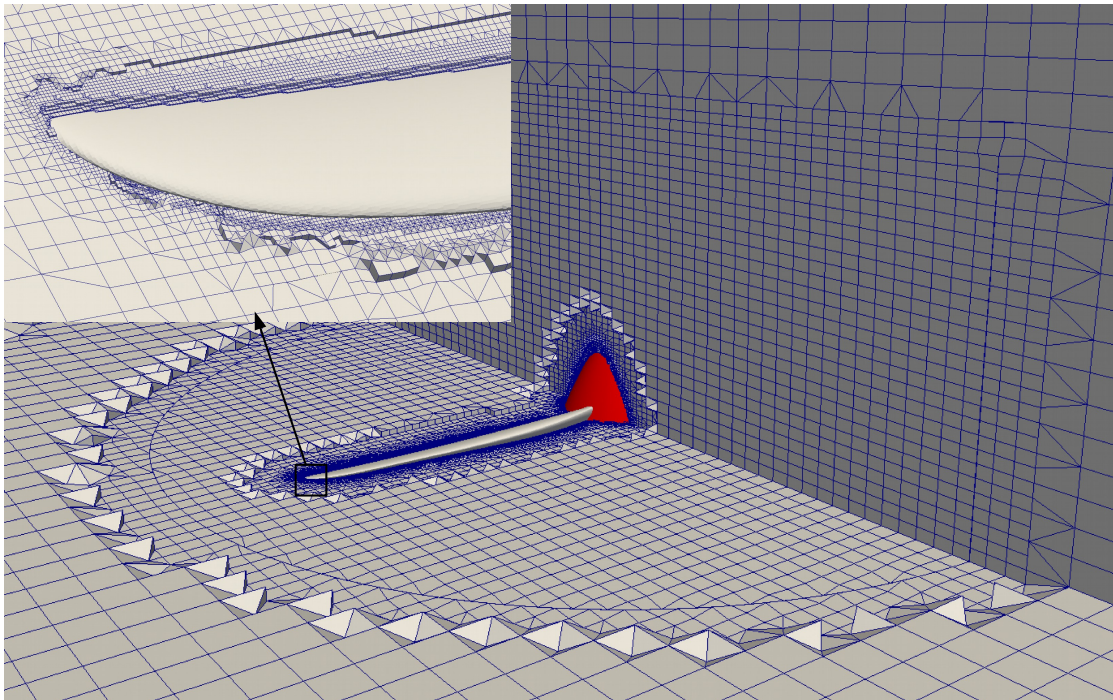

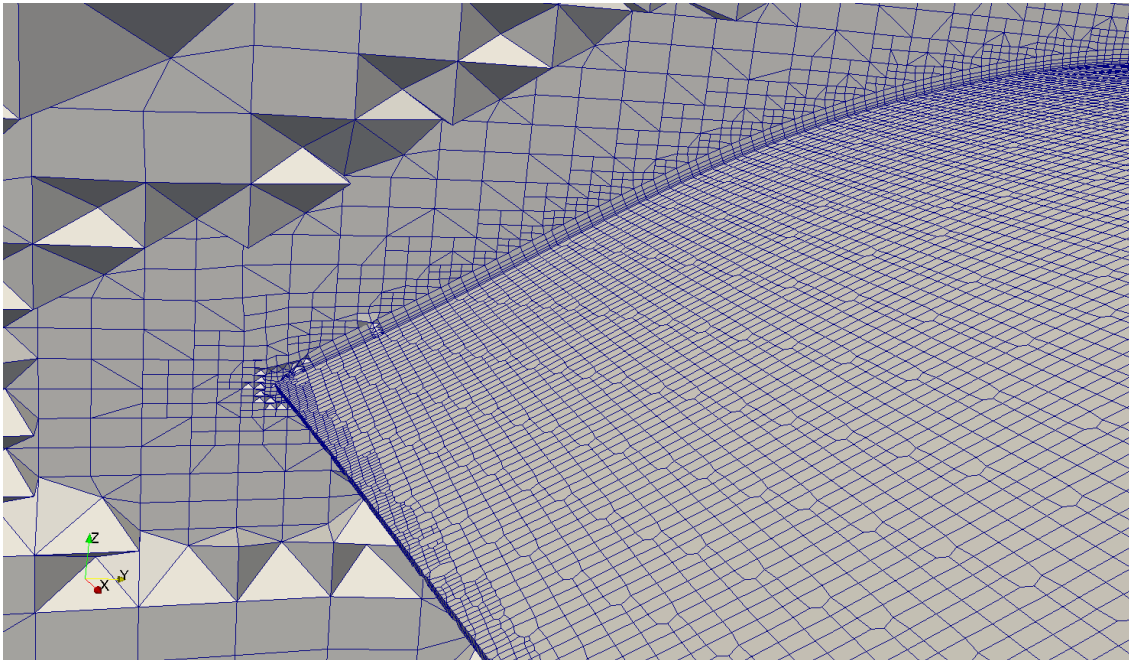Figure 4.4: Propeller tip inside mesh.

Figure 4.5: Trailing edge of propeller.
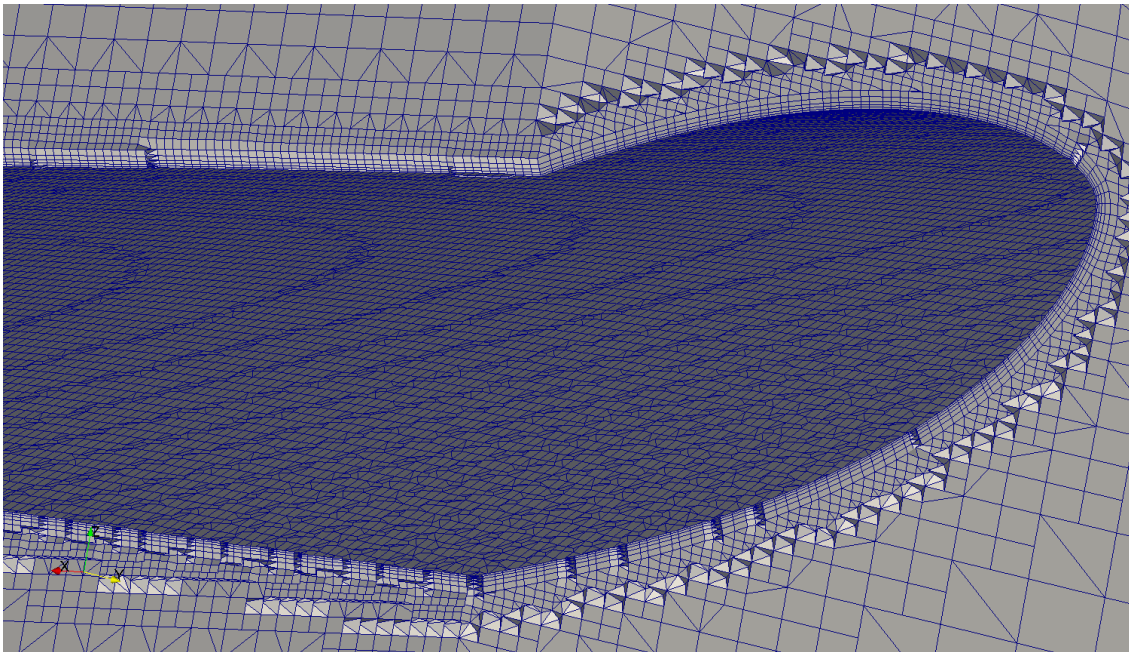
Figure 4.6: Leading edge and boundary layer.
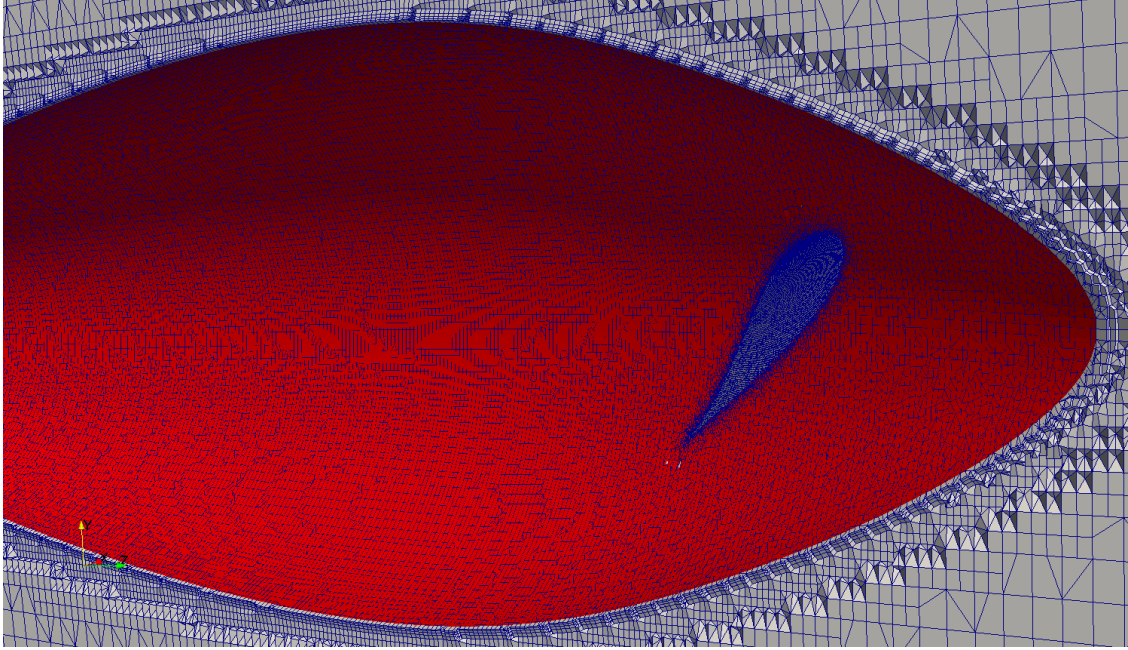
Figure 4.7: Boundary layer of spinner.

Settings

As experimental results are known for only one operating point, case will be set up for that operating point. The operating point is defined for the free stream velocity of 42.3 m/s and angular velocity of 216.66 rad/s. Thermodynamical parameters for experimental conditions are shown in Table (4.3) which are given for air conditions at approximately ≈ 2000 m sea level. Boundary conditions of turbulence parameters are

Table 4.3: Air conditions

ν	$1.5 \cdot 10^{-5}$	$\frac{\text{m}^2}{\text{s}}$
c_p	1005	$\left[\frac{\text{kJ}}{\text{kgK}}\right]$
M	28.966	$\left[\frac{\text{g}}{\text{mol}}\right]$
Pr	0.713	[-]
ρ	1.205	$\left[\frac{\text{kg}}{\text{m}^3}\right]$

calculated using empirical equations for turbulent length scale and turbulent intensity.

The turbulent kinetic energy is calculated:

$$k = \frac{3}{2}(IV_\infty)^2 \,, \tag{4.1}$$

where turbulence intensity is assumed 1% and the turbulent length scale is calculated:

$$l = 0.07D_f \,, \tag{4.2}$$

where D_f is the characteristic length, in this case diameter of the propeller. For all numerical simulations k-ω *SST* will be used, turbulent length scale ω is calculated according expression:

$$\omega = \frac{k^{0.5}}{C_\mu^{0.25}l} \,, \tag{4.3}$$

where C_μ is a constant defined in turbulence model.

4.2. Setup of Engine Cooling System

The aim of the engine cooling system case is to prescribe heat transfer rate from the engine cylinders to the air flow. The second important task of this case is calculation of mass flow through engine cylinders (porous zone). The complex geometry of engine cylinders ribs is difficult to model. A reasonable simplification comes in form of the porous zone. Mesh domain is a cuboid where fuselage with its cooling system is positioned in the center of the cuboid. Figure (4.8) shows symmetrically clipped domain, and representation of fuselage. Fuselage is modeled with focus on internal heat transfer, where the influence of the plane's real shape is negligible. Mean focus in modeling was the front side of the aircraft, and nose modeling with diffuser intake. Special attention has been given to the internal system of cooling engine. Inlet diffuser is colored blue, and outtake from the system cooling is colored yellow, as seen in Figure (4.8).
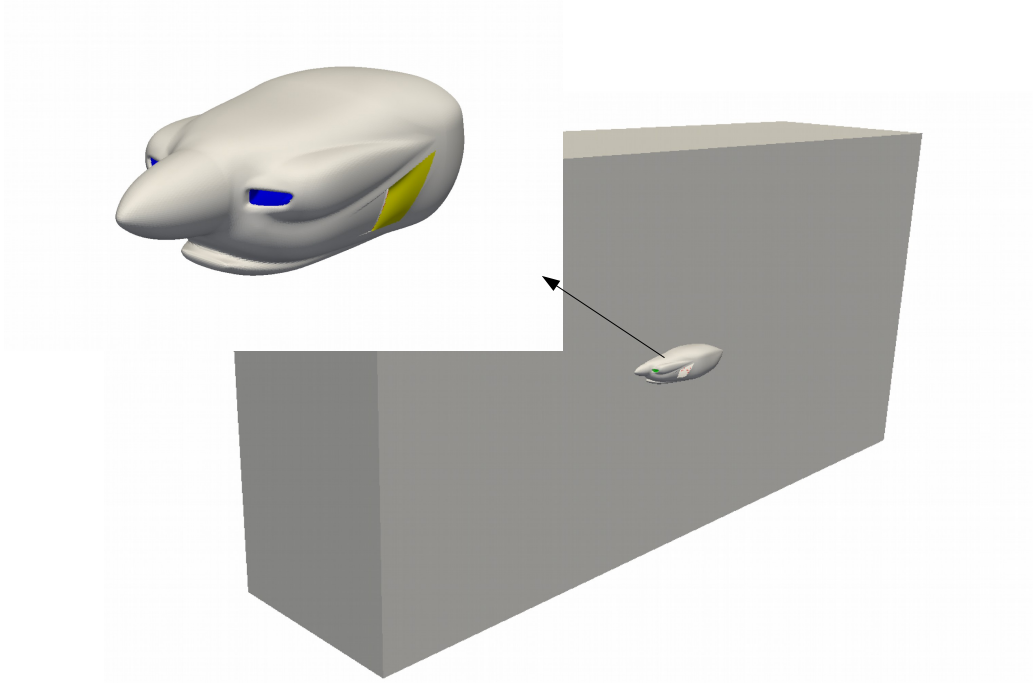
Figure 4.8: Cooling system domain.

Entering at internal parts of the cooling system, air has to pass through diffuser (colored blue), and pass through internal box where piston engine with six cylinders is positioned (colored brown), Figure (4.9). Six cylinders are represented by porous zone, where internal cells are defined as cell zone, and boundary of the zone is defined as face zone. These selected cells will behave like a porosity in order to model cooling ribs along the engine. The reality of physical flow is defined with experimental pressure drop through porous zone.   Table (4.4) shows boundary names and types of boundaries for mesh domain. Inlet and outlet are located relatively far from the fuselage to get free stream conditions as represented in Figure (4.8).
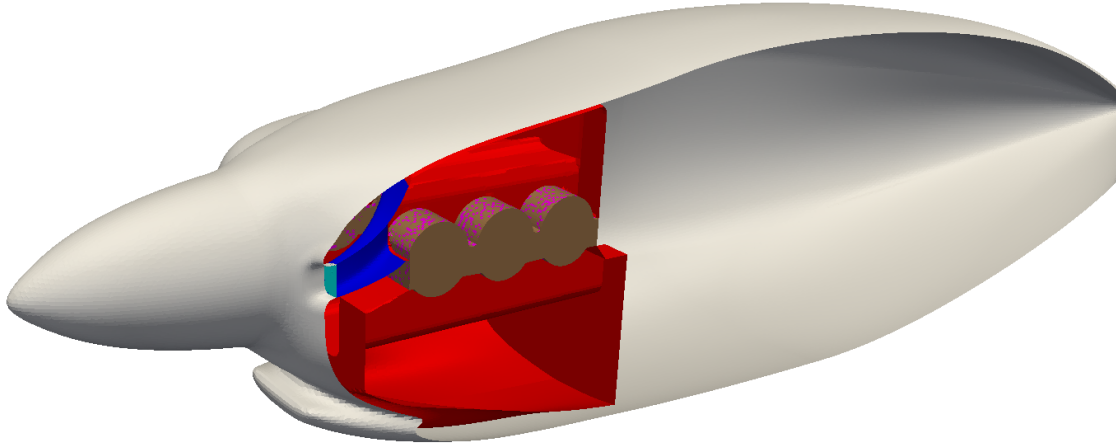
Figure 4.9: Internal parts of cooling system.

Table 4.4: Boundary names and types for cooling system.

Number	Name	Type of boundary
1.	inlet	patch
2.	outlet	patch
3.	fuselage	wall
4.	internal	wall
5.	porositywall	wall
6.	difuser	wall
7.	outtake	wall

Settings

First, to set up a case user needs to define a set of values. To include porous zone Darcy-Forheimmer coefficients or Power Law coefficients need to be defined inside the momentum equation. Darcy-Forheimmer model is used for all simulations including porous media. Experimental set of data with pressure drop and velocity through porous
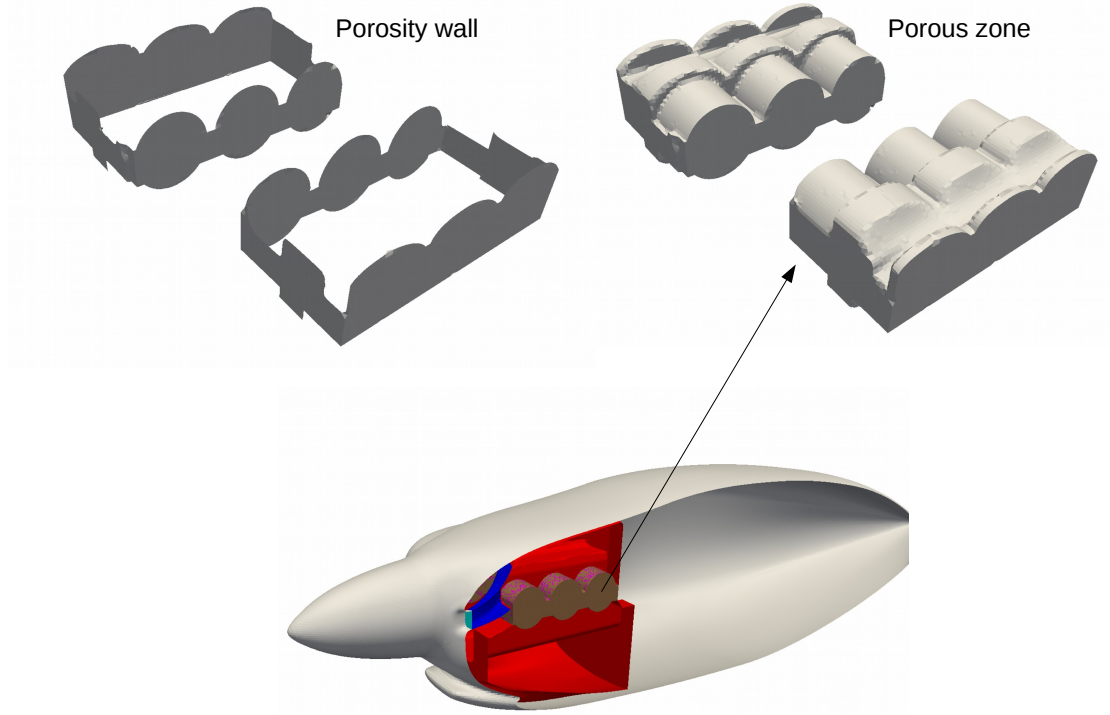
Figure 4.10: Engine introducing porous zone with porous wall.

media needs to be included. This porous zone is in a shape of piston engine presented in Figure (4.10) and porosity wall is located in space around the engine. It is shown in Figure (4.11) where blue points are representing experimental data through which fitted curve is driven:

$$f(u) = 367.27u^2 + 233.85u \,. \tag{4.4}$$

This fitted function has to be second order square function of velocity which describes pressure drop. Darcy-Forheimmer coefficients are calculated as:

$$
\begin{aligned}
D &= \frac{\alpha}{\nu} = 13.59530 \cdot 10^6 \\
E &= \frac{2\beta}{\rho} = 727.27 \,,
\end{aligned}
\tag{4.5}
$$

where α and β are coefficients next to variable u in equation (4.4). These coefficients are added into the momentum equation where the additional term in porous zone is
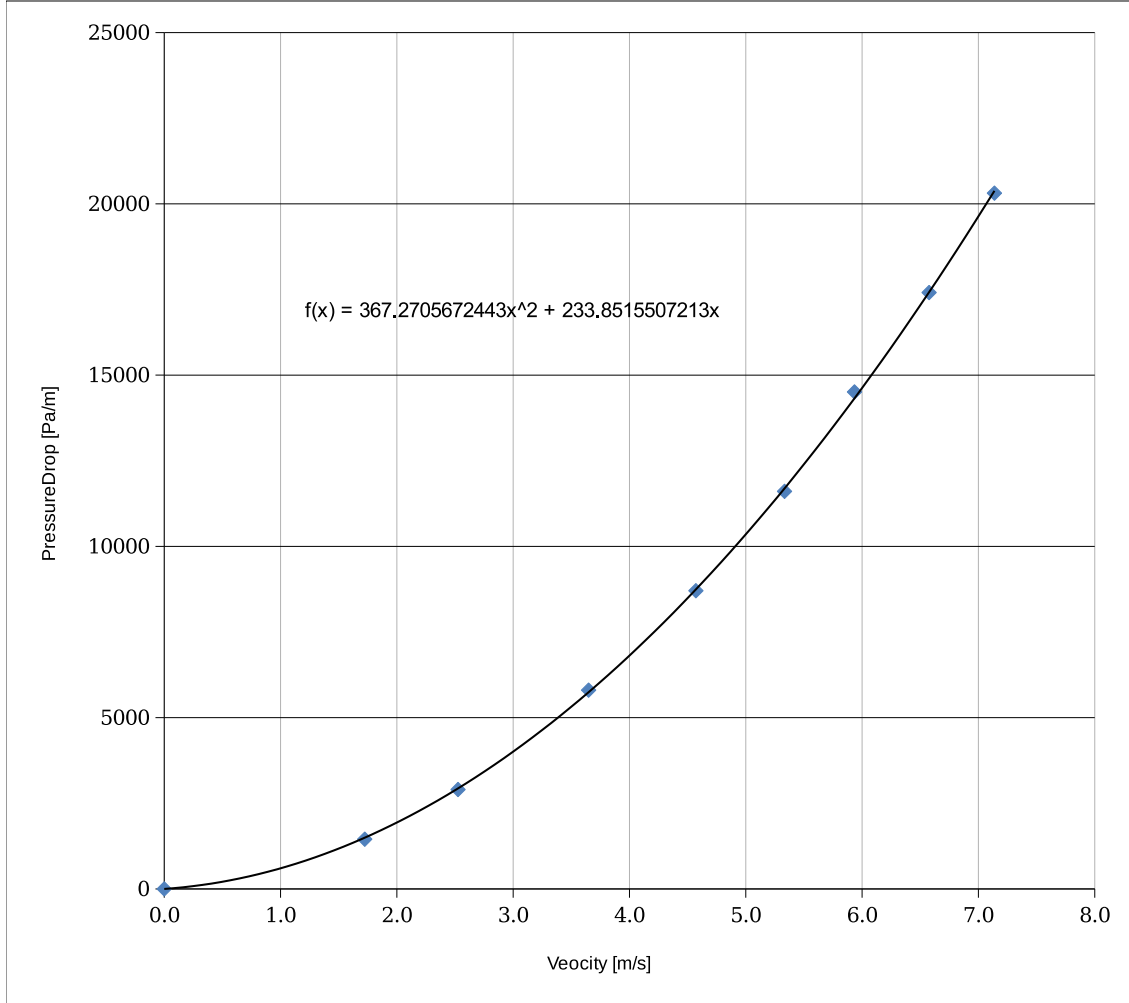
Figure 4.11: Pressure drop trough the porous zone.

behaving as a sink of velocity with proportional strength of D and F coefficients.

The second step is the definition of heat transfer for all heat transfer models, described in section (3.6.), where heat transfer rate needs to be calculated. Parameters of the engine and its cooling ribs and also air characteristics are shown in Table (4.5). First, we need to calculate heat convection coefficient for one rib inside cooling system, and then for all engine ribs using relations [10]. The mean temperature value in convection process is

$$T_{mean} = \frac{T_s + T_f}{2} = 345.57 \, \text{K} \,, \tag{4.6}$$

and all air characteristic will be taken for that temperature. Reynolds number is defined

Table 4.5: Conditions for porous medium.

ν	$1.72 \cdot 10^{-5}$	$\frac{\text{m}^2}{\text{s}}$
p_f	79485	Pa
T_f	288	K
T_s	403.15	K
α	-1.5	$^\circ$
ρ	1.01	$\frac{\text{kg}}{\text{m}^3}$
S_{ref}	3.5	m^2

Table 4.6: Characteristics of air at 345.57 K.

ν	$2 \cdot 10^{-5}$	$\frac{\text{m}^2}{\text{s}}$
C_p	1009	$\frac{\text{W}}{\text{kgK}}$
ρ	1.003	$\frac{\text{kg}}{\text{m}^3}$
λ	0.0294	$\frac{\text{W}}{\text{mK}}$

as:

$$Re = \frac{w_\infty t}{\nu} = 625 \, [-] . \tag{4.7}$$

where t is the characteristic length (the width of fins) and the mean velocity w_∞ is $2.5 \, \text{m/s}$. Calculated Prandtl number is:

$$Pr = \frac{c_p \rho \nu}{\lambda} = \frac{1009 \cdot 1.0032 \cdot 10^{-5}}{0.0294} = 0.7085 \, [-] . \tag{4.8}$$

The Nusselt number can be calculated using relation (3.48), by assuming turbulent fluid flow. Having in mind that local paths create turbulent fluid flow, these calculations are valid only on the local level:

$$N_u = 0.023 \cdot 625^{0.8} \cdot 0.7085^{0.33} = 0.63 \, [-] . \tag{4.9}$$

From this point local heat convection coefficient is:

$$\alpha_{fin} = \frac{N_u \lambda}{t} = \frac{58.057 \cdot 0.0294}{0.165} = 0.64 \, \frac{\text{W}}{\text{m}^2\text{K}} , \tag{4.10}$$

and it takes into account shape and dimensions of all engine ribs with equations defined in [10]. Dimensions of engine cooling ribs are shown in Table (4.7). The definition of

Table 4.7: Dimensions of engine cooling ribs.

w	Width of fin	0.165 m
p	Fin pitch	0.0055 m
s	Average air space between fins	0.005 m
t	Average fin thickness	0.0005 m
w'	Width of fin plus 0.5 tip thickness	0.1655 m
s_b	Length of cylinder wall exposed between two adjacent fins	0.0035 m
R_b	Radius to base of fins	0.14 m
k	Thermal conductivity of fin material	$16 \, \frac{\text{W}}{\text{m}^2\text{K}}$

total α is:

$$\alpha = \frac{\alpha_{fin}}{s+t} \left[\frac{2}{a} \left(1 + \frac{w}{2R_b} \right) \tanh(aw') + s_b \right] , \tag{4.11}$$

with the addition of:

$$a = \sqrt{\frac{2\alpha_{fin}}{kw}} = 3.783 , \tag{4.12}$$

and after inserting required values the final result is:

$$\alpha = 53.72 \, \frac{\text{W}}{\text{m}^2\text{K}} . \tag{4.13}$$

Heat exchange between the engine and the surrounding cooling air inside porous zone is defined as:

$$Q_{tot} = \alpha S_{ref}(T_s - T_f) = 21650.52 \, \text{W} . \tag{4.14}$$

5 | Results

The results for case introduced in Chapter (4.) are presented in the sequel. The first section is observing compressible effects, wake pattern, blade pressure distribution and influence of different freestream velocity on forces and moments on the propeller. The second section demonstrates the heat transfer inside the engine compartment. Main focus is on wall temperature limits, cooling efficiency and influence of the propeller wake on internal flow.

5.1. Propeller Simulation Results

Results are presented for three different solvers: steady compressible, incompressible transient and steady solver. Transient numerical simulation should be more accurate, but steady simulation is sufficiently accurate. As calculated forces and moments varied less than 1% between simulations. Compressibility is taken into account, because Mach number at the tip of the propeller is significantly higher than 0.3, shown in the Figure (5.8). This causes density and pressure field changes which affect the force and moment results in Table (5.7). Mesh of the rotor cell zone is rotating with angular velocity $\omega = 216.66\,\text{rad/s}$, which is defined for cruise speed of aircraft.

At inlet patch called big_cylinder_inlet fixed velocity boundary condition is used, while pressure value is set at the outlet patch which consists of big_cylinder_liner and big_cylinder_outlet. Steady compressible MRF simulation demands following pressure and velocity boundary condition definition presented in Table (5.1). μ_t and α_t at inlet and outlet patch are set to 0, while at wall types are calculated. It can be shown in

Table (5.2). For all boundary conditions at small cylinder patch types are set to general grid interface, while **cyclic_left** and **cyclic_right** are set to cyclic general grid interface patch type. Temperature has fixed value at the inlet patch and zero gradient patch type at propeller, spinner and outlet patches. Boundary condition for turbulence dissipation length ω has fixed value at the inlet, and zero gradient at outlet. At walls omega wall function is defined. It is shown in the figure (5.4). Final, turbulence kinetic energy **k** is set as fixed value for the inlet, and zero gradient for outlet. At walls compressible kqr wall function is defined. It is shown in the Table (5.5).

Table 5.1: Boundary conditions for pressure and velocity.

Boundary name	Velocity	Pressure
big_cylinder_inlet	type fixedValue; value uniform(0 0 42.3);	type isentropicTotalPressure; p0 uniform 100522;
big_cylinder_liner	type fixedValue; uniform(0 0 0);	type fixedValue; value uniform 100000;
big_cylinder_outlet	type fixedValue; uniform(0 0 0);	type fixedValue; value uniform 100000;
propeller	type fixedValue; value uniform(0 0 0);	type zeroGradient;
spinner	type fixedValue; value uniform(0 0 0);	type zeroGradient;
small_cylinder_inletIS	type ggi;	type ggi;
small_cylinder_linerIS	type ggi;	type ggi;
small_cylinder_outletIS	type ggi;	type ggi;
small_cylinder_inletUS	type ggi;	type ggi;
small_cylinder_linerUS	type ggi;	type ggi;
small_cylinder_outletUS	type ggi;	type ggi;
cyclic_leftV	type cyclicGgi;	type cyclicGgi;
cyclic_rightV	type cyclicGgi;	type cyclicGgi;
cyclic_leftM	type cyclicGgi;	type cyclicGgi;
cyclic_rightM	type cyclicGgi;	type cyclicGgi;

Table 5.2: Boundary conditions for ν_t and μ_t.

Boundary name	ν_t	μ_t
big_cylinder_inlet	type calculated; value uniform 0;	type calculated; value uniform 0;
big_cylinder_liner	type calculated; value uniform 0;	type calculated; value uniform 0;
big_cylinder_outlet	type calculated; value uniform 0;	type calculated; value uniform 0;
propeller	type nutWallFunction; value uniform 0;	type mutWallFunction; value uniform 0;
spinner	type nutWallFunction; value uniform 0;	type mutWallFunction; value uniform 0;
small_cylinder_inletIS	type ggi;	type ggi;
small_cylinder_linerIS	type ggi;	type ggi;
small_cylinder_outletIS	type ggi;	type ggi;
small_cylinder_inletUS	type ggi;	type ggi;
small_cylinder_linerUS	type ggi;	type ggi;
small_cylinder_outletUS	type ggi;	type ggi;
cyclic_leftV	type cyclicGgi;	type cyclicGgi;
cyclic_rightV	type cyclicGgi;	type cyclicGgi;
cyclic_leftM	type cyclicGgi;	type cyclicGgi;
cyclic_rightM	type cyclicGgi;	type cyclicGgi;

Table 5.3: Boundary conditions for α_t and rhothalpy.

Boundary name	α_t	i
big_cylinder_inlet	type calculated; value uniform 0;	type fixedValue; value uniform 0;
big_cylinder_liner	type calculated; value uniform 0;	type gradientEnthalpy; gradient 0;
big_cylinder_outlet	type calculated; value uniform 0;	type gradientEnthalpy; gradient 0;
propeller	type alphatWallFunction; Prt 0.71 value uniform 0;	type gradientEnthalpy; gradient 278188;
spinner	type alphatWallFunction; Prt 0.71 value uniform 0;	type gradientEnthalpy; gradient 278188;
small_cylinder_inletIS	type ggi;	type ggiEnthalpyJump; patchType ggi; rotating true;
small_cylinder_linerIS	type ggi;	type ggiEnthalpyJump; patchType ggi; rotating true;
small_cylinder_outletIS	type ggi;	type ggiEnthalpyJump; patchType ggi; rotating true;
small_cylinder_inletUS	type ggi;	type ggiEnthalpyJump; patchType ggi; rotating false;
small_cylinder_linerUS	type ggi;	type ggiEnthalpyJump; patchType ggi; rotating false;
small_cylinder_outletUS	type ggi;	type ggiEnthalpyJump; patchType ggi; rotating false;
cyclic_leftV	type cyclicGgi;	cyclicGgi;
cyclic_rightV	type cyclicGgi;	cyclicGgi;
cyclic_leftM	type cyclicGgi;	cyclicGgi;
cyclic_rightM	type cyclicGgi;	cyclicGgi;

Table 5.4: Boundary conditions for ω and temperature.

Boundary name	ω	Temperature
big_cylinder_inlet	type fixedValue; value uniform 4000;	type isentropicTotalPressure; T0 uniform 300.447; value uniform 0;
big_cylinder_liner	type zeroGradient;	type zeroGradient;
big_cylinder_outlet	type zeroGradient;	type zeroGradient;
propeller	compressible::omegaWallFunction; refValue uniform 0;	type zeroGradient;
spinner	compressible::omegaWallFunction; refValue uniform 0;	type zeroGradient;
small_cylinder_inletIS	type ggi; patchType ggi;	type ggiEnthalpyJump; patchType ggi; rotating true;
small_cylinder_linerIS	type ggi; patchType ggi;	type ggiEnthalpyJump; patchType ggi; rotating true;
small_cylinder_outletIS	type ggi; patchType ggi;	type ggiEnthalpyJump; patchType ggi; rotating true;
small_cylinder_inletUS	type ggi; patchType ggi;	type ggiEnthalpyJump; patchType ggi; rotating false;
small_cylinder_linerUS	type ggi; patchType ggi;	type ggiEnthalpyJump; patchType ggi; rotating false;
small_cylinder_outletUS	type ggi; patchType ggi;	type ggiEnthalpyJump; patchType ggi; rotating false;
cyclic_leftV	type cyclicGgi;	cyclicGgi;
cyclic_rightV	type cyclicGgi;	cyclicGgi;
cyclic_leftM	type cyclicGgi;	cyclicGgi;
cyclic_rightM	type cyclicGgi;	cyclicGgi;

Table 5.5: Boundary conditions for pressure and velocity.

Boundary name	k
big_cylinder_inlet	type fixedValue; value uniform 0.071;
big_cylinder_liner	type zeroGradient;
big_cylinder_outlet	type zeroGradient;
propeller	type compressible::kqRWallFunction;
spinner	type compressible::kqRWallFunction;
small_cylinder_inletIS	type ggi;
small_cylinder_linerIS	type ggi;
small_cylinder_outletIS	type ggi;
small_cylinder_inletUS	type ggi;
small_cylinder_linerUS	type ggi;
small_cylinder_outletUS	type ggi;
cyclic_leftV	type cyclicGgi;
cyclic_rightV	type cyclicGgi;
cyclic_leftM	type cyclicGgi;
cyclic_rightM	type cyclicGgi;

The last variable which needs to be defined is rhotalpy. In turbomachinery rothalpy is constant along streamlines, and calculated as [18]:

$$I = h_0 + \omega R V_\theta \, , \tag{5.1}$$

where h_0 is total enthalpy, ω is angular velocity, R radius and V_θ is relative velocity. Pressure and velocity field are shown in sliced plane vertical and parallel to axial axis of the propeller in Figures form (5.1) to (5.4).
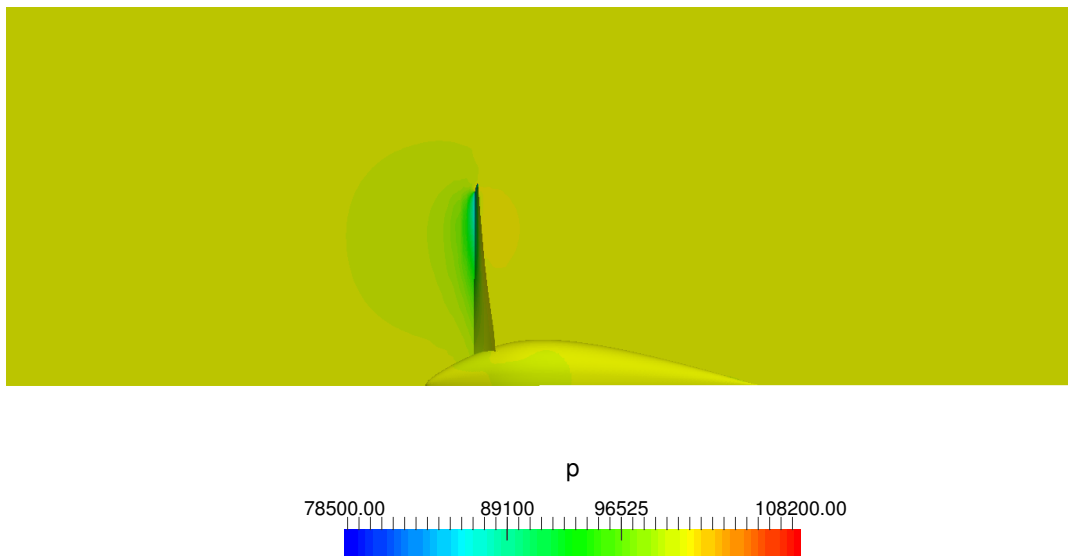
Figure 5.1: Pressure distribution for sliced plane x-z.
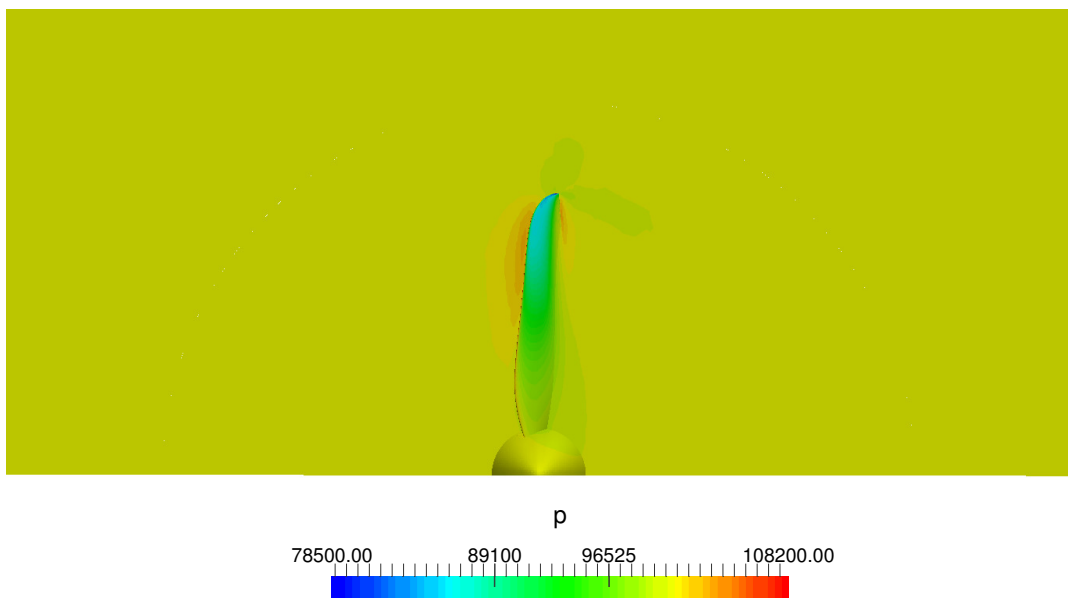
Figure 5.2: Pressure distribution for sliced plane x-y.

For case set up of case explained in (4.1.) pressure field is presented in Figures (5.1) and (5.2).It can be seen that, approaching to the suction side of the blade, pressure is decreasing while on the other side, pressure side, pressure is increasing. This creates a force in axial direction. Difference in pressure also creates a vortex at the blade tip, which stretches in helical shape downstream of the propeller on the Figure (5.7). The main part of the force is produced in the area towards the tip, where the pressure is the lowest. In Figure (5.3) closed topological lines are created to visualize a creation of stretching vortex behind propeller.
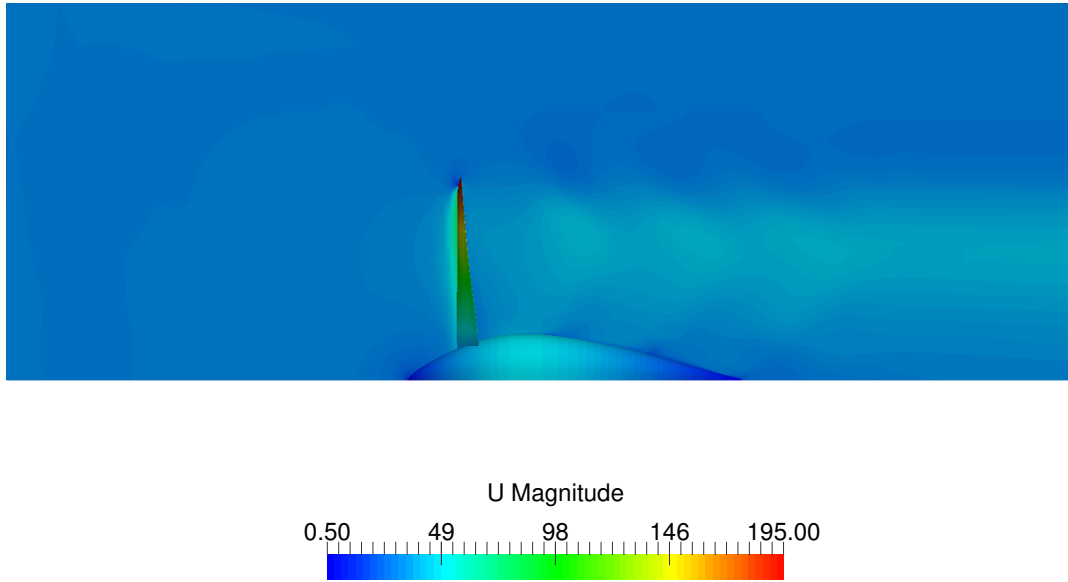
Figure 5.3: Velocity distribution for plane x-z.

In Figures (5.3) and (5.4) the velocity is increasing as the radius increases. The propeller with its spinner already has an influence on fluid in the front area where velocity is increasing when as approaching the surface. Downstream, propeller creates a vortex, which can be spotted by distribution of velocity field.
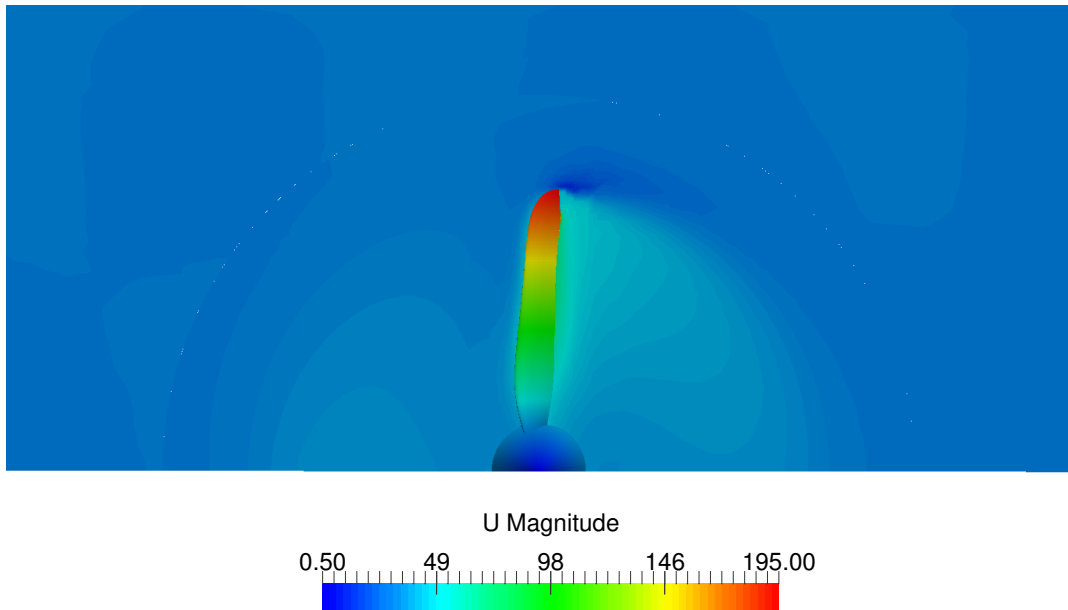
Figure 5.4: Velocity distribution for plane x-y.

Since blade is designed for relatively large subsonic speeds its curvature is not sharp. Velocity distribution on the Figure (5.4) shows equal velocity at downstream from the blade. As approaching to the tip, velocity drops to approximately zero. In front of the blade, velocity is increasing as approaching to the blade.
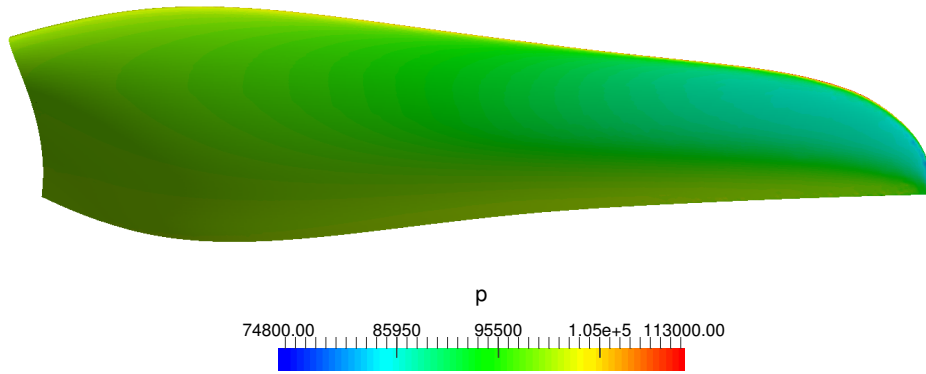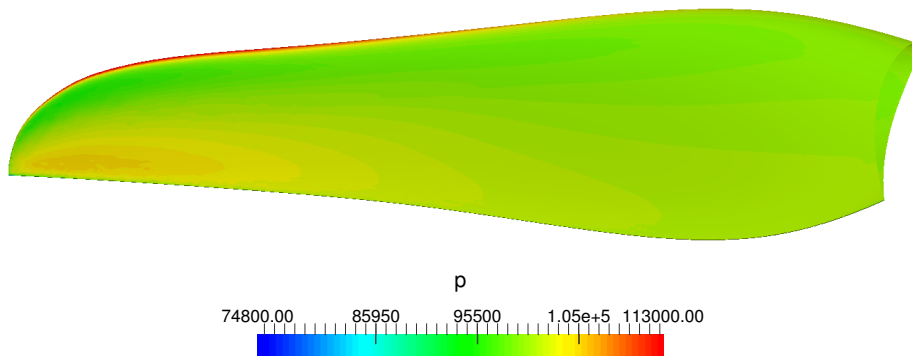
Figure 5.5: Suction side.

Figure 5.6: Pressure side.

In the Figure (5.5) highest pressure is distributed at leading edge. As approaching to trailing edge at suction side, pressure is dropping rapidly to its minimum value closer to the tip. On the other hand, at pressure side, in the Figure (5.6) pressure is dropping
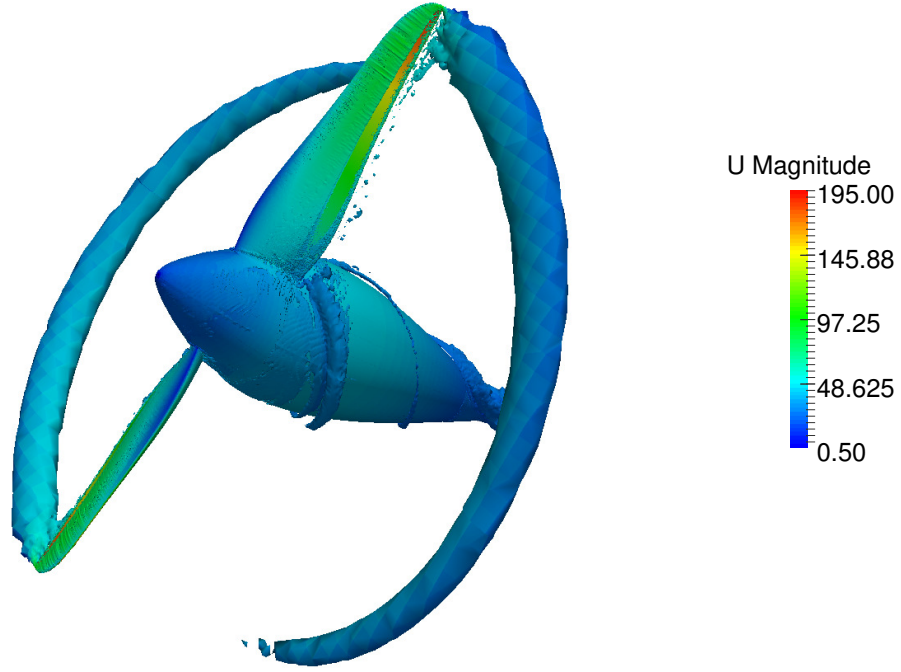
Figure 5.7: Main vortex at tip of propeller.

slower, as approaching to trailing edge, and gets mean value of pressure distribution on blade. For given conditions in this section results for thrust, moment, and power consumption by propeller are presented in the Table (5.6). Vortex is created at the

Table 5.6: Characteristic of propeller for $U_{inf} = 42.3$m/s

Propeller characteristics	Values
Thrust [N]	315.773
Torque [Nm]	89.98
Axial power [W]	21685.51

blade root, but its energy is smaller compared to the main vortex generated at the tip. The creation of vortex is caused by pressure difference at the tip, while the geometry changes at the connection of blade and spinner also cause pressure drop.

5.1.1.   Compressible Effects and Comparison of Results

In order to visualize compressible effects compressible and incompressible cases are compared. Comparison of the results was made for free stream velocity of 30 m/s and angular velocity of 241 rad/s. Maximum velocity at the propeller tip is 218 m/s. Using properties of air specified in the Table (4.3), Mach number reaches 0.63 as shown in Figure (5.8). Compressibility effects are not negligible at $Ma > 0.3$, which effect the comparison between incompressible and compressible results shown below. Comparison has been made in the following order:

- Steady compressible MRF case

- Steady incompressible MRF case

- Transient incompressible case.
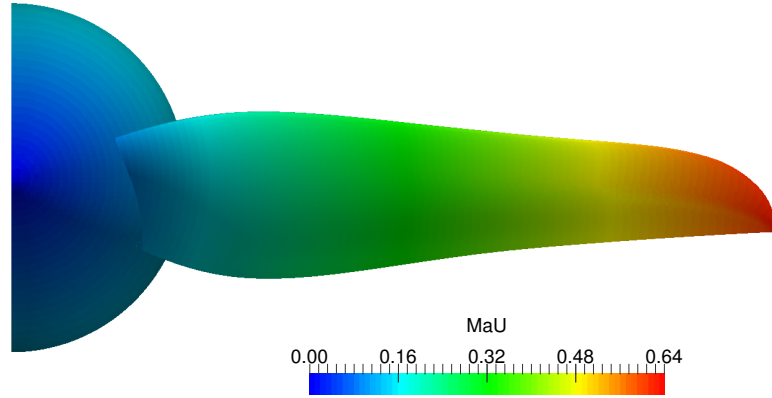
Figure 5.8: Mach number field.

Velocity fields of steady case are similar and they differ from transient results in the vortex tail area. Stronger effect of vortex can be seen in reduced velocity near the propeller tip in Figure (5.12), while incompressible cases in Figures (5.13) and (5.14) are generally the same. For presented velocity field along axis which are presented from Figure (5.9) to 5.11 are similar, and all confirm stretching vortex which can be spotted with distribution of velocity downstream.
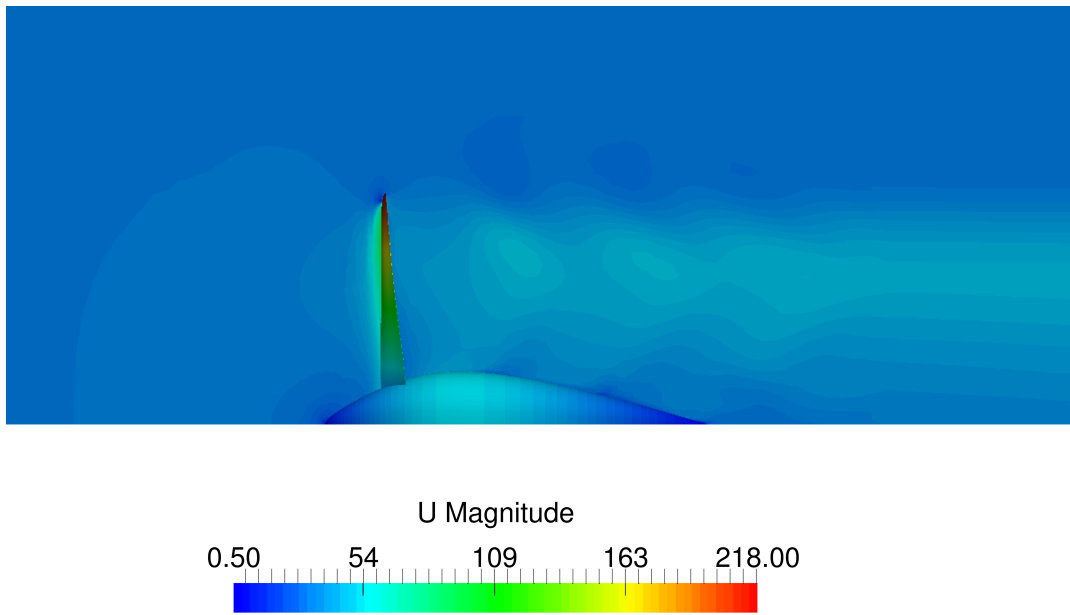
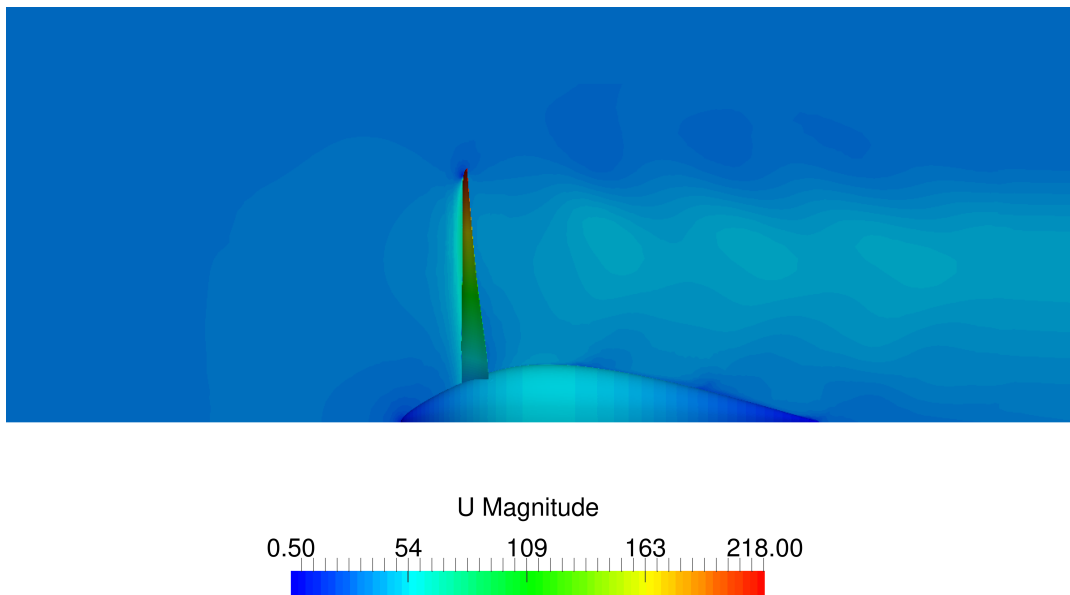Figure 5.9: Steady compressible velocity field along axis.

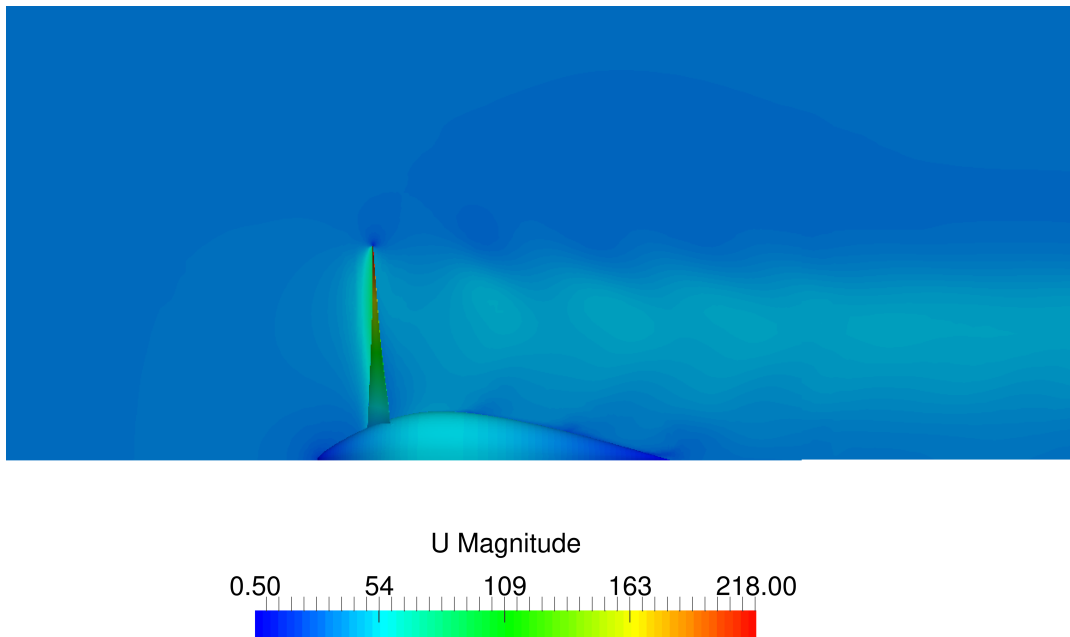Figure 5.10: Steady incompressible velocity field along axis.

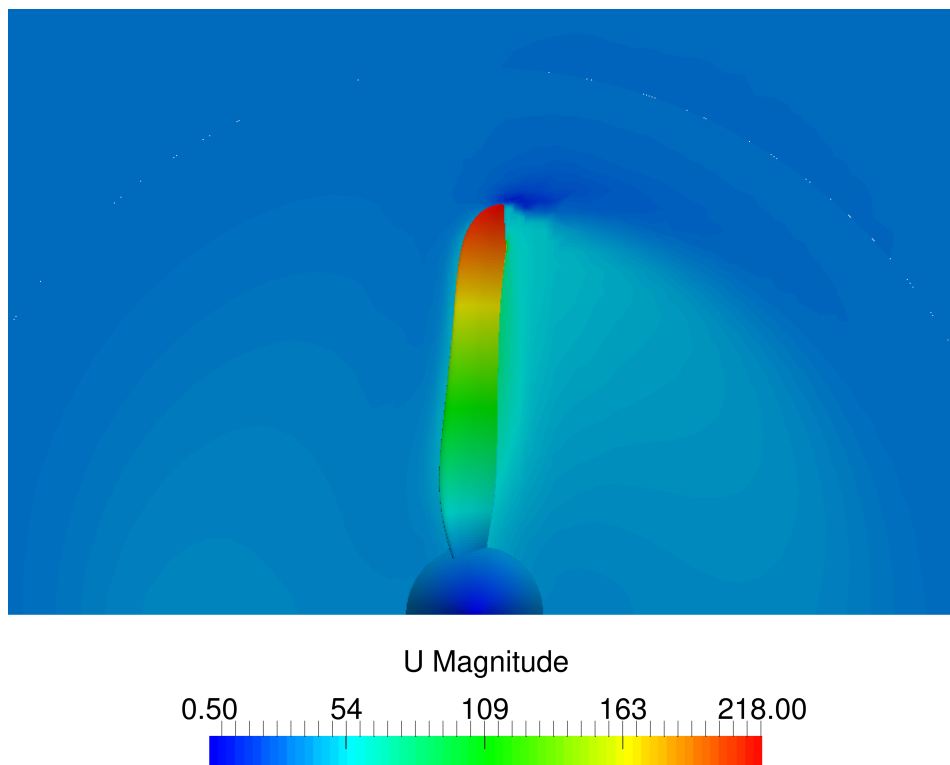Figure 5.11: Transient incompressible velocity field along axis.

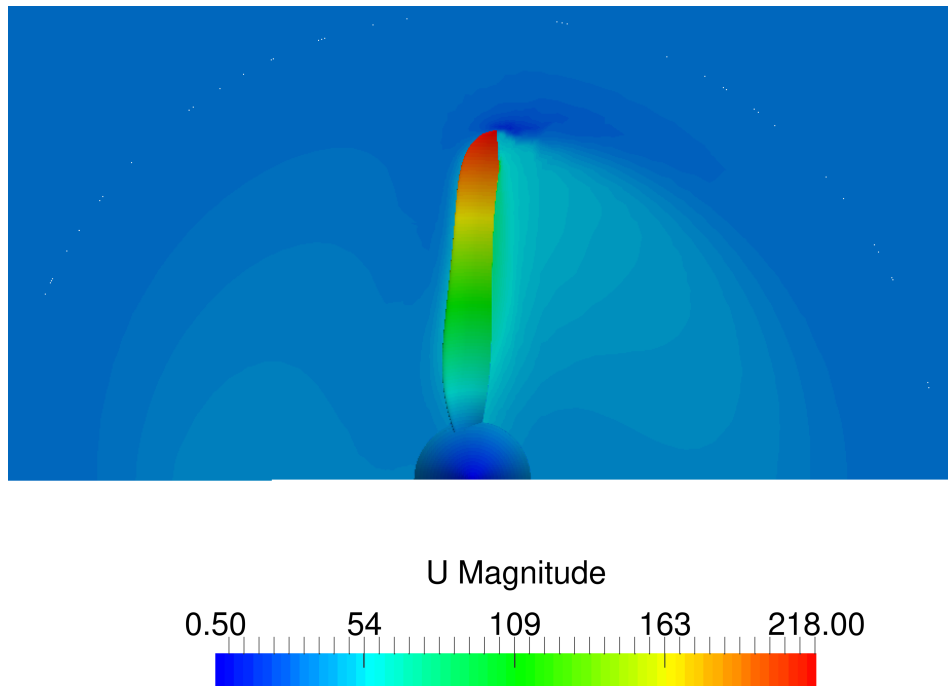Figure 5.12: Steady compressible velocity field across axis.

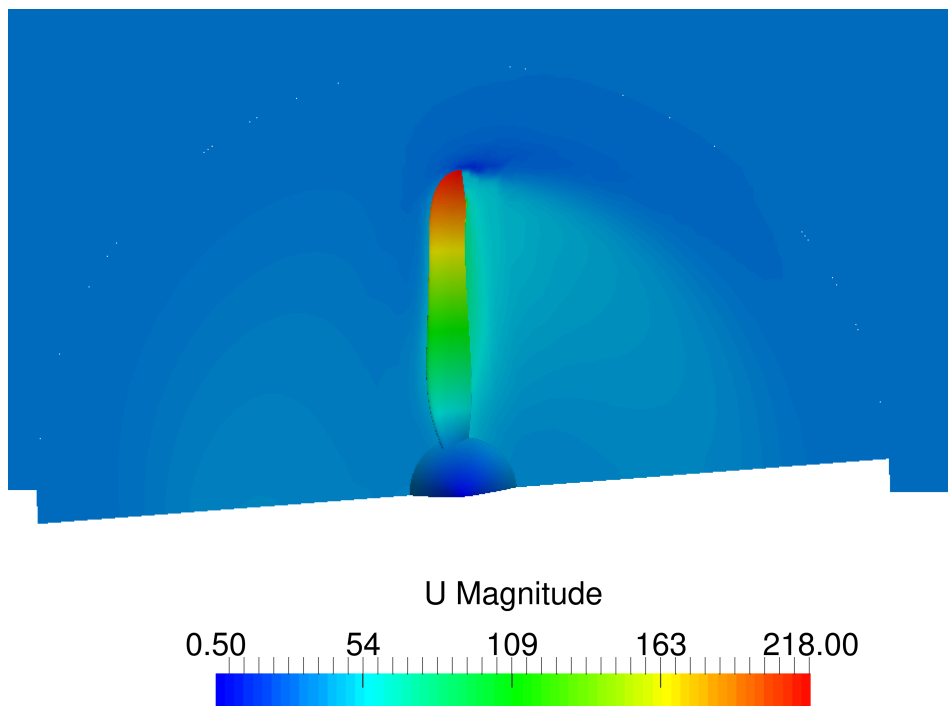Figure 5.13: Steady incompressible velocity field across axis.

Figure 5.14: Transient incompressible velocity field across axis.

Streams in the compressible case Figure (5.15) are different compared to the incompressible (Figs. 5.15 5.17 and 5.17), because velocities at the propeller tip which overcame 0.3 Ma are intensively reducing the pressure drop compared to incompressible cases.
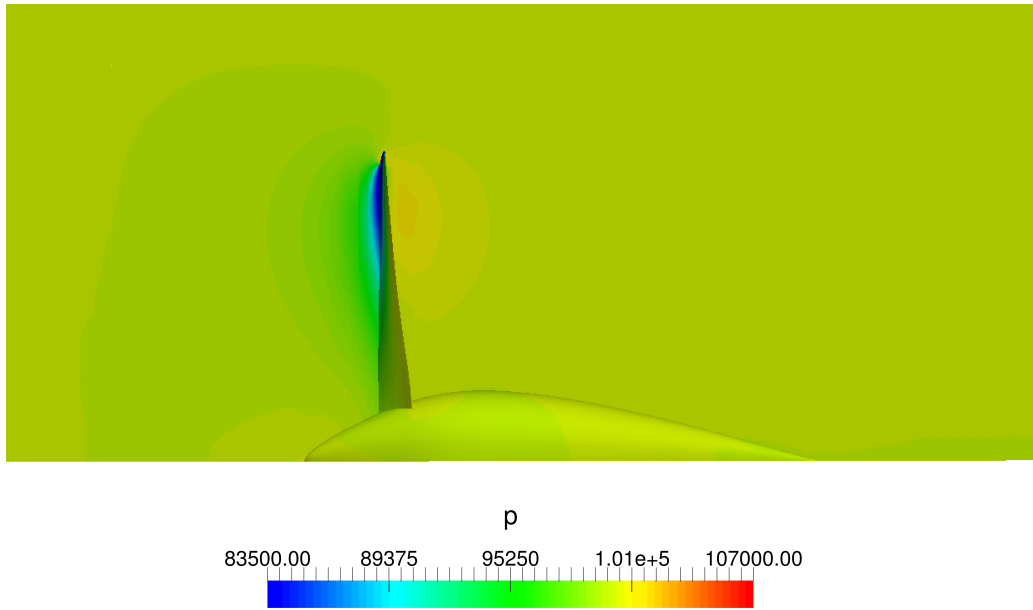

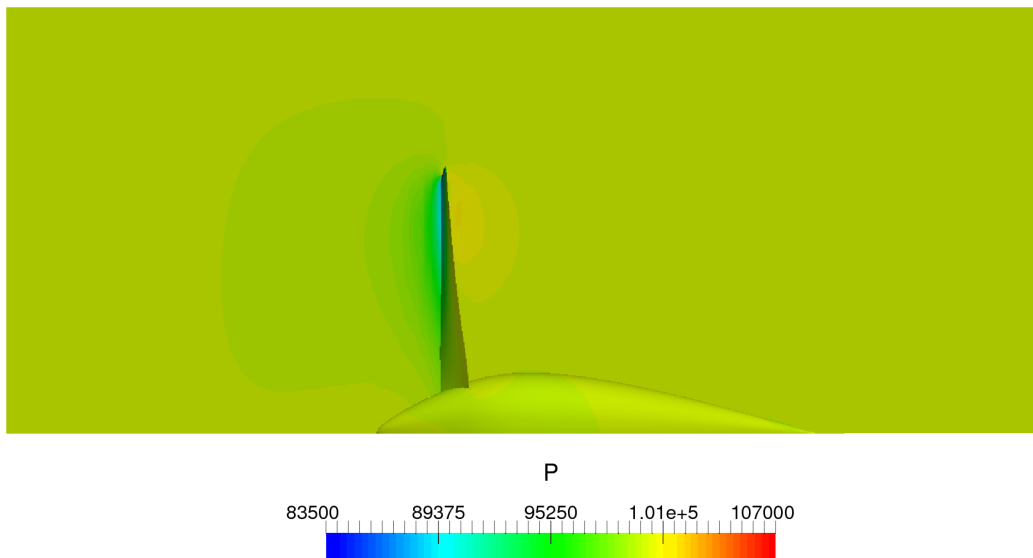Figure 5.15: Steady compressible pressure field along axis.

Figure 5.16: Steady incompressible pressure field along axis.

P

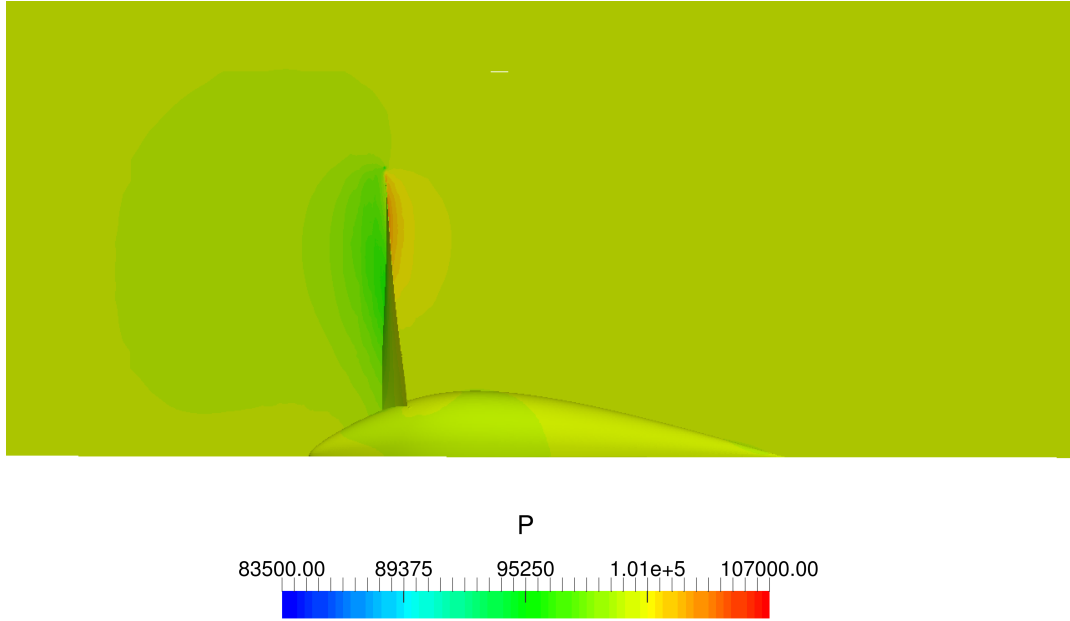83500.00   89375   95250   1.01e+5   107000.00

Figure 5.17: Transient incompressible pressure field along axis.

Suction area of the propeller is larger in incompressible cases as shown in the Figure (5.19). It effects the total pressure and moment comparison. On the other hand, incompressible cases have similar distributions of pressure. Four sliced propeller sections are shown in the Figure (5.18). Distribution of the pressure along the propeller blade can be seen. Also, it shows that field flow is changing its direction as the pressure is decreasing on the upper surface. On the other hand, at lower surface, pressure is increasing. In radius equals 0.85 large pressure gradients are present at tailing edge. At the pressure side approaching to the tip two large pressure drops occur, first on the leading edge and second on the trailing edge. It can explain the beginning of vortex at the tip.
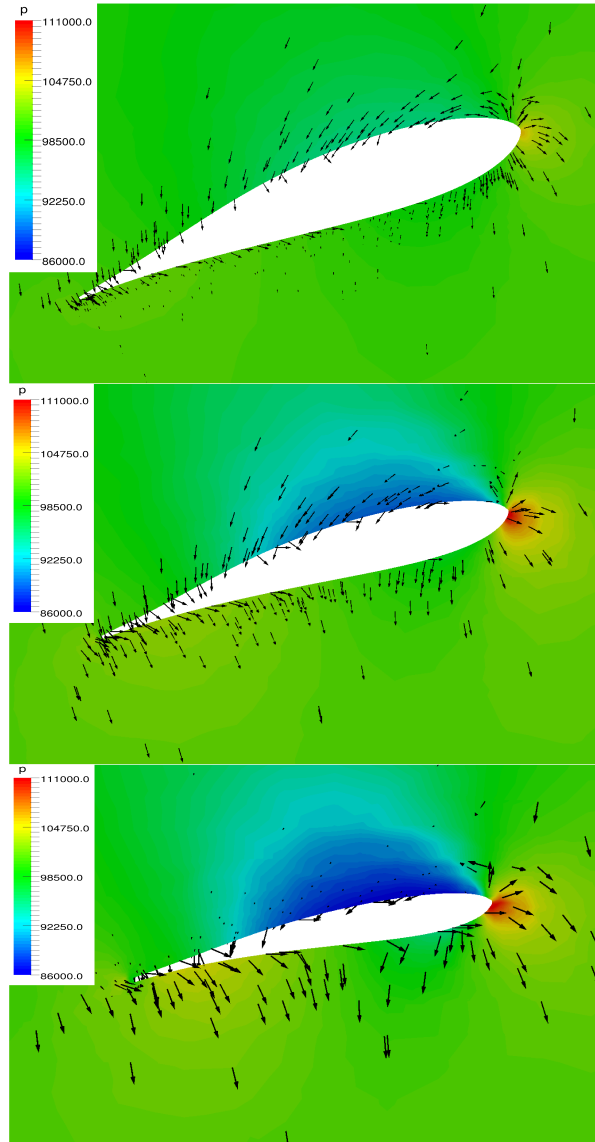
Figure 5.18: Pressure distribution and magnitude of velocity glyphs for radius sections 0.45, 0.65 and 0.85.

High pressure area of the blade has the same size in incompressible transient and steady one. Difference in the area where higher value of pressure is located close to the trailing edge. The main difference is that Figure (5.21) transient effects are taken into account. As these two Figures, (5.20) and (5.21), show little deviation between pressure and velocity distribution on the blade, it can be assumed that a current problem is a steady case problem.
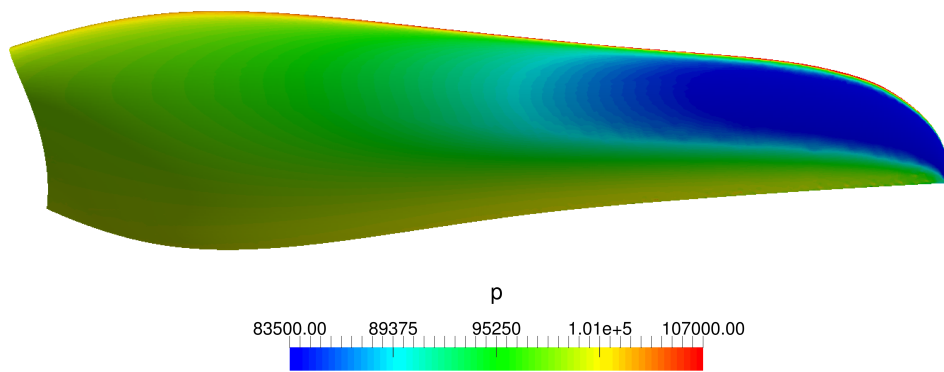
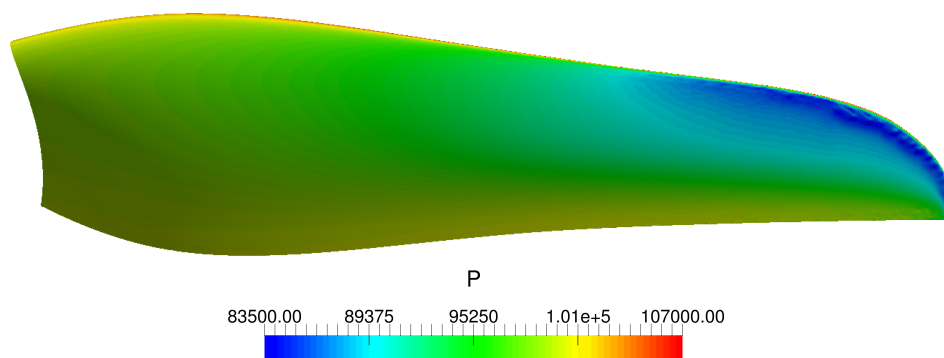Figure 5.19: Steady compressible pressure field on the propeller.

Figure 5.20: Steady incompressible pressure field on the propeller.
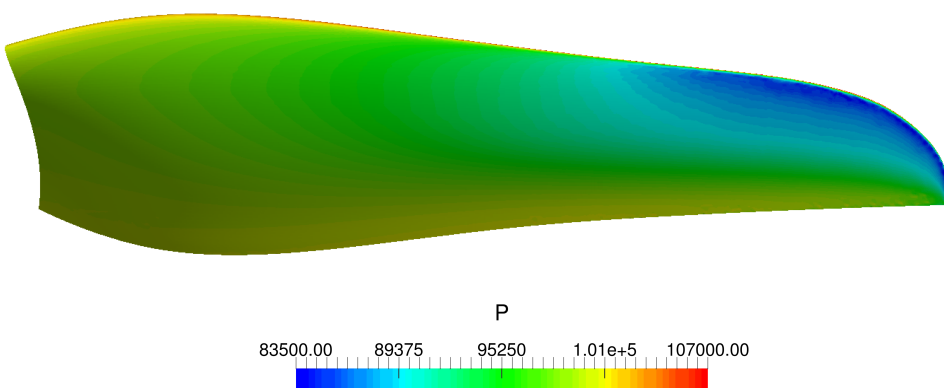

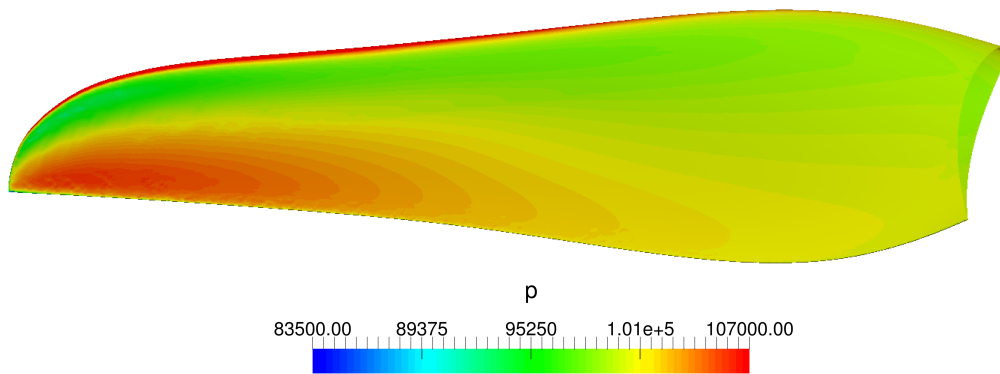Figure 5.21: Transient incompressible pressure field on the propeller.

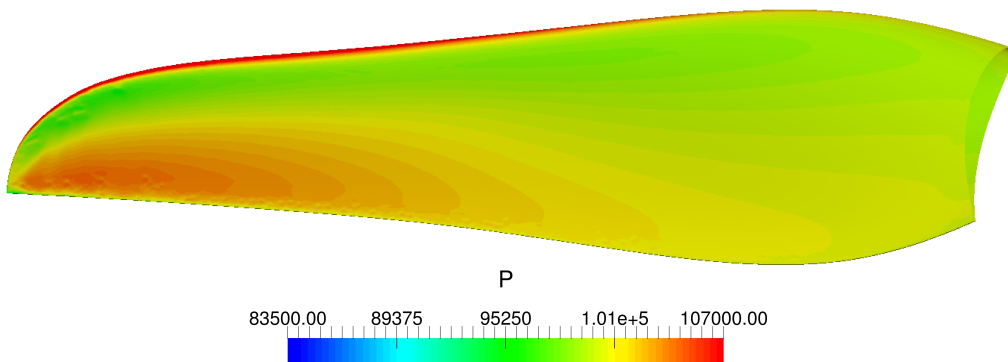Figure 5.22: Steady compressible pressure field on the propeller.

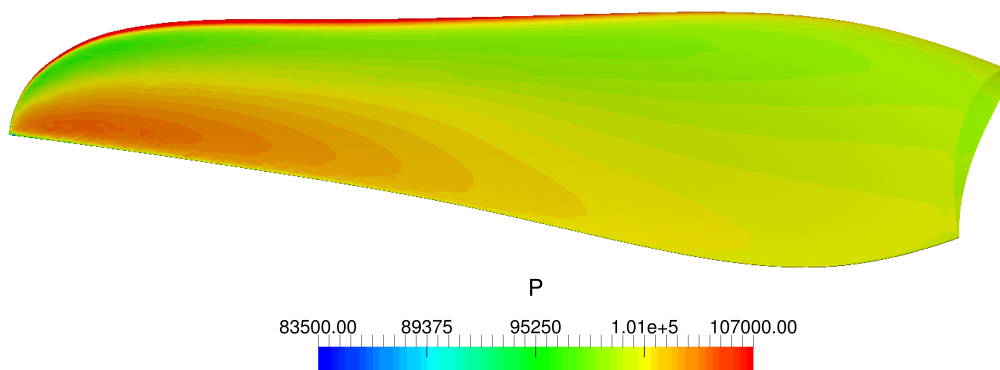Figure 5.23: Steady incompressible pressure field on the propeller.

Figure 5.24: Transient incompressible pressure field on the propeller.

Values of torque and thrust for the given propeller in three comparable cases are presented in Table (5.7). Trust for incompressible cases differs 1.25% and torque 1.39%. This small difference shows that steady results at this conditions will not have big deviations compared to transient cases. It can be noticed that compressible effects reduce thrust by 6.59% and increase torque by 27%, although the velocity field and transient effects are very similar in both incompressible and compressible cases. Significant compressible effects appear at the blade tip, which is the main source of suppressive force, yielding a meaningful difference between incompressible and compressible results.

Table 5.7: Comparison of results.

Case	Thrust [N]	Torque [Nm]
Steady compressible MRF	470.55	117.13
Steady incompressible MRF	497.49	84.29
Transient incompressible	503.8[1]	85.48[2]

---

[1]during period of rotation, force is between 503.05 – 504.85 [N]

[2]during period of rotation, moment is between 85.08 – 85.88 [Nm]

5.1.2. Propeller Performance and Convergence Study

In order to make efficiency performance diagram, thrust and moment have to be calculated with advance ratio taken into account. Advance ratio represents freestream velocity flow through the propeller geometry. On the other hand, torque represents a drag which has to be overcome with the purpose of producing such force. As advance radio is increasing, torque is decreasing, and achieves another maximum at $J = 1.158$ in the Figure (5.25). Thrust curve is calculated for angular velocity of 241 rad/s. There is also comparison of static thrust with ground effect where can be seen that force is decreasing for 6.07%, where it drops to value of 845.33 N.
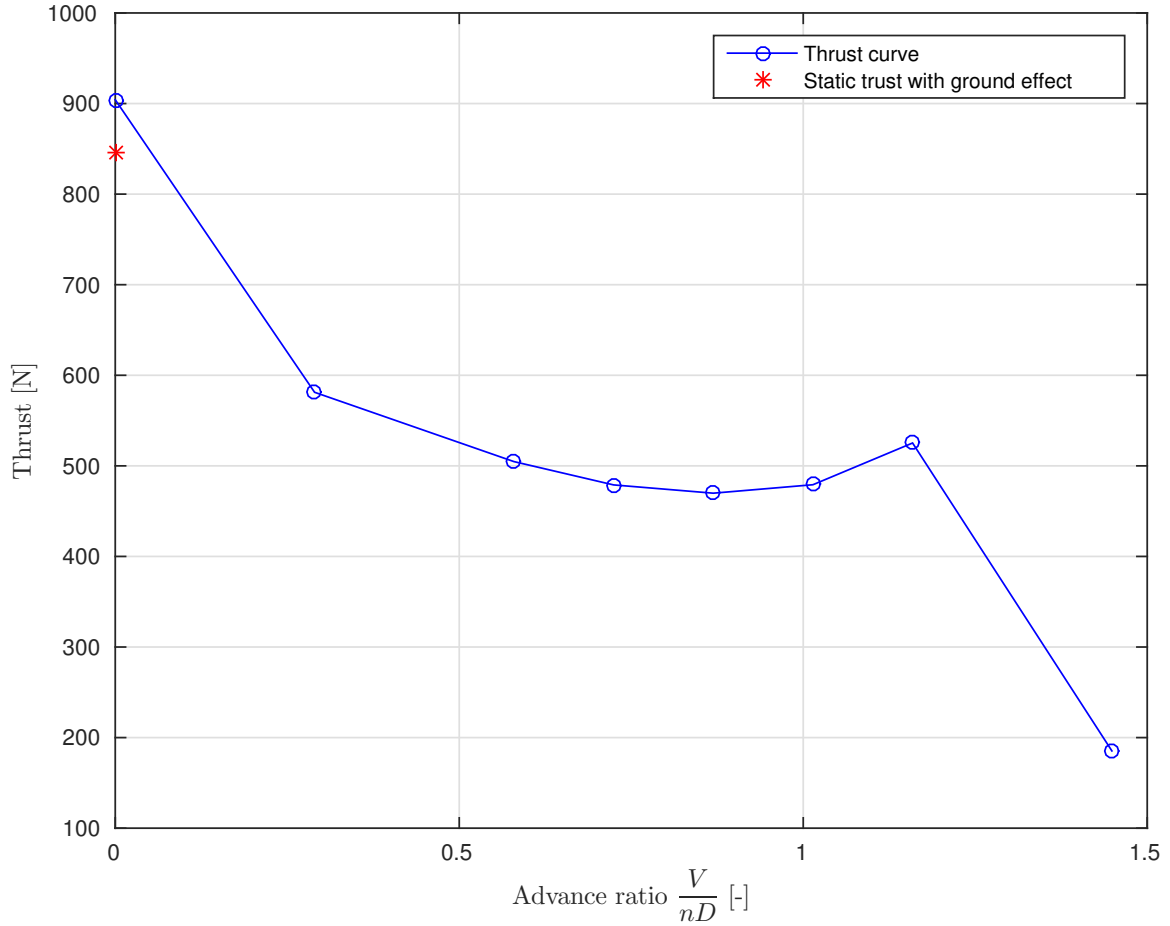

Figure 5.25: Distribution of thrust for advance ratio number.

Torque curve has similar shape to the thrust curve in the Figure (5.25) where torque is reducing with increasing advance ratio and achieves another maximum at $J = 1.158$,

which, in other words, can be described as a freestream velocity of 40 m/s. Static moment with ground effect increased at value of 154.28 N, and changed for 1.15%. A main reason of the increase is drag which has also increased. Since the torque and thrust
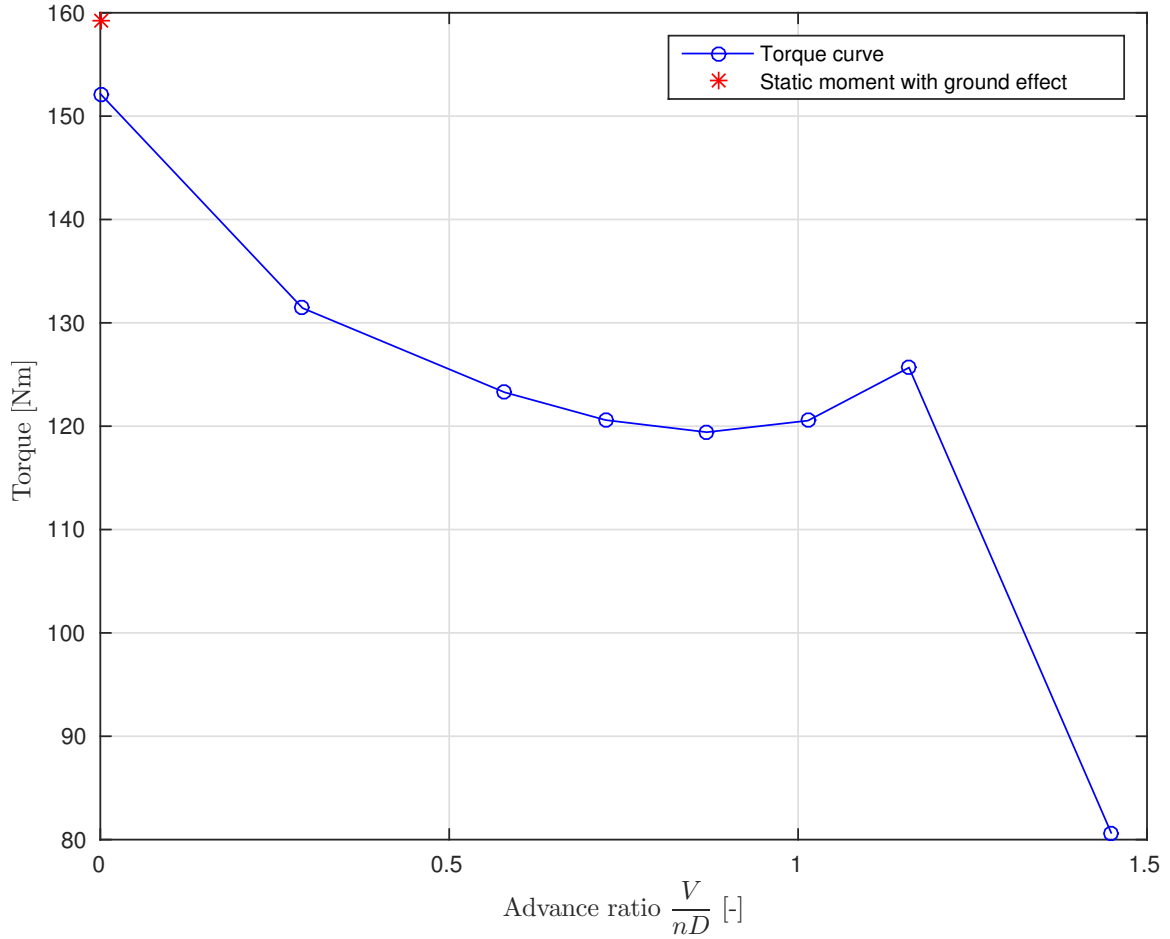

Figure 5.26: Distribution of torque for advance ratio number.

distributions are similar, the point of local maximum at $J = 1.158$ will be the point of maximum efficiency. On the other hand, the maximum moment and thrust is for $J = 0$, but since the efficiency of a propeller is defined as:

$$\eta = \frac{TV}{P} \, ,$$
(5.2)

where for freestream velocity is equal to 0, η will be also 0. Increasing the freestream velocity after the maximum efficiency point propeller will convert from pump to turbine mode, which is not in the field of interest of this thesis.
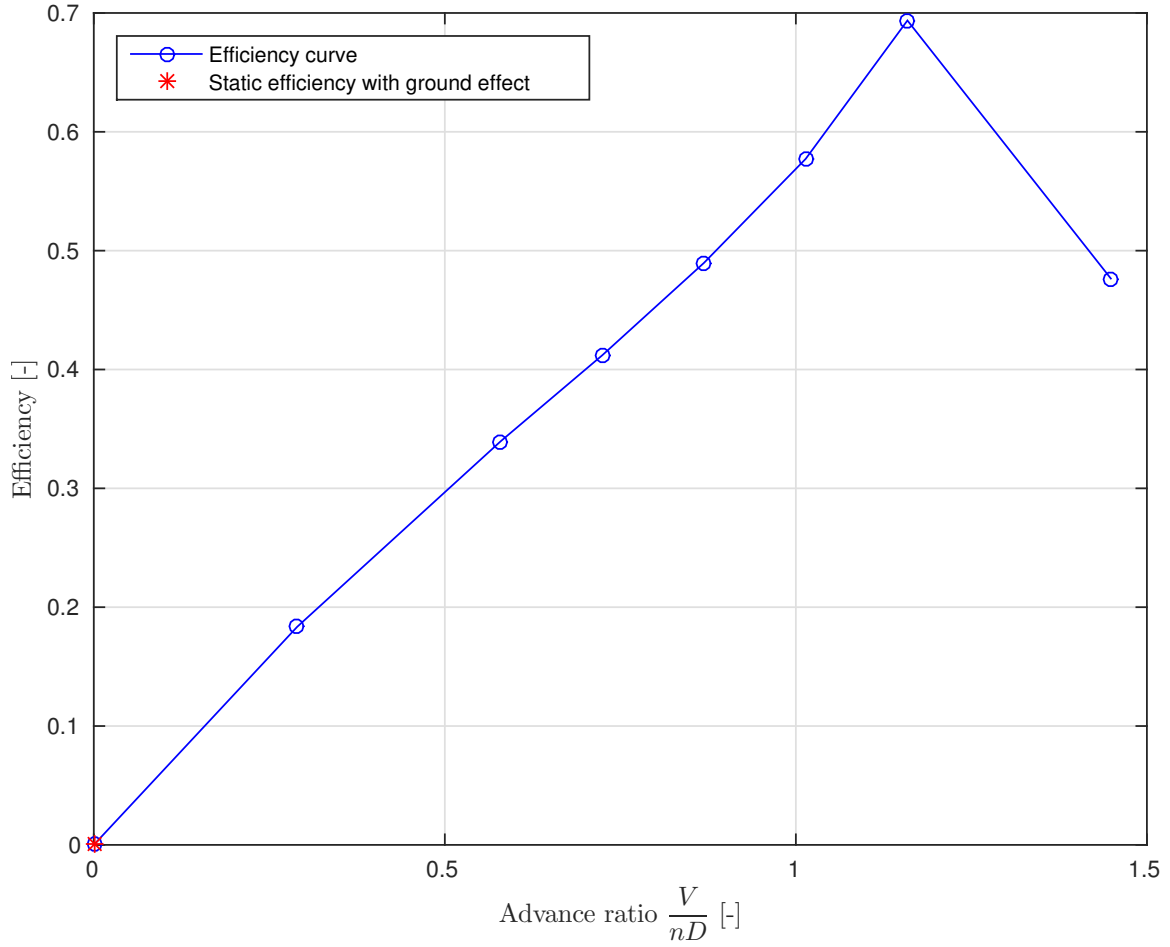
Figure 5.27: Distribution of efficiency for advance ratio number.

A domain for numerical simulation which includes ground effect is presented in the Figure (5.28). When aircraft is taxing clearness between propeller tip and ground is 0.02 m. All other condition are the same as for point $J = 0$. The comparison of velocity field distribution with and without ground effect is shown in the Figure (5.29). At the inlet free stream velocity is close to zero which represents numerical simulation of static thrust and moment. The figure shows visible difference of flow field which effect on pressure distribution on the blade and causes thrust drop and moment increase. Also it effects on velocity field distribution which in case of ground effect has large and abrupt variations.
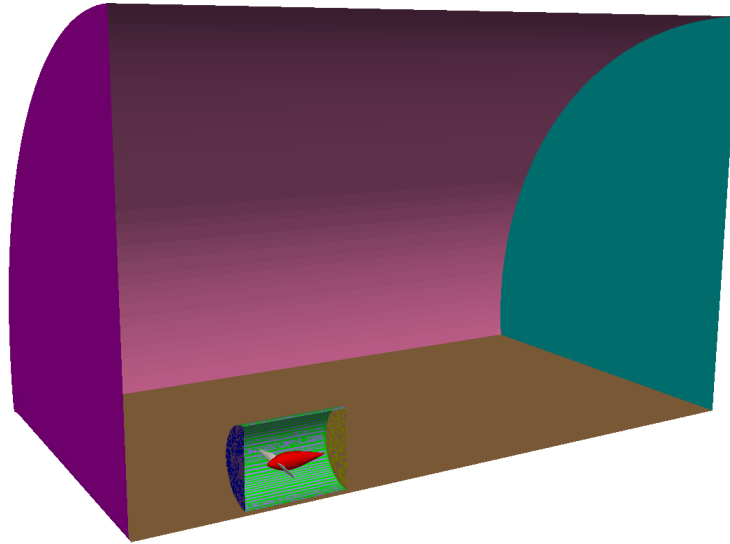
Figure 5.28: Representation of half domain for numerical simulation of static
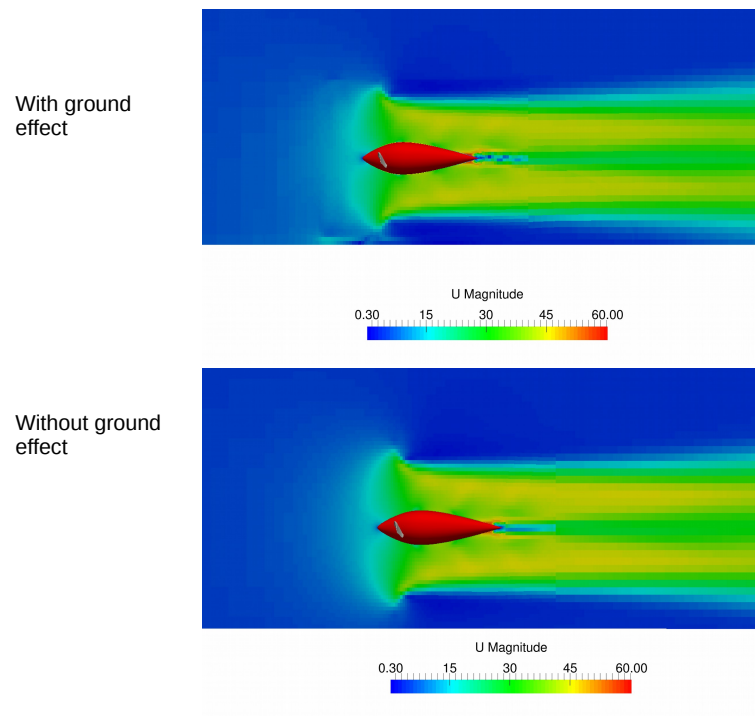thrust and moment.

Figure 5.29: Comparison of velocity field with ground effect.

A convergence study is playing on important role in optimizing and verifying the results. Figures (5.31) and (5.30) are showing convergence of force and torque as the number of cells is increasing. The convergence study has been made for cases with and without cell-limited gradient discretization scheme. This propeller case has shown different convergence behavior for these two schemes. As seen in Figure (5.30) cell limited schemes are more accurate in cases with smaller number of cells. The main reason are large pressure gradients which appearing at the propeller tip, and in order to tackle this problem a fine mesh or limiting pressure gradients inside cells is required. The convergence study for the torque shows different behavior. The results of the cases
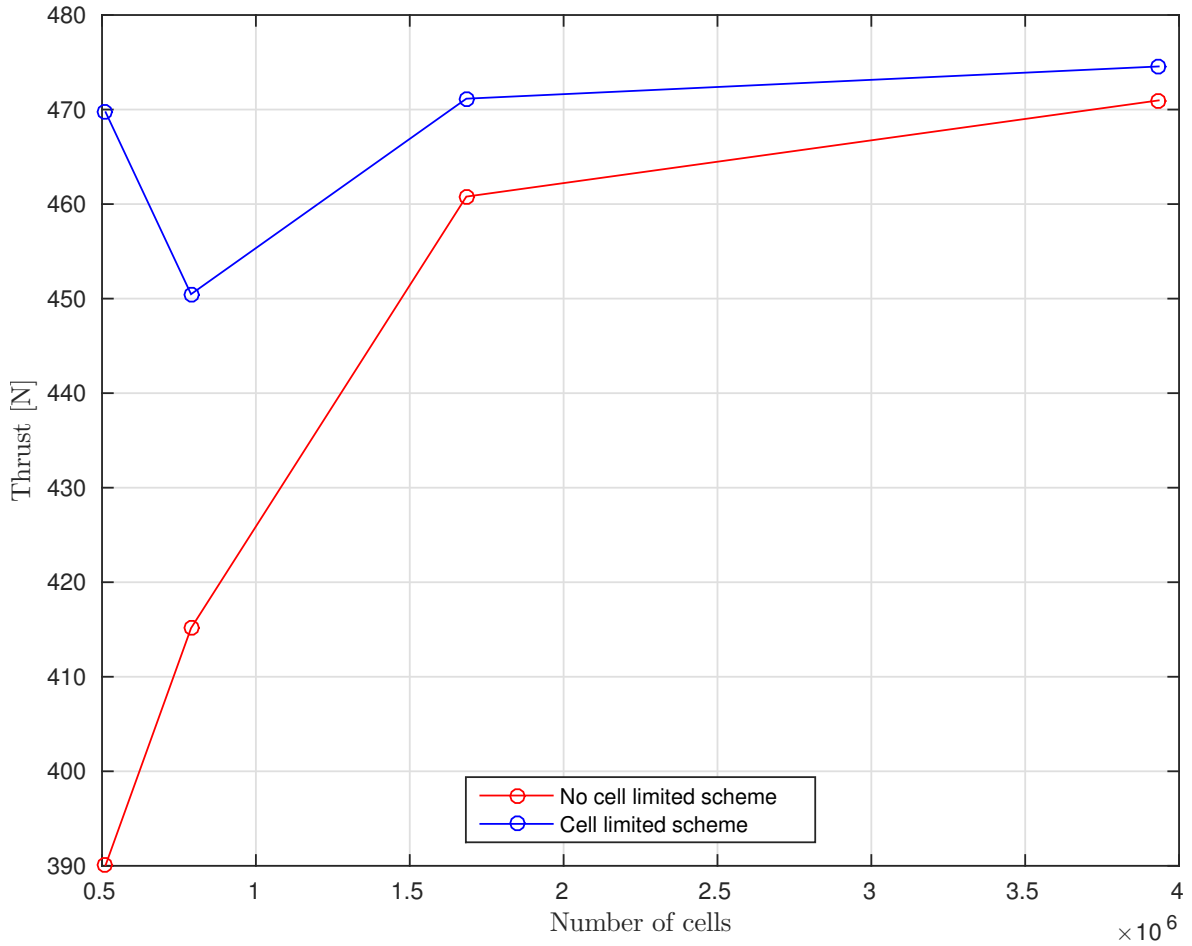
Figure 5.30: Convergence study results for thrust.

without cell limited gradient scheme show smaller torque error for less cells then cases with limited scheme. Final, torque between schemes converged and difference between

moments is 0.83% and thrust is 0.75%. Optimal mesh with adequate number of cells which can capture compressible effects and still have reasonable simulation time is third mesh with 1683816 cells. All the results presented in this study were calculated for the specified mesh with cell limited scheme.

Figure 5.31: Convergence study results for moment.

5.2. Engine Cooling System Simulations

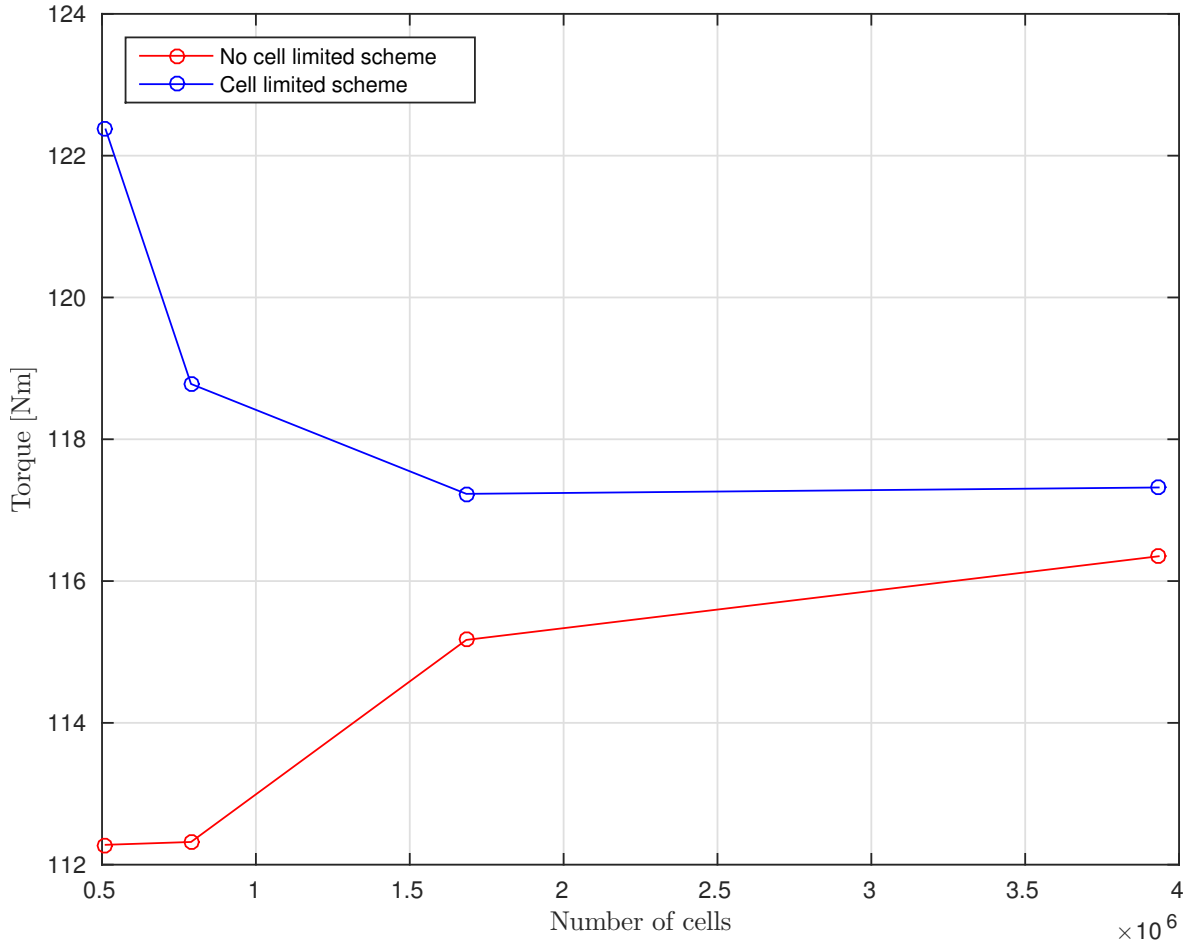In this chapter, a validation of the implemented heat exchanger model is presented. After the validation, results of the engine cooling system, simulation, set-up in Section 4.2. are presented.

5.2.1. Validation of Heat Exchange Models

In order to validate the new heat exchanger model in `foam-extend` a three test cases will analyzed. Domain is made out of a cuboid tube whose heat zone is inside and shown in the Figure (5.32). Inserting specific quantity of heat energy, temperature of fluid has to rise. In addition, specific quantity of energy has been calculated as:

$$\dot{Q}_{tot} = \dot{m}C_p(T_{in} - T_{ref}) \, . \tag{5.3}$$

As the numerical simulation is steady it can be assumed that in every second, for every time step, source of heat energy gives exact quantity of calculated energy to air. Type of the boundary conditions are presented in Table (5.8). As air is flowing through tube with calculated mass flow of $\rho U A$. Specific heat of air is $1005 \, \text{J/kgs}$. In order to test this implementation any value of $Tref$ can be assumed, while the final result of temperature should stay the same. After $\dot{Q}_{tot}$ is calculated, it is the main input of the implemented heat exchanger model, where $\dot{m}$ refers to mass flow calculated inside the heat zone. If assumed value of T_{ref} equals 303 K and the mass flow of the heat zone is $2.44 \, \text{kg/s}$, Q_{tot} can be calculated as:

$$\dot{Q}_{tot} = \dot{m}C_p(T_{in} - T_{ref}) = 24522 \, [W] \, . \tag{5.4}$$

Purpose of this test is to prove that particle which travels through the tube of cuboid shape, with heat zone length of 2 m and with velocity of 2 m/s has to change its temperature for 10 K in one second. Results for the Total Volumetric Heat model, Single Stream model and Nusselt model is presented. Figures (5.34), (5.35) and (5.36) show temperature changes as the particle is approaching the exit of heat zone. Comparing the total volumetric heat model (5.34) with the single stream approach in Figure (5.35) temperature fields differ. The main reason for the difference is in definitions of the models. As Single Stream approach includes local velocity and temperature, it exhibits reduced values of temperature field distribution in comparison to the Total Volumetric
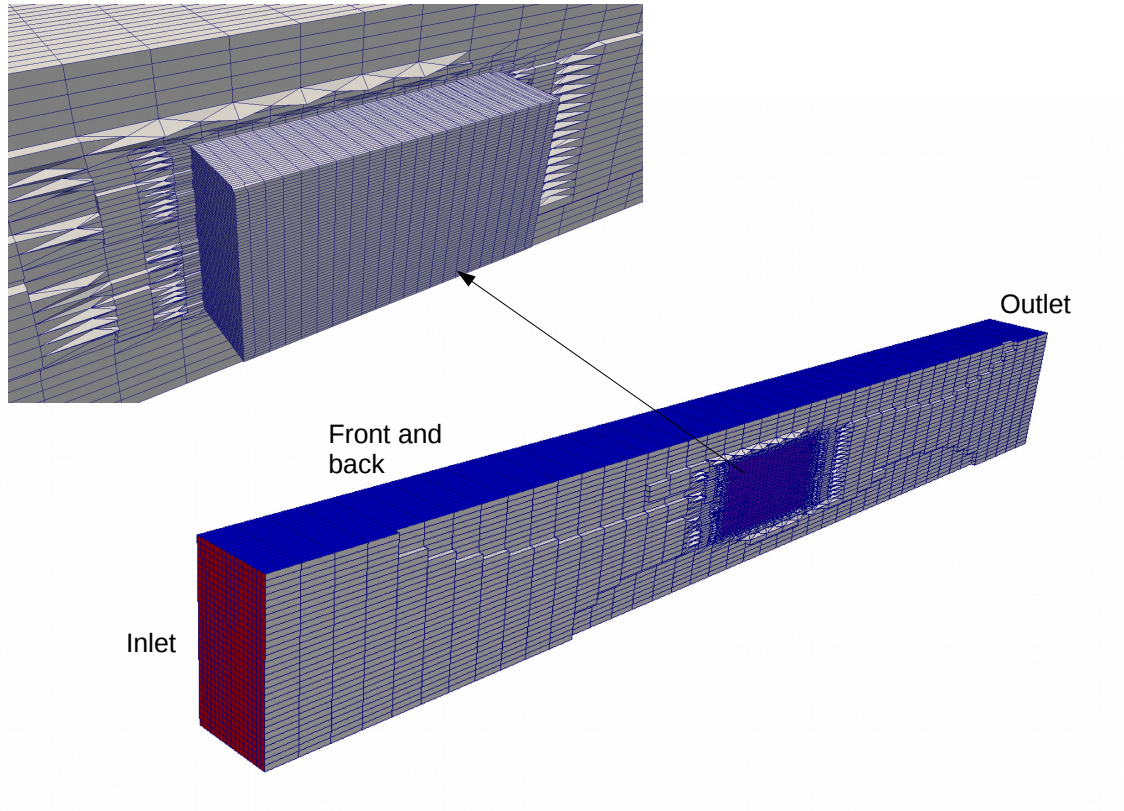
Figure 5.32: Domain and heat zone.

Table 5.8: Type of boundary conditions of test cases.

	Frontandback	**Inlet**	**Outlet**
Velocity	fixedValue	flowRateInletVelocity	inletOutlet
Pressure	zeroGradient	zeroGradient	fixedValue
ν_t	nutWallFunction	calculated	calculated
μ_t	mutWallFunction	calculated	calculated
α_t	alphatWallFunction	calculated	calculated
k	compressible::kqRWallFunction	fixedValue	inletOutlet
ω	compressible::kqRWallFunction	fixedValue	inletOutlet
Temperature	zeroGradient	fixedValue	zeroGradient

Heat model and Nusselt model. The Nusselt model calculates total heat transfer using equation (3.42) and effectiveness via (3.41). In oder to make a comparable test case, the effectiveness needs to remain around ≈ 1. High value of the Nusselt number has to be assumed. As the Nusselt model is very similar to the Total Volumetric Heat model, only difference being the numerical discretization while calculating the total heat transfer. The assumption of the effectiveness was good because the Nusselt model has similar temperature field as the TVH model. The results can be seen in figures (5.36)and (5.34).

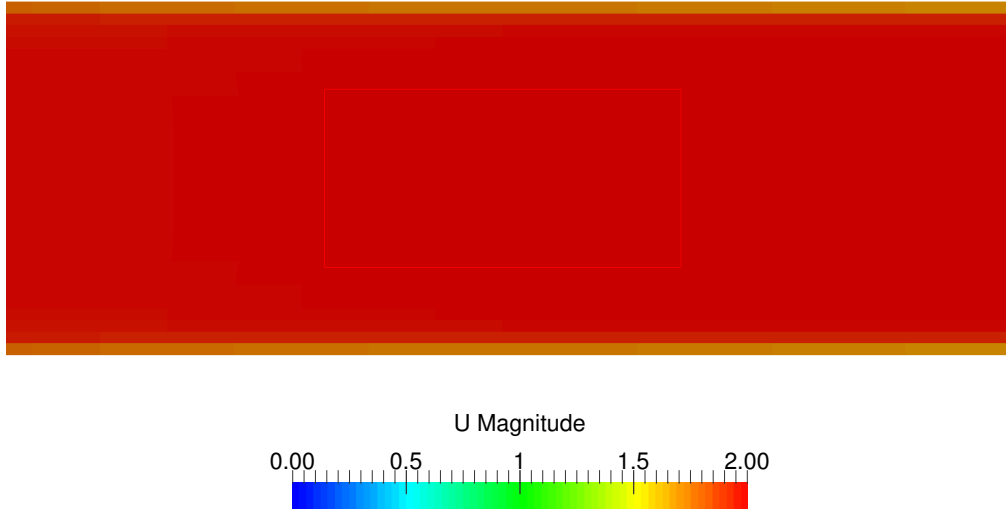For all the cases velocity is calculated by the specified flow rate, which gives better

Figure 5.33: Velocity distribution through box.

convergence than using field velocity value at the inlet. As code is calculating mass flow it is optimized to make velocity $\approx 2\,\mathrm{m/s}$, which is important in order to keep the idea of particle passing trough the heat zone in one iteration. Velocity distribution is presented on the Figure (5.33), where the surface of rectangle represents the heat zone.
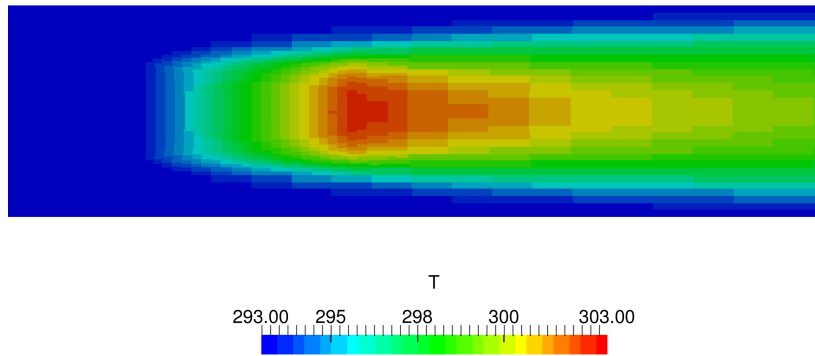
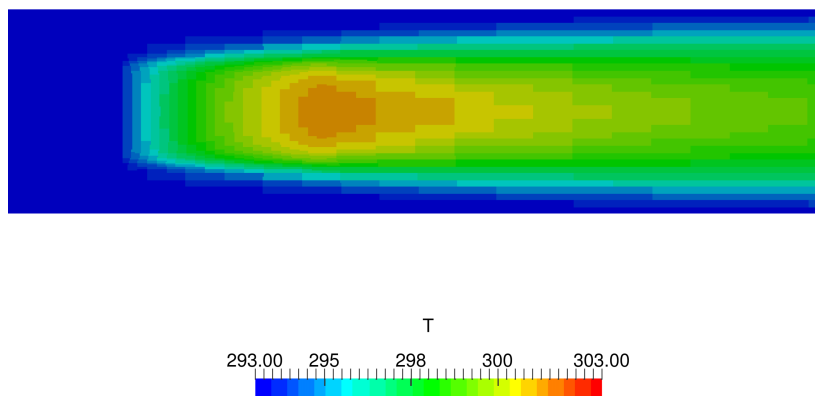Figure 5.34: Total Volumetric Heat model test result.
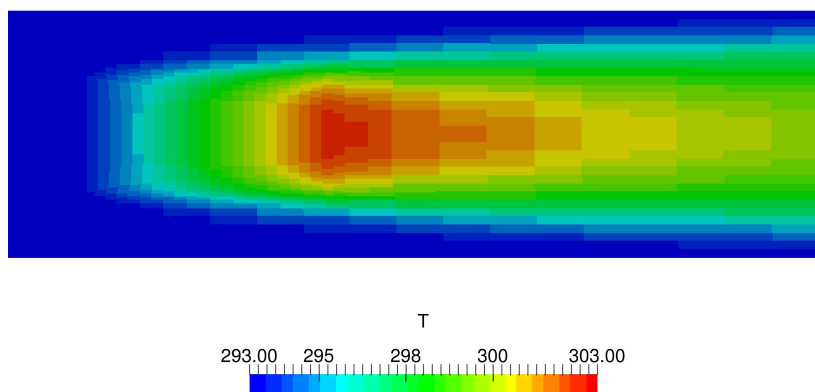

Figure 5.35: Single Stream model test result.

Figure 5.36: Nusselt model test result.

5.2.2.   Integration of Propeller and Cooling System Case

Case set-up was presented in Section (4.2.). The boundary conditions for inlet and outlet are specified in Table (5.9). Free stream velocity is 100 m/s, and attack angle of the aircraft is $-1.5°$ for the cruising operating point, also the absolute velocity at inlet will be divided into components, on the other hand, zero gradient is at outlet. For compressible solver total pressure and temperature boundary conditions are used. ν_t, α_t and μ_t are calculated at inlet and outlet patches.

Table 5.9: Inlet and outlet boundary conditions for cooling system.

Patch	Inlet	Outlet
Velocity	type pressureInletVelocity; value uniform $(97.667\ 0\ -2.557)$;	type zeroGradient;
Pressure	type isentropicTotolPressure; U U; p0 uniform 84315.7;	type fixedValue; value unifrom 79495;
ν_t	type calculated;	type calculated;
μ_t	type calculated;	type calculated;
α_t	type calculated;	type calculated;
k	type turbulentIntensityKineticEnergyInlet; value uniform 0.0143;	type zeroGradient;
ω	type fixedValue; value uniform 751;	type zeroGradient;
Temperature	type isentropicTotatTemperature; phi phi; psi psi; p p; p0 uniform 287.94;	type zeroGradient;

Turbulence coefficients are obtained using the equation (4.1) where turbulence intensity is 5%. Turbulent length scale ω requires characteristic length for its calculation. The characteristic length is the height of fuselage in z-direction. All other boundary types are wall type, and are shown in the Table (5.10). Velocity boundary condition

is set to fixed value zero. Pressure and temperature boundary conditions are set zero gradient. Wall functions are set for ν_t, μ_t and α_t.

Table 5.10: Wall type boundary conditions for cooling system.

Patch	WallGroup	Porositywall
Velocity	type fixedValue; value uniform (0 0 0);	type slip; value uniform (0 0 0);
Pressure	type zeroGradient;	type zeroGradient;
ν_t	type nutWallFunction;	type nutWallFunction;
μ_t	type mutWallFunction;	type mutWallFunction;
α_t	type alphatWallFunction;	type alphatWallFunction;
k	compressible::kqRWallFunction; value uniform 0.0143;	compressible::kqRWallFunction; value uniform 0.0143;
ω	compressible::omegaWallFunction; uniform 751;	compressible::omegaWallFunction; uniform 751;
Temperature	type zeroGradient	type zeroGradient;

Results are be presented for velocity, pressure and temperature fields inside the engine compartment. Large pressure drop is located at the intake of diffuser. After passing the diffuser air flows into engine compartment. In Figure (5.37) velocity drop can be seen due to turning of the flow field by existence of engine wall and porous media. Definition of porous media for velocity in linear momentum equation is defined as a sink, which is why velocity drop is created along the surrounding area of porosity. Pressure and velocity distribution over the same slice, for all three models, are expected to be similar because equations for pressure and velocity do not differ.

In order to set the actuator disk in front of diffuser, mesh needs to be upgraded with a patch which defines the propeller plane. Boundary conditions are defined and presented in Table (5.11). Type of the patch is cyclic. There are few important pressure boundary conditions which are user defined: pressure function which depends on velocity, it is defined as constant value 2672.23 Pa; load profile, defined as constant through radius. Velocity boundary condition demands profile angle, angular velocity, start and end of ramp time. Figure (5.38) presents velocity and pressure distribution on sliced plane along aircraft. In comparison with (5.37) pressure abrupt can be seen as cause of

actuator disk theory. Velocity is increased for 28 m/s, and pressure for 3370 Pa.

Table 5.11: Actuator disk type boundary conditions for cooling system.

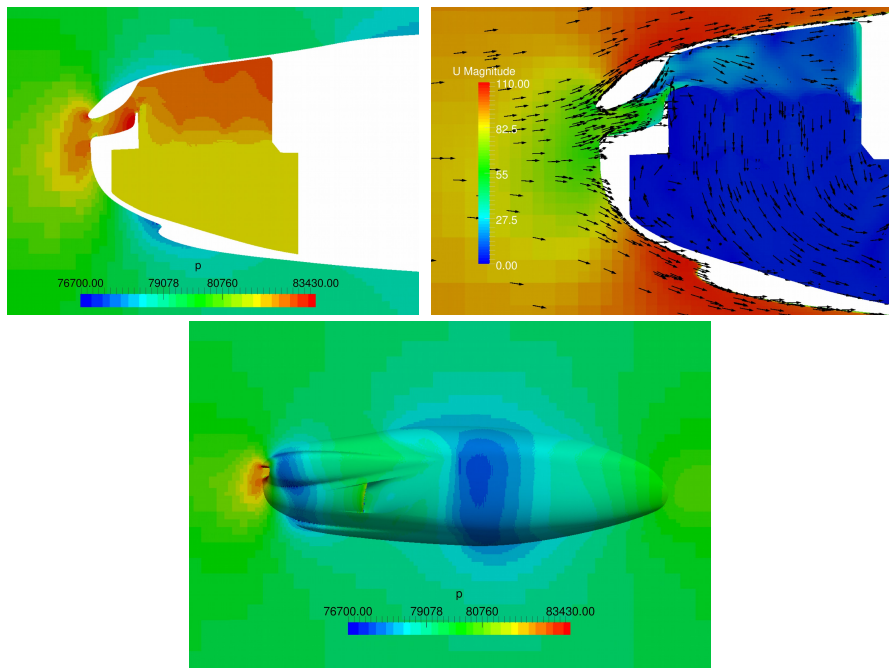| Patch	propellerDisk
Pressure	type propellerPressure; patchType cyclic; f 1(2672.23); loadProfile 2 (0 1 1 1);
Velocity	type propellerVelocity; patchType cyclic; rpm 2301; rampStart 0; rampEnd 10; alphaProfile 2(0 30 1 5.8);
ν_t	type cyclic;
μ_t	type cyclic;
α_t	type cyclic;
k	type cyclic;
ε	type cyclic;
Temperature	type cyclic;

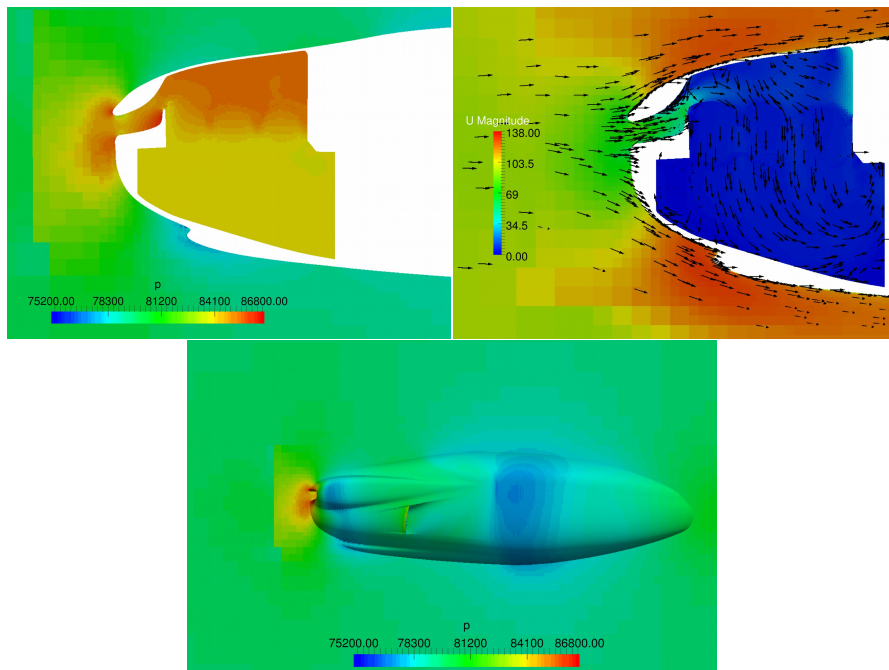Figure 5.37: Pressure and velocity field distribution.

Figure 5.38: Pressure and velocity field distribution with actuator disk.

First, temperature distribution without propeller disk actuator will be explain. Figure (5.39) presents two representative sliced planes along aircraft fuselage, and engine compartment. As the heat transfer is modeled in three different ways, comparison is shown between Figures (5.40), (5.41) and (5.42). The largest heat transfer is made for SS model. It confirms test case results where in comparison of all three models lowest temperature distribution was for SS model in Figure (5.35). Including velocity and temperature field in heat transfer equation, heat will have moving and diffusive ability and it will end up with smaller temperature values. Higher temperature value characterize TVH model it appear in areas behind sharp edges because weak influence of velocity at model and temperature difference between cells. It only includes the cells volumes where the amount of source heat is distributed depending only on the cells volumes. If the volume is larger it will give more heat to air and vice versa. Third model, Nusselt model, has highest temperature values between other two, and basically defines temperature distribution as product of the calculated heat source rate and effectiveness of heat exchanger (air cooling ribs) as function of Nusselt number. This model is a bit different than the previous two. The Nusselt model needs from the user to define average Nusselt number and the hot stream temperature, or the constant temperature which is in cooling system case the cylinder temperature. As the heat source rate is calculated for porous zone cells, it has ability of adjustments to geometry and domain. Temperature distribution is similar to TVH model, but temperature value is higher for Nusselt model. Temperature rises in areas behind sharp edges where velocity is reduced and causes reduced thermal convection coefficient. It results reduced heat transfer. All three models produce visible temperature increase in a shape of cylinder section. In Figure (5.43) porous wall areas has highest temperature values as passing through porous zone temperature is rising. It shows swirling inside internal passage behind engine. This swirling reduces efficiency of cooling system, and make hot air keeps inside increasing total temperature field distribution.
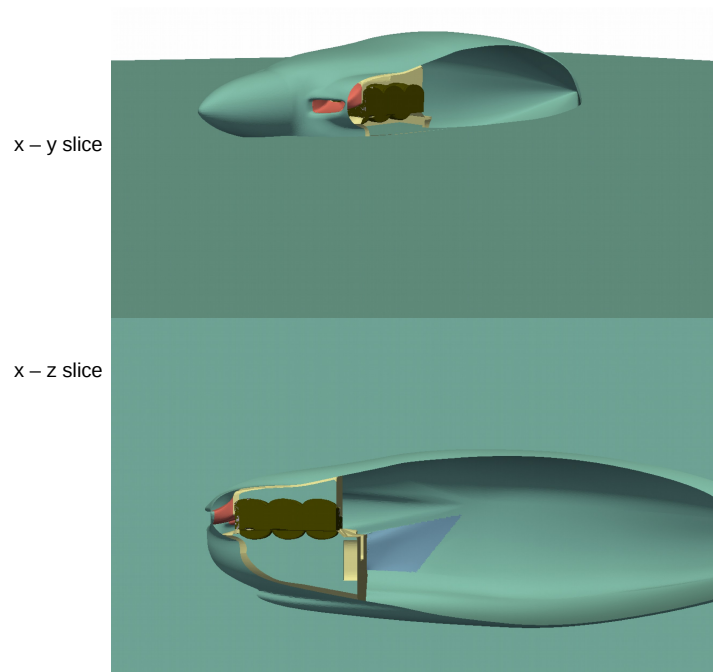
x – y slice

x – z slice
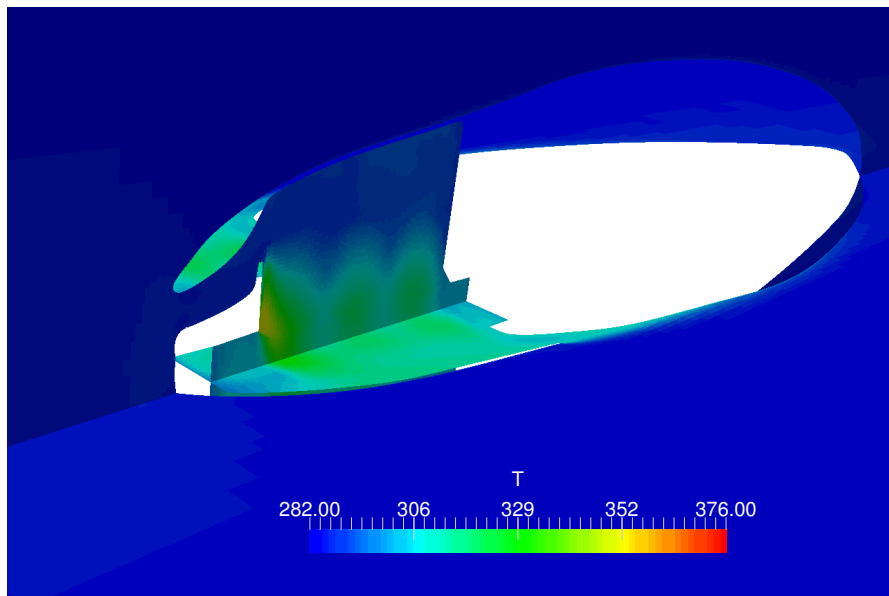
Figure 5.39: Cutting planes for results view.

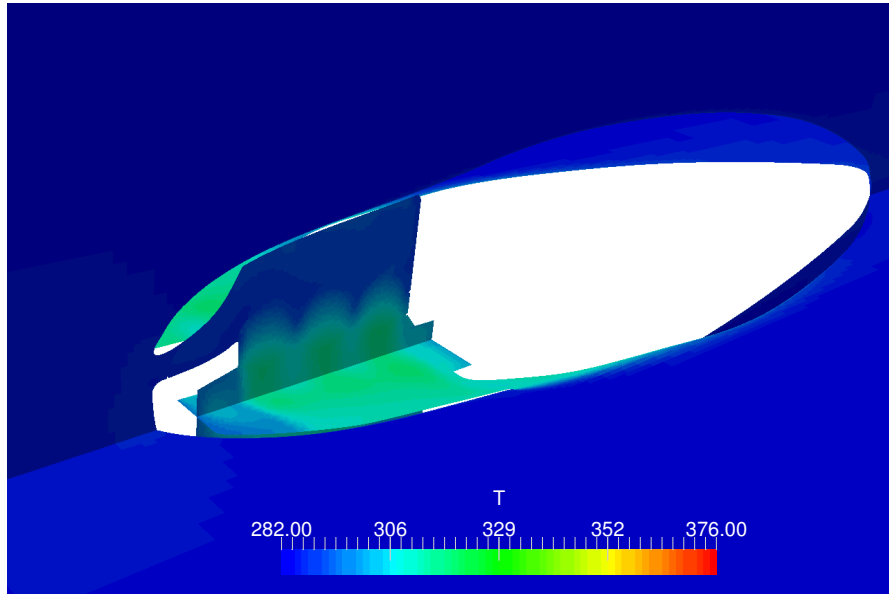Figure 5.40: Total Volumetric Heat (TVH) model temperature results.

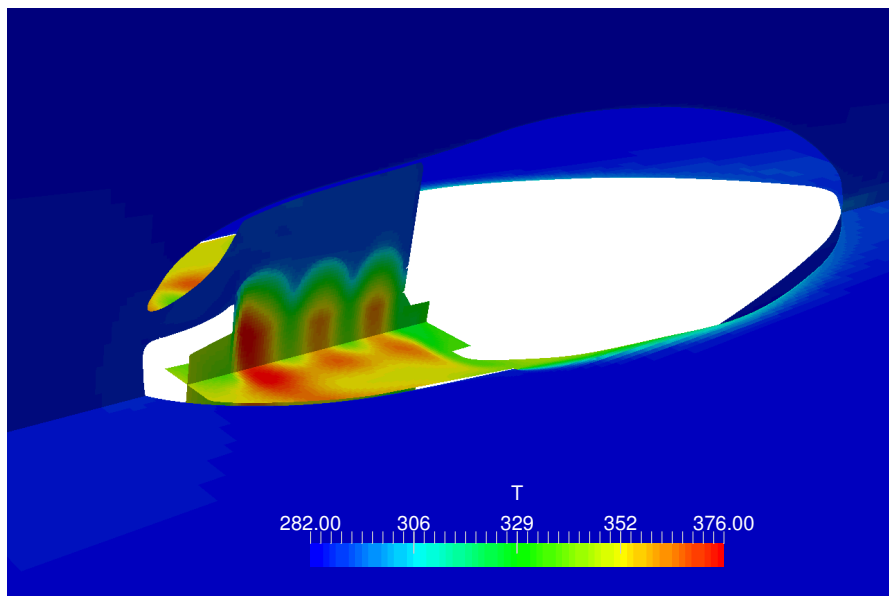Figure 5.41: Single Stream (SS) model temperature results.

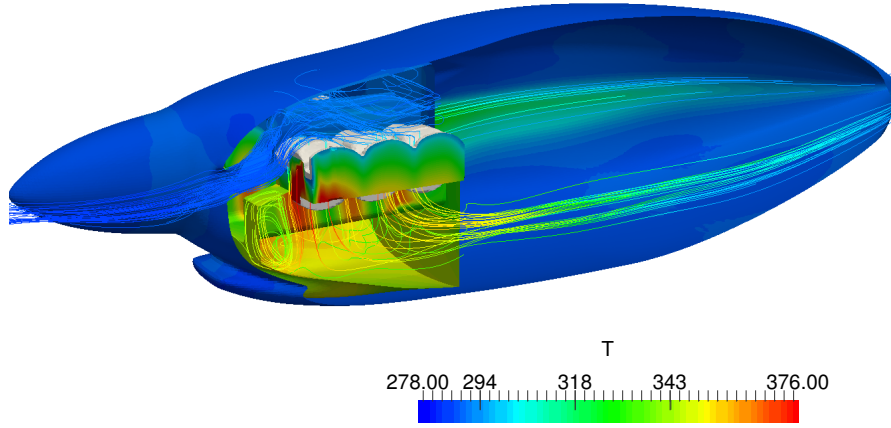Figure 5.42: Nusselt model temperature results.

Figure 5.43: Velocity stream lines with temperature distribution.

5.2.3.   Field Temperature Results with Actuator Disk

In this subsection the temperature field of the cooling system with actuator disk are presented in Figures (5.44), (5.45) and (5.46). The results are obtained using set up form Section (4.2.) with addition of boundary condition upgraded and explained in the section (5.2.2.). Representative slices are shown in figure (5.39). Total temperature of domain is reduced in comparative with cases without actuator disk. Also the total temperature is reduced at the internal engine compartment. The main cause is increase of the mass flow as the actuator disk is set at the spinner in front of the diffuser. Pressure and velocity increases as presented in Figure (5.38). In repercussions the heat transfer increased. Temperature distributions are similar to Figures (5.40), (5.41) and (5.42), respectively. Also, flow field visualization of the Nusselt model is presented. The purpose of it is to see if there are any swirls at the internal passage that disrupt cooling of the engine. Temperature distribution of the air with their velocity stream lines is presented in Figure (5.47). In the comparative with Figure (5.39) velocity stream lines are not changed, only temperature field values are decreased. Difference is also in temperature distribution on the spinner which shows influence of the actuator disk. Another reason in decrease of temperature distribution is lower inlet total temperature caused by the
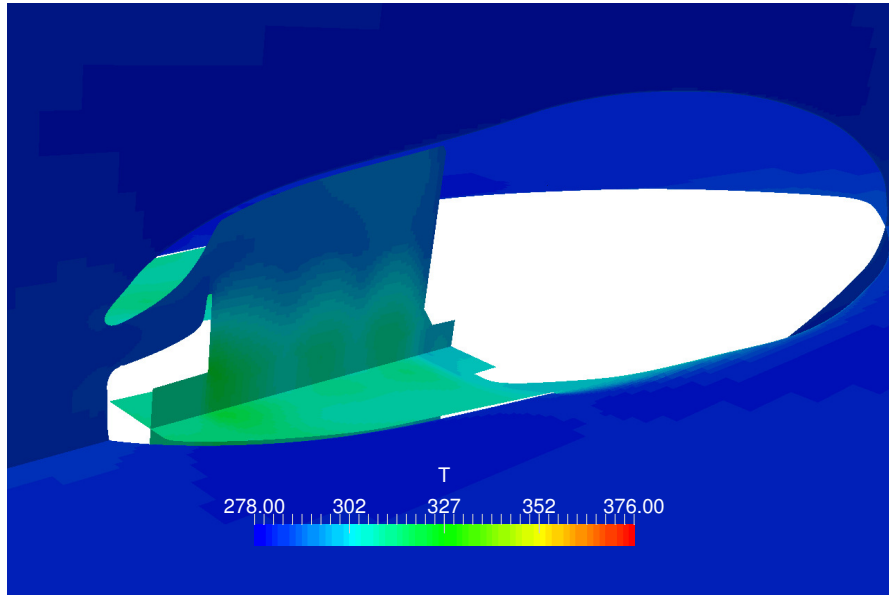
influence of the actuator disk.

Figure 5.44: Total Volumetric Heat model temperature results.
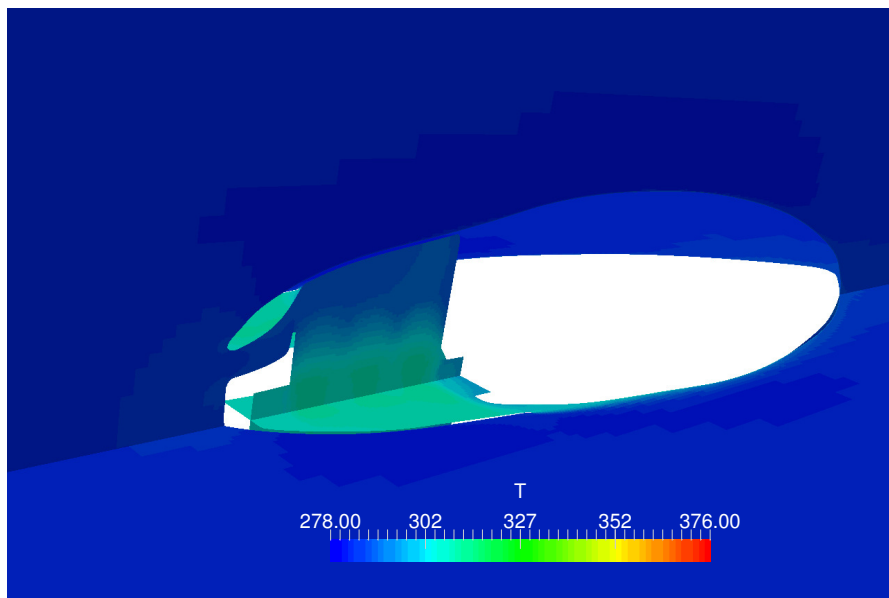

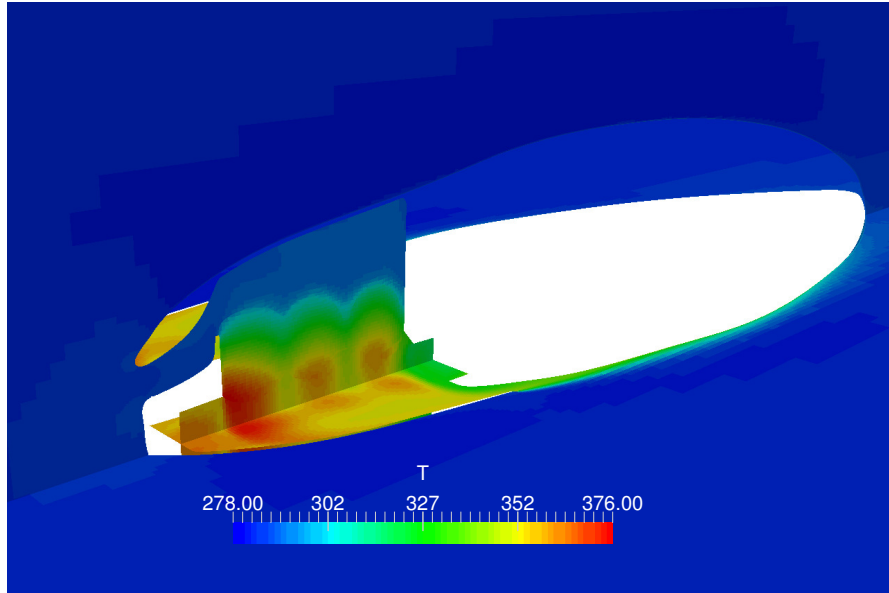Figure 5.45: Single Stream model temperature results.

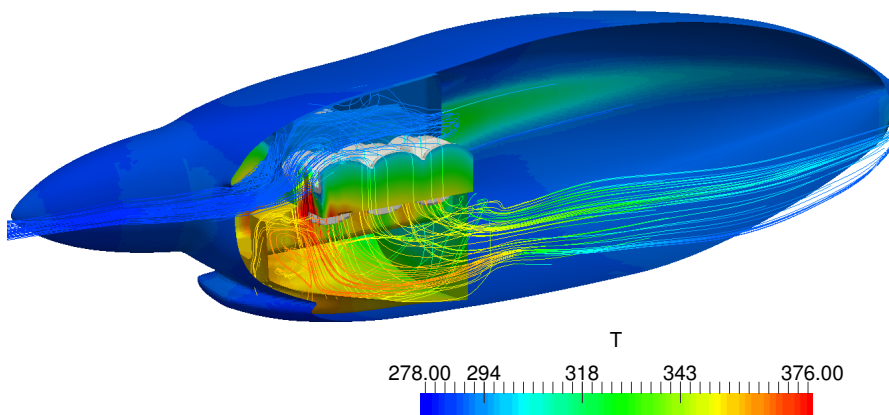Figure 5.46: Nusselt model temperature results.

Figure 5.47: Velocity stream lines with temperature distribution of Nusselt model.

6 | Conclusion

In this thesis numerical models are used to reduce time and cost of engineering development. CFD simulations are significantly less expensive compared to complicated and time consuming physical experiments. The most critical part of the aircraft propeller case is the rotor-stator interference and the stability of numerical simulation using *cyclicGgi* patches which reduces simulation time by giving the ability to simulate only half of domain. This applications demand perfect connections of faces between rotational and stationary mesh, which is hard to achieve with *snappyHexMesh* automatic meshing tool. It is suggested to use another more advanced meshing tool. The another reason for that is the large velocity difference over the propeller radius which strongly effects $y+$ distribution. To achieve better distribution of $y+$, the first layer of cells need to have specific height depending on the location radius. Compressible and incompressible simulations show significant difference in pressure distributions which result in different values of total forces and moments. The necessity for using compressible solver for these types of problems is presented here. On the other hand, small differences are seen between steady and transient simulations which proves the use of steady-state solver as acceptable. The propeller performance is presented for eight operating points, and it shows two maxima, where the first one is for $J = 0$ which was expected, and other one is at $J = 1.158$. Between these points propeller is designed to reduce power consumption and for wider range of advance radio J. Further optimization of propeller could be done in order to reduce material stresses and drag force in cruise operating points. In that way power consumption would be reduced and aircraft would have lower operating costs. The existing steady-state compressible solver is upgraded with porous

media effects and three heat transfer models. The total volumetric heat model and the Nusselt model show similar behavior, and produce similar results, while single stream model is modeled for a singe stream heat exchanger which strongly depends on mass flow and results in lower temperatures for the same amount of heat transfer. Results of the temperature fields clearly show areas with high temperature, and whether the engine is being cooled optimally. This information also helps in improving cooling efficiency and reducing power consumption for the whole range of operating points. Reducing the influence of the propeller wake on internal flow can improve cooling and also minimize wall temperatures and conjugate heat transfer conditions and maximize usage of the limited space inside the engine compartment.

Bibliography

[1] M. Ferziger J. H., Perić. *Computational Methods for Fluid Dynamics*. Springer, Berlin, 1996.

[2] D.C. Wilcox. *Turbulence Modeling for CFD*. DCW Industries, Inc, 1993.

[3] H. Jasak. *Lecture slides: Turbulence Modeling for CFD*, 2011.

[4] http://www.cfd-online.com/Wiki/SST_k-omega model.

[5] M. Beaudoin and H. Jasak. Development of a generalized grid interface for turbomachinery simulations with openfoam. In *Open Source CFD International Conference*, number December 2008, 2008.

[6] Vishal a Jambhekar. Forchheimer porous-media flow models - numerical investigation and comparison with experimental data. Master's thesis, Universität Stuttgart - Institut für Wasser- und Umweltsystemmodellierung, 2011.

[7] https://www.sharcnet.ca/Software/Fluent6/html/ug/node297.htm.

[8] Doucet M. & Jahra F. Islam M. Optimization of rans solver simulation setup for propeller open water performance prediction. *Proceedings of the ASME 2015 34th International Conference on Ocean, Offshore and Arctic Engineering*, May 31-June 5, 2015,.

[9] G. Cvijetić. *Steady State Methods for Turbomachhinery*, 2014.

[10] Benjamin Pinkel. HEAT-TRANSFER PROCESSES IN AIR-COOLED ENGINE CYLINDERS. *Report N0. 612*, page 24, 2017.

[11] Lawrence V. Underhood airflow simulation of a passenger car using computational fluid dynamics. *The 10th International Mobility Technology Congress and Exhibition*, 2001.

[12] Nobel T.P. and Jain S.K. Improving truck underhood thermal management through cfd. *SAE 2002 World Congress and Exhibition*, 2002.

[13] Ninoyu M. Ohshima T., Hamatani K. and Nakagawa K. Influence of the cooling air flow outlet on the aerodynamic characteristics. *JSAE Review*, 1998.

[14] H. Jasak I. Dominics, M.Willetts. *Enhanced Turbomachinery Capabilities for foam-extend: Development and Validation.*

[15] S. Kurepa. *Matematička analiza 1 (diferenciranje i integriranje)*. Tehnička knjiga, Zagreb, 1989.

[16] C. Hirsch. Computtional methods for inviscid and viscous flows. *Numerical Computation of Internal and External Flows, Volume 2*, 1990.

[17] H. Jasak. *Error Analysis and Estimation for the Finite Volume Method with Application to Fluid Flows*. Imperial College of Science, Tehnology & Academic Emergency Medicine, London,, 1996.

[18] C.Hall S. Dixon. Introduction: Basic principles. *Fluid Mechanics and Thermodynamics of Turbomachinery*, 2010.

[19] Emil Ljungskog and Ulf Nilsson. Cfd for underhood modeling development of an efficient method. *Journal of Mechanical Science and Technology*, 2014.

[20] H. Jasak G. Cvijetic. The compressible harmonic balance method for turbomachinery. *2018 AIAA Aerospace Science Meeting*, 2018.